The electromechanical excitation mechanism of film capacitors within highly integrated drivetrains

Dissertation

Technische Universität Darmstadt

submitted in fulfilment of the requirements for the degree of
Doctor of Engineering

by
Maximilian Michael Herrnberger
Darmstadt 2023

Referees:
Prof. Dr. mont. Mario Kupnik
Prof. Dr.-Ing. Thilo Bein

Department: Elektrotechnik und Informationstechnik (ETIT)
Research area: Mess- und Sensortechnik (MUST)

Submission date: 23 June 2023
Disputation date: 18 December 2023

The electromechanical excitation mechanism of film capacitors within highly integrated drivetrains

Genehmigte Dissertation von
Maximilian Herrnberger

Tag der Einreichung: 23.06.2023
Tag der Prüfung: 18.12.2023

Darmstadt, Technische Universität Darmstadt

Bitte zitieren Sie dieses Dokument als:
URN: urn:nbn:de:tuda-tuprints-285812
URL: http://tuprints.ulb.tu-darmstadt.de/28581
Jahr der Veröffentlichung auf TUprints: 2024

Erklärungen laut Promotionsordnung

§8 Abs. 1 lit. c PromO

Ich versichere hiermit, dass die elektronische Version meiner Dissertation mit der schriftlichen Version übereinstimmt.

§8 Abs. 1 lit. d PromO

Ich versichere hiermit, dass zu einem vorherigen Zeitpunkt noch keine Promotion versucht wurde. In diesem Fall sind nähere Angaben über Zeitpunkt, Hochschule, Dissertationsthema und Ergebnis dieses Versuchs mitzuteilen.

§9 Abs. 1 PromO

Ich versichere hiermit, dass die vorliegende Dissertation selbstständig und nur unter Verwendung der angegebenen Quellen verfasst wurde.

§9 Abs. 2 PromO

Die Arbeit hat bisher noch nicht zu Prüfungszwecken gedient.

....	....
Ort, Datum	Unterschrift

Abstract

DC-link capacitors are used in highly integrated power electronics for electric drives. These capacitors compensate for harmonics caused by switching operations during the conversion. The harmonics depend on the switching strategy of the transistors within the converter and cause the DC-link capacitor within the power electronics to vibrate mechanically. This can cause high-frequency acoustic noise, which propagates via structure-borne and airborne sound paths and thus can be a source of interference within electric vehicles.

In the acoustic investigation of electric drives, the existing literature is focused mainly on noises that arise due to varying Maxwell forces in the air gap field between the rotor and stator. However, for a comprehensive acoustic evaluation, the excitations from the power electronics must also be considered. This is particularly important for highly integrated drives in which the power electronics, the electric machine and the gearbox are integrated into a compact drive unit. Within the power electronics, the focus is on the DC-link capacitor since it is subjected to voltage ripples. In electric drives, polypropylene-based film capacitors are widely used, which usually consist of several capacitor windings embedded in epoxy resin.

In this work, a model is presented for predicting the voltage-induced acoustic excitation of film capacitors. For this purpose, a sensor model known from the literature is first transferred to a plate capacitor to analytically derive the deformation in a single capacitor layer. In addition to the electrostatic attractive forces of the electrodes, this model also considers electromechanical couplings in the dielectric, which are described by the electrostrictive parameters. The analytically calculated deformation amplitudes can then be transferred to the geometry of a capacitor winding using finite element (FE) simulations. The application of FE models makes it possible to take into account the structural-dynamic properties of different capacitor geometries.

Since film capacitor windings consist of several thousand layers, the FE models are simplified in a way that modal superposition can be applied as a model reduction method. The aim is to increase the numerical efficiency of the simulation and thus to simulate larger capacitor structures with reduced resource consumption. The resulting excitation model is then validated by measurements at both the winding and the capacitor level and can be used to predict the excitation of polypropylene-based capacitors. In addition, the resulting airborne sound radiation from capacitors is estimated based on the resulting surface velocity.

Acoustic measurements on capacitor windings also show that the excitation amplitude depends on the polarity of the applied DC voltage. Accordingly, polarization effects in the dielectric must also be considered (especially for small voltages), which can be caused by the manufacturing process of the metallized capacitor films. Polarization is caused by both space charges in the dielectric and a boundary layer near the metallization and leads to an intrinsic electrical field that influences the acoustic excitation of the windings. This boundary layer is detected in the course of the work using high-resolution transmission electron microscopy.

Furthermore, the acoustic influence of the polarization present in the capacitor winding can be used to determine a corresponding compensation voltage that is needed to cancel the internal polarization. The compensation voltage can be influenced externally either by voltage pulses or temperature loads, which will be investigated in further experiments. The stability of the compensation voltage over time is also analyzed, and various relaxation mechanisms are discussed. The behavior of the capacitor windings can be compared to the long-term stability of electrets. The present investigations are based on polypropylene capacitors but can essentially be transferred to other dielectrics by adjusting the characteristic values.

The findings presented in this work enable a prediction of the excitation amplitudes of film capacitors. The model presented combines various excitation mechanisms and takes into account the polarization caused by the manufacturing process. The results provide a basis for considering DC-link capacitors in the electric drivetrain as a source of acoustic excitation.

Kurzfassung

In hochintegrierten Leistungselektroniken für elektrische Antriebe kommen Zwischenkreiskondensatoren zum Einsatz. Diese kompensieren Oberschwingungen, die durch Schaltvorgänge bei der Umrichtung hervorgerufen werden. Diese Oberschwingungen hängen von der Schaltstrategie der Transistoren im Umrichter ab und regen den Zwischenkreiskondensator innerhalb der Leistungselektronik zu mechanischen Vibrationen an. Dadurch können hochfrequente akustische Störgeräusche verursacht werden, die sich über Körperschall- und Luftschallpfade ausbreiten und in Elektrofahrzeugen eine Störquelle innerhalb des elektrischen Antriebs darstellen.

Die bestehende Literatur konzentriert sich bei der akustischen Untersuchung von elektrischen Antrieben hauptsächlich auf Geräusche, die durch variierende Maxwell-Kräfte im Luftspaltfeld zwischen Rotor und Stator entstehen. Für eine umfassende akustische Betrachtung müssen jedoch auch Anregungen aus der Leistungselektronik berücksichtigt werden. Dies ist insbesondere bei hochintegrierten Antrieben wichtig, bei denen die Leistungselektronik, die elektrische Maschine und das Getriebe in einer kompakten Antriebseinheit integriert sind. Innerhalb der Leistungselektronik steht hierbei der Zwischenkreiskondensator im Fokus, da dieser mit Spannungsrippeln beaufschlagt wird. In elektrischen Antrieben sind Folienkondensatoren auf Polypropylen-Basis weit verbreitet, die üblicherweise aus mehreren in Epoxidharz vergossenen Kondensatorwickeln bestehen.

In dieser Arbeit wird ein Modell zur Vorhersage der spannungsinduzierten akustischen Anregung von Folienkondensatoren vorgestellt. Dazu lässt sich ein aus der Literatur bekanntes Sensormodell zunächst auf einen Plattenkondensator übertragen, um die Deformation in einer einzelnen Kondensatorschicht analytisch herzuleiten. Dieses Modell berücksichtigt neben den elektrostatischen Anziehungskräften der Elektroden auch elektromechanische Kopplungen im Dielektrikum, die auf Basis der elektrostriktiven Parameter beschrieben werden. Anschließend können die analytisch berechneten Deformationsamplituden mithilfe von Finite-Elemente (FE) Simulationen auf die Geometrie eines Kondensatorwickels übertragen werden. Die Verwendung eines FE-Modells ermöglicht es, die strukturdynamischen Eigenschaften verschiedener Kondensatorgeometrien zu berücksichtigen. Da Folienkondensatorwickel aus mehreren tausend Schichten bestehen, werden die FE-Modelle vereinfacht, sodass die modale Superposition als Modellreduktionsverfahren angewendet werden kann. Ziel ist es, die numerische Effizienz der Simulation zu erhöhen und somit größere Kondensatorstrukturen mit geringem Ressourcenverbrauch zu simulieren.

Das resultierende Anregungsmodell wird im Anschluss durch Messungen sowohl auf Wickelebene als auch auf Kondensatorebene validiert und kann zur Vorhersage der Anregung von Polypropylen-basierten Kondensatoren eingesetzt werden. Zudem lässt sich die resultierende Luftschallabstrahlung von Kondensatoren auf Basis der Anregung abschätzen.

Akustische Messungen an Kondensatorwickeln zeigen zudem, dass die Anregungsamplitude von der Polarität der angelegten Gleichspannung abhängig ist. Demnach müssen (insbesondere für kleine Spannungen) auch Polarisationseffekte im Dielektrikum berücksichtigt werden, die durch den Herstellungsprozess der metallisierten Kondensatorfolien verursacht werden können. Die Polarisation wird sowohl durch Raumladungen im Dielektrikum als auch durch eine Grenzschicht im Bereich der Metallisierung hervorgerufen und führt zu einem intrinsischen elektrischen Feld, das die akustische Anregung der Wickel beeinflusst. Diese Grenzschicht wird im Rahmen der Arbeit mittels hochauflösender Transmissionselektronenmikroskopie nachgewiesen.

Darüber hinaus kann der akustische Einfluss der im Kondensatorwickel vorhandenen Polarisation genutzt werden, um eine entsprechende Kompensationsspannung zu bestimmen, die zur Aufhebung der Polarisation benötigt wird. Diese Spannung kann entweder durch Spannungsimpulse oder Temperaturbelastungen extern beeinflusst werden, was in weiteren Experimenten untersucht wird. Die Stabilität der Kompensationsspannung über die Zeit wird ebenfalls analysiert, und verschiedene Relaxationsmechanismen werden diskutiert. Das Verhalten der Kondensatorwickel kann mit der Langzeitstabilität von Elektreten verglichen werden. Die vorliegenden Untersuchungen basieren auf Polypropylen-Kondensatoren, sind aber im Wesentlichen durch Anpassung der Kennwerte auch auf andere Dielektrika übertragbar.

Die in der Arbeit gewonnenen Erkenntnisse ermöglichen eine Vorhersage der Anregungsamplituden von Folienkondensatoren. Das vorgestellte Modell kombiniert verschiedene Anregungsmechanismen und berücksichtigt auch die durch den Herstellungsprozess verursachte Polarisation. Die Ergebnisse bilden eine Grundlage für die Berücksichtigung von Zwischenkreiskondensatoren im elektrischen Antriebsstrang als akustische Anregungsquelle.

Acknowledgements

This thesis was written during my time as an industrial PhD student at BMW and originated in cooperation with the Technical University of Darmstadt. This constellation enabled me to make numerous contacts both in the company and at the University of Darmstadt. I must emphasize that the success of the work was crucially dependent on numerous people. Therefore, I would like to thank everyone involved.

First of all, I would like to thank Prof. Dr. mont. Mario Kupnik for taking over as my first supervisor and for the trust he has placed in me. Furthermore, I also say thank you to Prof. Dr.-Ing. Thilo Bein for taking over the co-supervision and the associated technical guidance.

I would also like to thank my BMW supervisor Dr. Roland Lichtinger, who not only helped me with difficult technical questions, but also cleared bureaucratic hurdles for me. In this context, I would also like to express my gratitude to David Farmer and his entire team, the mechanical development of Inverter components.

I would also like to thank Dr. Moritz Hülsebrock and Heiko Atzrodt, who, in addition to their professional input, introduced me to the TU Darmstadt and the Fraunhofer Institute.

Special thanks also goes to my students Jakob Bonart, Patrick Eifert, Thymoty Naacke and Felix Wolf. Furthermore, the results of this thesis would not have been possible without the measurement and simulation support of Robert Heyer, Peter Olbrich, Julian Pohn and Daniel Braun.

Last but not least, I would like to thank my family, who has always supported me in my dissertation project.

Contents

Nomenclature

List of Abbreviations

AC	Alternating current
AFM	Atomic force microscope
APDL	Ansys programming design language
BOPP	Biaxially oriented polypropylene
CAD	Computer aided design
DC	Direct current
DEGA	Deutsche Gesellschaft für Akustik
DUT	Device under test
EMC	Electromagnetic compatibility
EoL	End-of-line
ERP	Equivalent radiated power
ESR	Equivalent series resistance
ESL	Equivalent series inductance
FE	Finite element
GaN	Gallium nitride
GMM	Generalized Maxwell model
IGBT	Insulated-gate bipolar transistor
IXPP	Irradiated crosslinked polypropylene

MAC	Modal assurance criterion
MEMS	Micro-electro-mechanical systems
MOSFET	Metal-oxide semiconductor field-effect transistor
MSUP	Modal superposition
NVH	Noise vibration harshness
PC	Polycarbonat
PET	Polyethylenterephthalat
PEU	Power electronic unit
PP	Polypropylene
PPS	Polyphenylensulfid
PWM	Pulse width modulation
SiC	Silicon carbide
SEM	Scanning electron microscope
SMD	Surface-mounted device
TEM	Transmission electron microscope
THT	Through-hole technology

Latin characters

Symbol	Description	Unit
A	Area	m^2
a_1, a_2	Electrostrictive coefficients	-
a_{ijkl}	Electrostrictive tensor	m$^-$1
$\boldsymbol{B}$	Magnetic field vector	Vs/m^2
C	Capacity	F
$\boldsymbol{C}$	Damping matrix	Ns/m
c	Damping coefficient	Ns/m
D	Damping ratio	-
d	Plate distance	m
$d_{feature}$	Feature size	m
d_{ijk}	Piezoelectric constant	C/N
$\boldsymbol{E}$	Electric field	V/m
$\vec{F}$	Force vector	N
$F(t)$	Excitation force	N
f	Force (non-vectorial)	N
G	Shear modulus	N/mm^2
$g(\tau)$	Distribution function for Debye model	-
$\boldsymbol{K}$	Stiffness matrix	N/m
I_{AC}	Alternating current	A
i_u	Actual current signal	A
$i_{u,1}$	Target current signal	A
$i(t)$	Depolarisation current	A
$\Im$	Imaginary part	-
k	Stiffness coefficient	N/m
L_p	Sound power level	dB

Symbol	**Description**	**Unit**
m	Mass	kg
$\boldsymbol{M}$	Mass matrix	kg
$P(t)$	Polarization	C/m^2
Q	Charge	C
Q_{ijmn}	Electrostrictive coupling tensor	m^2/V^2
$\Re$	Real part	-
S	Surface area	m^2
s_i, s_j	Deformation in i,j	m
$\boldsymbol{S}$	Poynting vector	-
t	Time	s
U	Electric voltage	V
U_{DC}	DC voltage	V
U_{AC}	AC voltage	V
U_{comp}	Compensation voltage	V
u	Displacement	m
$\dot{u}$	Velocity	m/s
$\ddot{u}$	Acceleration	m/s^2
v_{avg}	Average surface velocity	m/s
v_i	Complex surface velocity	m/s
v_n	Normal surface velocity	m/s
W_{rad}	Radiated sound power	W
Y	Young's modulus	N/m^2
$\|Z(\omega)\|$	Impedance	Ω

Greek characters

Symbol	**Description**	**Unit**
δ_{ij}	Partial derivative	-
ε	Permittivity	As/Vm
ε_0	Permittivity of vacuum	As/m
ε_c	Permittivity of cavities	As/m
ε_r	Material-dependent permittivity	As/m
ϵ	Strain	-
$\epsilon_{\parallel}$	Capacitor strain parallel to electrical field	-
$\epsilon_{\perp}$	Capacitor strain perpendicular to electrical field	-
η	Frequency ratio	-
κ	Sweep rate	s^-2
π	Permanent dipoles	A/m^2
ρ	Density	kg/m^3
ρ_c	Distribution of charges	A/m^2
λ	Eigenvalue	-
λ_w	Wavelength	m
μ_0	Magnetic field constant	N/A^2
ν	Poisson ratio	-
Ξ	Radiation efficiency	-
σ	Stress	N/m^2
σ_{ij}^0	Stress in ij in non-deformed state	N/m^2
ς	Entry in Maxwell stress tensor	N/m^2
τ	Relaxation time	s
$\tan\delta$	Dissipation factor	-
Φ	Phase angle	-
φ_1, φ_2	Displacement vector 1,2	-
χ	Susceptibility	-
χ''	Imaginary part of susceptibility	-
ω	Natural frequency	1/s
∇	Nabla operator	-

Chapter 1

Introduction

1.1 Motivation

What association does the term *Electromobility* spontaneously bring to your mind?

According to a study from Götz et al. [32], the majority of customers expects - besides environmental friendliness - a noiseless driving experience. Regarding the overall driving noise of electric vehicles, this is not necessarily the case. Studies conclude that electric vehicles are not quiet in general and above speeds of 25 kilometres per hour, their noise emission is not significantly lower compared to combustion engine vehicles [117].
However, the sound impression of electric vehicles is considerably different to vehicles with combustion engines. Several studies show that interfering noise gets more prominent in combination with electric cars since the masking effect of the engine is missing [28, 72].
Taking into account findings from psycho-acoustic investigations, especially tonal noise may be perceived as extremely annoying. Since the conversion of the current within the power electronic unit (PEU) is based on pulse width modulation (PWM), certain carrier frequencies are used and lead to harmonic oscillations of the supply current. Within the air gap field between rotor and stator of the electrical machine, these harmonics lead to oscillation forces. The mechanism of PWM-induced interfering noise in the air gap field has been examined in various publications [12, 67, 118].
Besides current-driven oscillations in the air gap field, there are also excitations inside the PEU. In this context, especially the DC-link film capacitor is excited by ripple voltages corresponding to the switching strategy within the inverter. For a comprehensive consideration of all PWM-induced noise sources, one has to include this component. This is even more important regarding highly integrated electrical drives, where the different sources of acoustic interfering noise cannot be separated. The drivetrain of the 5th generation from the BMW group and the packaging is shown in Fig. 1.1.

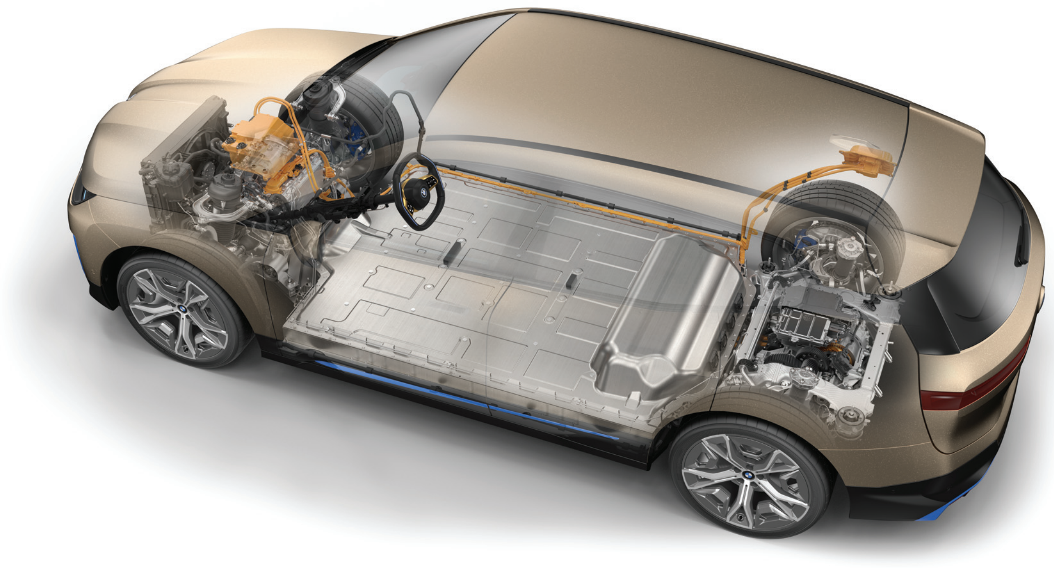

Figure 1.1: Exemplary electric vehicle with a highly integrated drivetrain [6].

This drivetrain provides a good example of a high integration level, since PEU, gearbox and electrical machine are all integrated in one housing. As a result, acoustic noise from the drive unit can reach the driver in the form of both structure-borne noise and airborne noise. A premium vehicle manufacturer in particular is motivated to consider all relevant excitation mechanisms within the drivetrain. The main focus is on effectively reducing noise as it arises, since this eliminates the need for further measures such as the installation of absorbers or the use of additional insulating material. Therefore, the focus should be on preventing interfering noise from occurring in the first place.

1.2 Goals of this thesis

The main objective of this work is to understand the chain of effects which leads to the acoustic excitation of DC-link capacitors within the highly integrated drivetrain. In order to accomplish this task, the following steps are necessary:

- Identification of excitation mechanisms in DC-link capacitors;
- Derivation of an electromechanical excitation model and mapping of all relevant effects in the dielectric;

- Application of suitable FE models for the simulative mapping of the structural-dynamic and acoustic behavior of film capacitors;
- Validation of the excitation models.

Another overarching goal is to predict the acoustic impact of the DC-link film capacitor based on a virtual component. This enables acoustic objectives to be taken into account and creates the basis for the acoustic simulation of capacitors. The findings of this work are integrated in a virtual design environment to support the computer aided design process of DC-link capacitors for highly integrated electrical drives. Another goal is to comprehensively understand the excitations in the DC-link capacitor. The findings within this work for the excitation of polypropylene-based capacitors can also be applied to other areas outside of acoustics. Thus, individual measurement methods developed in this work can be used for monitoring the production process of film capacitors. This idea will be taken up again in the conclusion of the work.

1.3 Method and structure

After the introduction, **Chapter 2** evaluates the current state of research on film capacitors with a focus on polypropylene as a dielectric. The capacitors are based on films made of biaxially oriented polypropylene (BOPP), which has special mechanical and electrical properties due to the high degree of stretching. The sub-areas of acoustics, electromechanical couplings and polarization effects are discussed based on this material.

The basic principles presented in the state of the research are used to derive an acoustic excitation model for film capacitors, which is presented and validated within **Chapter 3**. For a first approach, the excitation model is developed based on a plate capacitor representing a single film and then transferred to a capacitor stack. As a next step, the resulting deformations are carried over to finite element (FE) simulations in order to consider capacitor winding geometries. Furthermore, validation measurements are conducted on a capacitor winding level and confirm an electrostrictive approach. In addition, methods are presented to simplify the presented FE simulations via modal superposition and thus make them numerically more efficient.

In **Chapter 4**, the excitation models are applied for capacitor stacks and the results are compared to vibrometer measurements. It is shown that the modal behaviour of the investigated capacitor geometry can be predicted well applying FE simulation models. In addition, the sound radiation of DC-link capacitors within the electric powertrain is discussed. Furthermore, a laser vibrometer measurement shows how the sound wave propagates based on a typical excitation mode of the DC-link capacitor.

Chapter 5 discusses the influences of polarization effects on the acoustic excitation of film capacitors. Therefore, a measurement setup is presented to determine the so-called compensation voltage resulting from the polarization. Experiments show that the compensation voltage in the capacitor winding is influenced by high voltage pulses and temperature loads. Furthermore, the measured polarization effects are partially stable over longer periods of time, which can be traced back to an interface layer in the metallized capacitor film.

In **Chapter 6**, the results are interpreted and the key research questions of this work are answered. Furthermore, potential fields of application for the findings are discussed and present an outlook to this work.

Chapter 2

Fundamentals

2.1 Acoustical characteristics of highly integrated drives

Since electric powered vehicles are becoming more and more important, new sources of acoustical noise appear in the drivetrain. With the elimination of the combustion engine, other noise sources come to the fore that were previously masked by the engine sound. These include high-frequency tonal noise generated by the inverter control system. The cause of this noise can be traced to the switching operations of the power electronics, which electromagnetically excite components within the power electronic unit (PEU) as well as the rotor and the stator of the electric motor [40, 50, 68, 69].

The investigations in this thesis focus on the excitation within the power electronics. Therefore, the influence of voltage harmonics caused by switching operations is analysed since they excite the DC-link capacitor. Within the PEU of an electric drivetrain, polypropylene film capacitors are used as an intermediate buffer to protect the high-voltage battery and are thus exposed to voltage fluctuations [87].

The electrified drivetrain converts the electric energy provided by the battery to mechanical energy. For this reason, the DC voltage of the battery has to be converted into an AC voltage with variable frequency and amplitude to control the rotational speed and the engine load. In the context of the present work, the electric drivetrain refers in particular to an electrified axle, which includes the components power electronics, gearbox, rotor and stator. The term highly integrated refers to a dense package of these components, which are all included in one central housing. Although this has lots of advantages in terms of weight, efficient cooling, packaging and costs, it also leads to new challenges in the field of acoustics. The major problem is that within highly integrated drives, various sources of interfering noise interact with each other and crosstalk between the components cannot be neglected. To illustrate the structure of an exemplary highly integrated powertrain, the fifth generation of BMW's electrical axle is shown in Fig. 2.1.

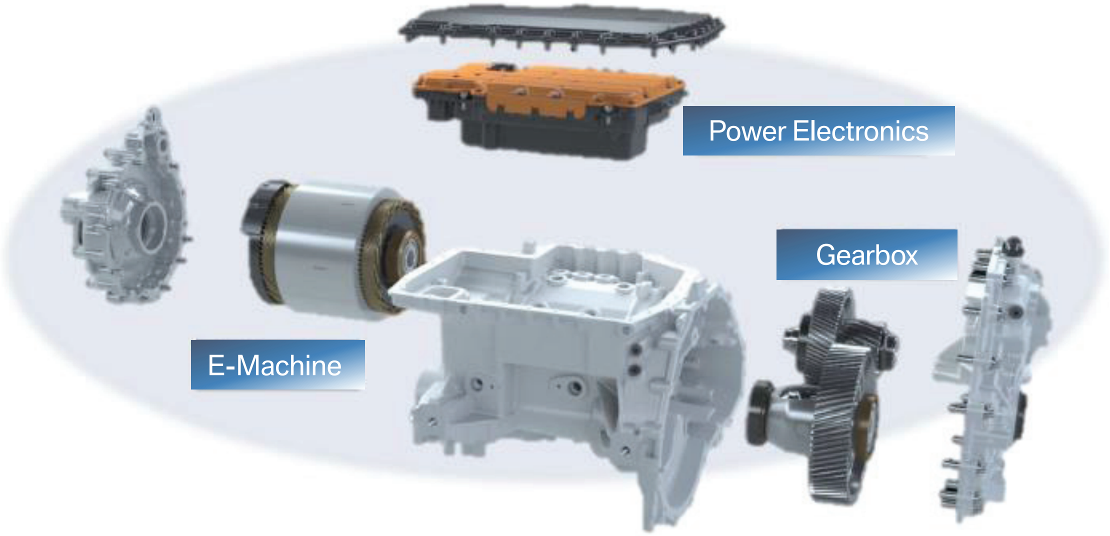

Figure 2.1: Fifth generation of the BMW highly integrated drivetrain. Electrical machine, gearbox and power electronics are integrated in one central housing [60].

Within the electric drivetrain, the different components can all contribute to interfering noise. However, the excitation mechanisms of electrical machine, gearbox and power electronics differ. Although this work is particularly dedicated to noise caused by DC-link capacitors, the existing literature in the field of noise, vibration and harshness (NVH) for other components will be briefly discussed to differentiate between the excitation mechanisms.

2.1.1 Acoustical properties of electrical drives

In general, the acoustic characteristics of electrical drives have been addressed in numerous publications. For a detailed derivation of the Maxwell forces inside rotor and stator, it can be referred to the work of Gieras [30]. Further investigations also focus on numerical approaches to predict the radiated sound power of electrical machines [1, 12, 24, 25, 68, 96].
The conversion of direct current (DC) to alternating current (AC) is realized within power electronics by pulse width modulation (PWM). By selective switching of transistors (e.g. IGBTs, MOSFETs, Thyristors), the conversion of the current is realized. Depending on the clock or carrier frequency f_c, this sinusoidal alternating current contains harmonics which excite both the electrical machine and components within the power electronics to vibrate. In the simplest case, the on and off switching points of a transistor can be represented by the convolution of a sine with a sawtooth signal. However, a sinusoidal phase current can only be approximated, which leads to harmonics. This example is illustrated in Fig. 2.2.

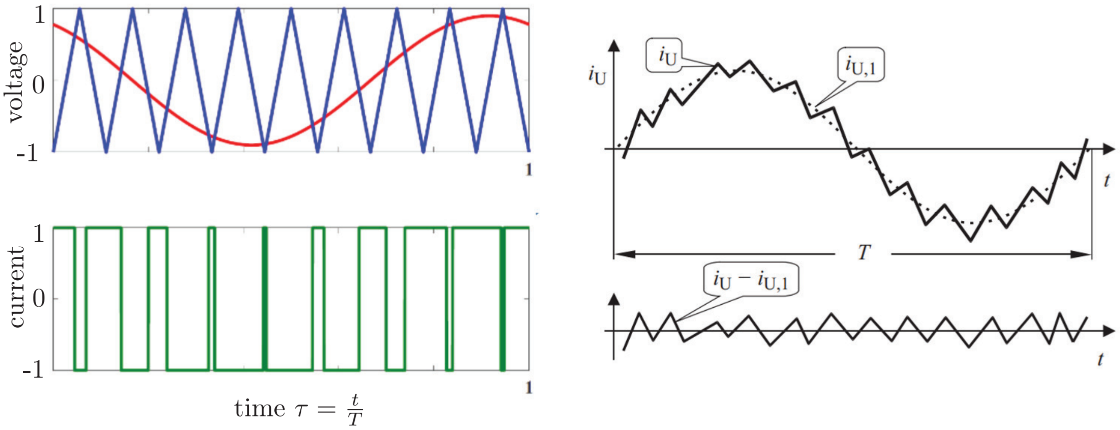

Figure 2.2: Principle of switching harmoncis caused by pulse width modulation. The target signal $i_{U,1}$ and actual signal i_U differ depending on the clock frequency [105].

Here, the voltage can be switched on and off at certain times to simulate a sinusoidal current by block functions. If the switching time is neglected and infinite switching speed is assumed, the caused harmonics have the same frequency as the carrier frequency. Nevertheless, the switching time is relevant for the electrical system, especially for electromagnetic oscillations and their influence on the electromagnetic compatibility (EMC) [55, 122].

Apart from the current-driven excitation in the air gap field between rotor and stator, the gearbox and also the bearing system provide potential sources of interfering noise. Those phenomena have been widely studied in literature and also lead to acoustic problems in electric vehicles. The first models have been presented by Harris [34] while Kahraman and Singh [61] extended them to a non-linear approach. Advanced modelling of gearbox excitation has been presented by Liu et al. [77] and Wei et al. [125].

2.1.2 Acoustical excitation within power electronics

The acoustical excitation, which is ascribed to the inverter, is based on noise caused by pulse width modulation (PWM). However, one must distinguish between two chains of effects, which are based on different physical effects. PWM-induced noise can either arise due to varying Maxwell forces in the air gap between rotor and stator due to current harmonics or can be attributed to the electromechanical excitation within passive components due to voltage harmonics. The latter are the focus of this work and originate especially from the DC-link capacitor within the PEU. The chain of effects for PWM-induced high frequent inverter noise is summarized in Fig. 2.3.

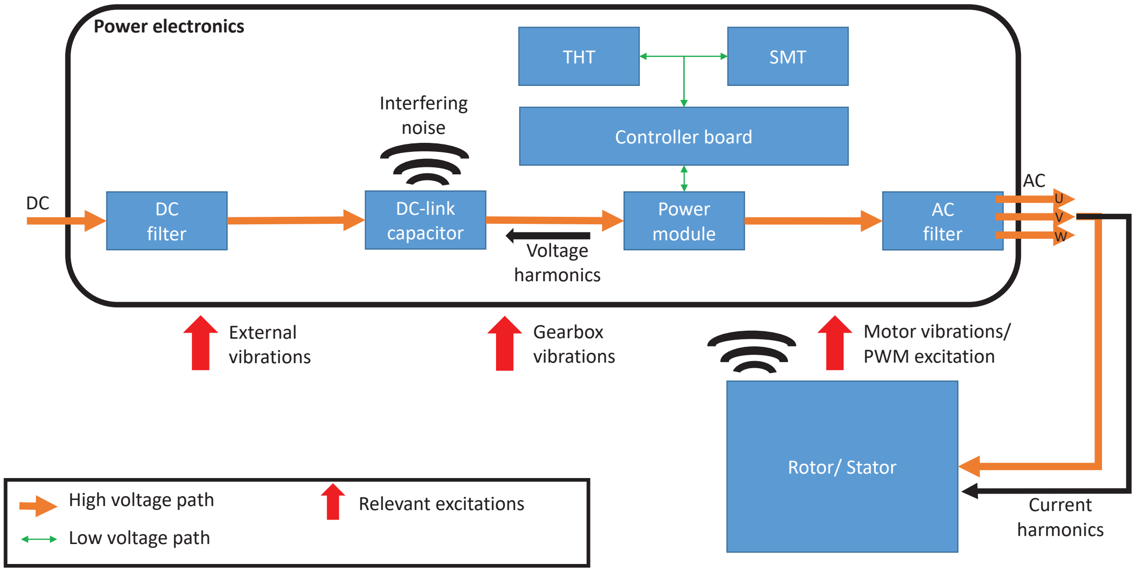

Figure 2.3: Representation of the mechanically relevant components in the inverter. Focus of this work is the DC-link capacitor, the excitation of the controller board is investigated by Hülsebrock [49].

For the acoustic assessment of electric drives, the PEU plays a role both as a potential excitation source and as a transfer path. For a transfer path analysis of the PEU, the interfaces to the surrounding structure are relevant. Exemplary interfaces for acoustic transfer are:

- Mounting points of the PEU;
- AC busbars for the stator supply;
- DC busbars for the connection to the battery;
- Cooling water connection;
- Signal cable.

All these interfaces can provide bridges for structure-borne sound, which can affect the overall acoustic impression of the vehicle [3]. In addition to structure-borne noise transmission, the DC-link capacitor is also a source of airborne interference noise. This topic has been addressed in literature in the context of power supply applications, where high voltages also lead to an electroacoustical excitation [46, 76, 102].
Acoustic noise excitation has also been examined in the context of solar inverters. One possible solution lies in the different PMW processes that are used. For example, tonality and amplitude of the noise can be reduced by using randomized carrier frequencies. Another possibility is to set

the carrier frequency outside the audible range (above 20 kHz). However, this is usually associated with poorer efficiency and more problems due to electromagnetic compatibility (EMC) [54, 78]. Additionally to the DC-link capacitor analysed in this work, the mechanical design process of power electronics includes also other components, especially printed circuit boards and the components placed with through-hole technology (THT) and surface-mounted devices (SMD). Complex models are required for the complete simulative representation of these essential components of the power electronics, which can be represented using methods from the state of research [47].

2.2 DC-link capacitors

Besides the electrical machine, coils and capacitors within power electronics are also a potential source of acoustic excitation [16, 130]. In power electronics, DC-link capacitors are used to protect the battery from ripple currents caused by semiconductor switching operations. The configuration of the switching transistors with freewheeling diodes and the DC-link capacitor providing the commutation cell is shown in Fig. 2.4.

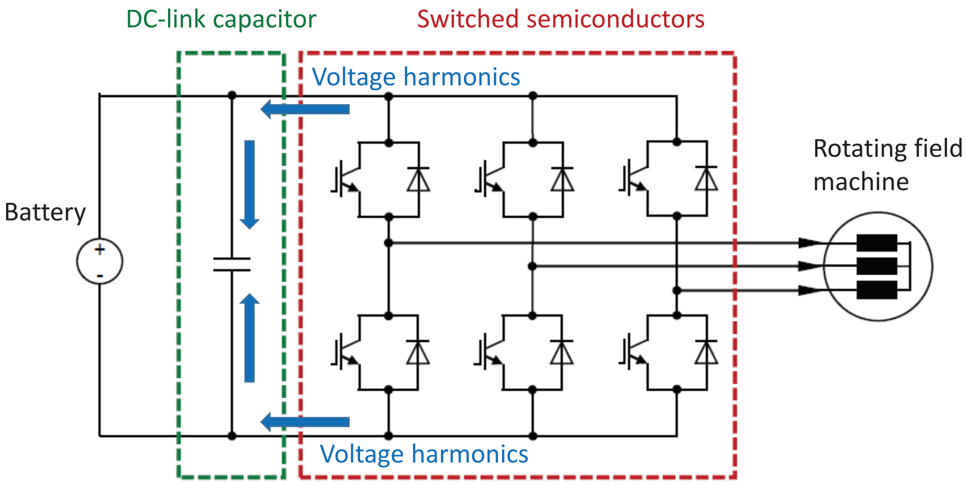

Figure 2.4: The capacitor is located on the DC-side to protect the battery from ripple voltages triggered by switching operations of the power modules.

The DC-link capacitor also represents a low-inductance energy reservoir for efficient switching operations of the semiconductors. The inductance of the so-called commutation cell is composed of the inductance of the DC-link capacitor and the inductance of the electrical connection to the power modules. The total inductance must always be kept to a minimum, otherwise the switching losses in the power semiconductors will increase. This is particularly important for fast-switching semiconductors, in particular if they are based on silicon carbide (SiC) or gallium nitride (GaN) technology. In addition, with a low inductance in the commutation cell, there is less risk of problems in the area of electromagnetic compatibility. An important design rule for reducing inductance is that the two opposing potentials are always kept in parallel at a small distance apart, ideally also within the DC-link capacitor. From an electrical point of view, it is therefore advisable to keep the capacitor windings as flat as possible. However, it must be considered that the capacitance density per volume decreases, and a compromise must be found in the vehicle between packaging efficiency and a low inductance design.

2.2.1 Polymeric metallized film capacitors

Capacitors in power electronics require high cycle stability and high safety requirements. For this reason, polymeric metallized film capacitors are state of the art for high voltage applications. The first polymeric capacitors go back to 1954 and and have been continuously developed since then [31]. Common dielectric materials for polymeric capacitors and their electrical and thermal key parameters are summarized in Tab. 2.1.

Polymer film	**Dielectric constant**	**Breakdown strength [MV/m]**	**Dissipation factor @ 1 kHz [%]**	**Operating temperature [°C]**
PP	2.2	640	0.02	-55 to 105
PET	3.3	570	0.5	-55 to 125
PC	2.8	528	0.15	-55 to 125
PPS	3	550	0.05	-55 to 200

Table 2.1: Selection of the most common dielectrics for film capacitors [31].

Most recently, biaxially oriented polypropylene (BOPP) has become the standard choice for capacitors used in high-voltage applications since it fulfils the following requirements [82]:

- Low dissipation factor;
- Self-healing ability;
- Applicable at a wide temperature range (typically -40 to 105 °C);
- Robust construction for high performance;
- Excellent pulse handling capability.

A review on the different technologies and materials used for film capacitors with a focus on BOPP is presented by Gnonhoue et al. [31]. New studies are currently focusing on materials with higher maximum temperatures. Promising results are being obtained with polysulfates, for which temperature ranges of 150 to 250 °C are possible according to current research. This is beneficial for

higher efficiency in the electric powertrain, as the cooling capacity can be reduced [74].
The self-healing ability of dielectric films can be further enhanced by a segmentation of the metallization. As a result, one of the electrodes is made out of small segments connected by small webs. A common example is shown in Fig. 2.5 [5].

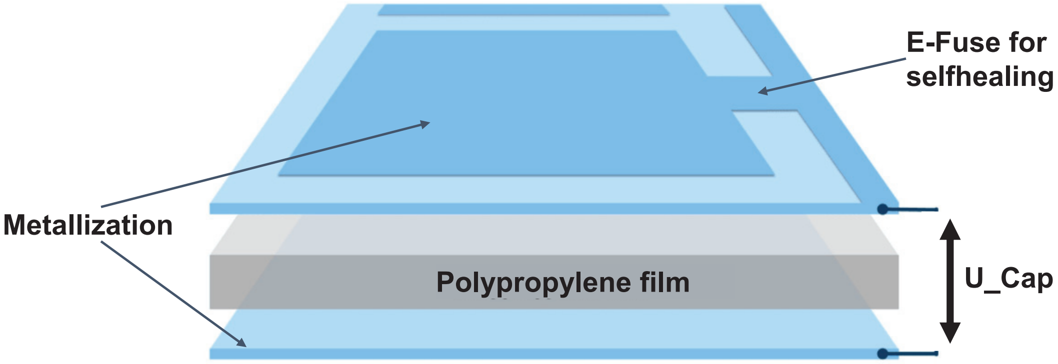

Figure 2.5: Cross-section of double-sided metallized PP film with self-healing structures [85].

These small connections are working as fuses. If there is a short circuit because of a failure of the dielectric in one segment, this leads to a high current at the segment connection, respectively the E-Fuse. Due to this high current, the fuse overheats and disconnects the segment from the rest of the capacitor. This ensures that only a small part of the capacitance is lost through weak points in the dielectric. Segmentation is not always necessary, since polypropylene has self-healing properties even without these complex metallization profiles. However, segmentation allows the film thickness to be reduced, which is conducive to the desire for increasingly compact designs within automotive applications. A state-of-the-art segmented BOPP film thickness used for applications up to 450 V is 2.0 to 2.2 μm, for 850 V systems the thickness is in the range 3.0 to 3.3 μm.
If the bobbin structure is neglected, the capacitor can be represented as a plate capacitor. The homogeneous electrical field E inside this plate capacitor depends on the potential U and the distance d separated by its electrodes. This can be written as

$$E = \frac{U}{d}. \tag{2.1}$$

A simple plate capacitor consists of two parallel plates at a distance d and a dielectric with known permittivity ε_r. The capacity C of a capacitor for a given plate area A can be optimized either by choosing a dielectric with high relative permittivity or by reducing the plate distance and is obtained according to

$$C = \frac{\varepsilon_0 \varepsilon_r A}{d}. \tag{2.2}$$

2.2.2 Structure and manufacturing process

In order to derive an acoustical excitation model, the structure of film capacitors has to be regarded. This design is explained based on polypropylene-based capacitors, which are currently the most widely type used in the automotive industry. The production process can be divided into three overarching steps:

- Production and metallization of the film;
- Production of the capacitor winding;
- Assembly of the capacitor.

One of the major challenges is the metallization of the film. In order to support the adhesion of the electrode layer to the polypropylene, the polymer is commonly pre-treated with a plasma activation process. In addition to capacitor production, similar processes are also used for food packaging, where metallized PP is also used due to its better properties compared to conventional PP [62, 107, 109, 110].

The metallization is achieved by vapor deposition of pure aluminum or alternatively a combination of aluminum and zinc. The thickness of the metallization varies depending on the required current carrying capacity. A thicker metallization layer increases the current carrying capacity and reduces the equivalent series resistance (ESR), but it also affects the self healing properties of the winding. Since the currents vary over the winding height, the thickness of the metallization is usually also varied. This variation is called wedge vaporization and is a way to improve the current carrying capacity of the windings with minimal material usage. The structure of a winding with wedge vaporization is shown as an example in the appendix in Fig. A.1.

During the production of the windings, two single-sided metallized polypropylene films are laid on top of each other with an offset and then wound up. The offset is called free margin and is relevant for the insulation of the two potentials, since otherwise a creepage distance would occur across the film edges. By offsetting the two films, it is possible to represent opposing electrical potentials at each end of the winding. Each potential is contacted via the so-called Schoop layer, which goes back to the inventor Max Ulrich Schoop [104]. The exemplary cross-section view of a film capacitor winding is illustrated in Fig. 2.6

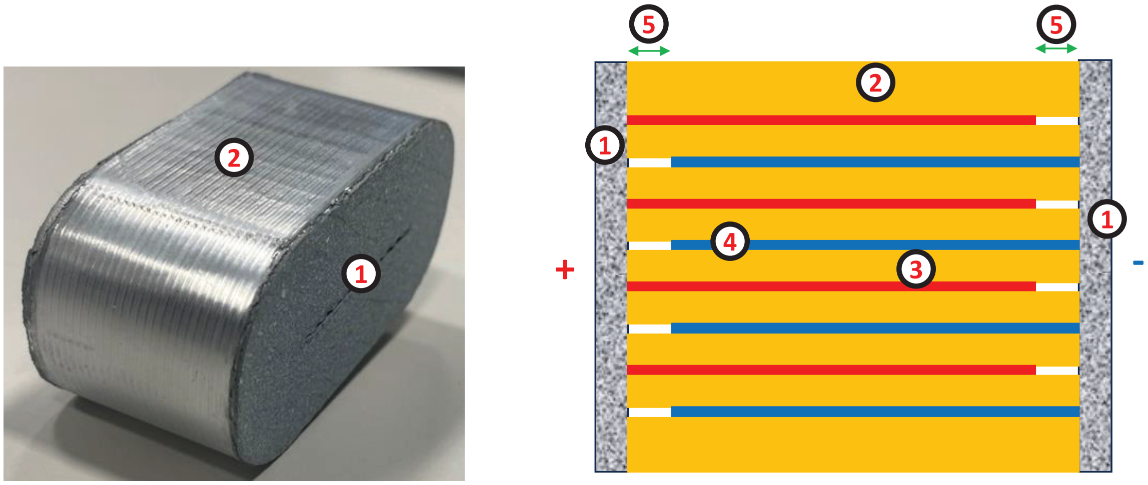

Figure 2.6: Structure of an exemplary film capacitor winding: 1) Schoop layer 2) BOPP protection film 3) BOPP dielectric film 4) Metallized electrode 5) Free margin

For the Schoop layer, usually a zinc-aluminium alloy is sprayed onto both capacitor ends. For better protection against environmental influences, BOPP (without metallization) is also used as a protective film on the capacitor edge by placing it around the winding several times at the end of the winding process.

The shape of the winding is usually not round but elongated, as this achieves a higher capacitance density in rectangular installation spaces. The exact manufacturing process of capacitor windings depends on the manufacturer. The usual steps are shown in Fig. 2.7. It should be noted at this point that a high voltage is applied in the healing step (step six) in particular, which burns out defects in the capacitor. For this purpose, twice the nominal voltage is usually applied. The intensity of this process is also important for the acoustic excitation, as will be explained in more detail in the course of this work since it has an influence on the internal winding polarization.

In addition, a repeated voltage pulse is used for the electrical end test (step ten) to test the insulation capacity, but the voltage applied is usually lower than in the healing process. Usually one and a half times the nominal voltage is used. In addition, electrical parameters such as capacitance, dissipation factor and impedance are determined in the end-of-line (EoL) test.

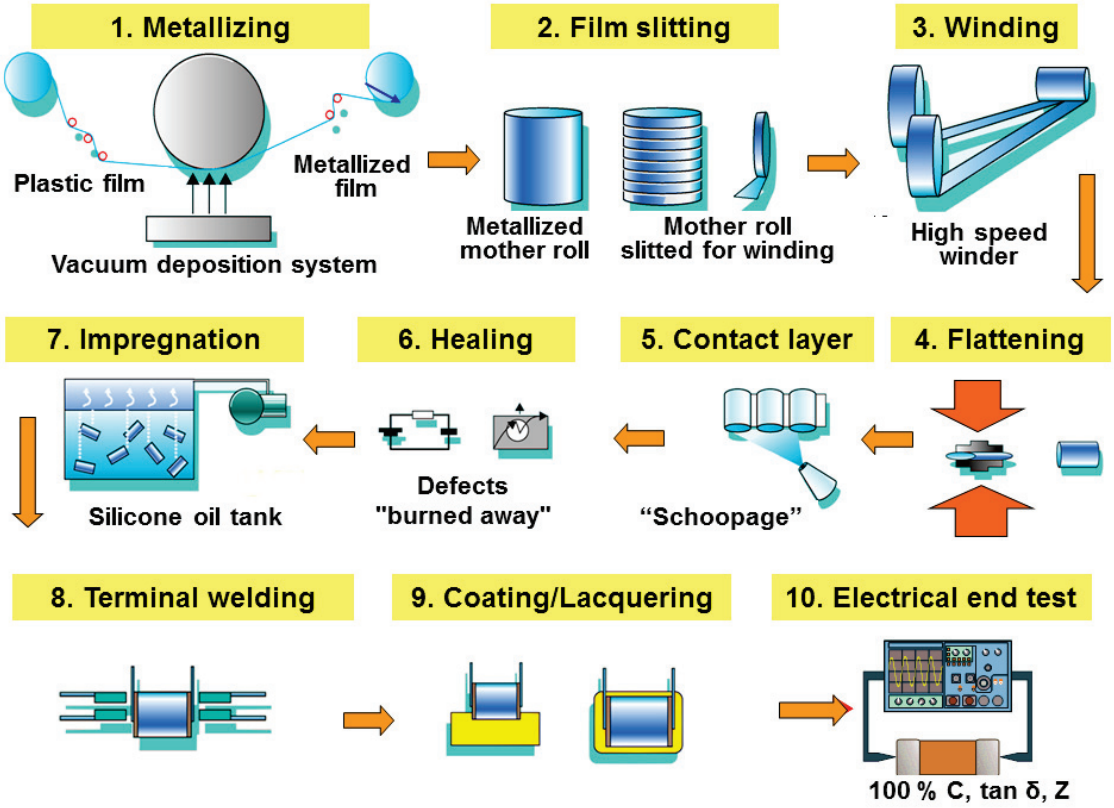

Figure 2.7: Exemplary representation of the production steps of standard capacitor windings [13].

The separately produced windings are usually connected in parallel and contacted with copper busbars at their Schoop layers. This connection between Schoop layer and copper busbar is normally realized by a soldering process, which makes it possible to compensate geometric tolerances introduced by the winding process. To ensure the lifetime requirements of the capacitors under any environmental influence, the contacted winding packages are inserted into a plastic housing and protected with the aid of a potting compound, typically an epoxy-based matrix with additives to ensure a good thermal conduction and low flammability. This structure for film capacitor stacks is shown in Fig. 2.8.

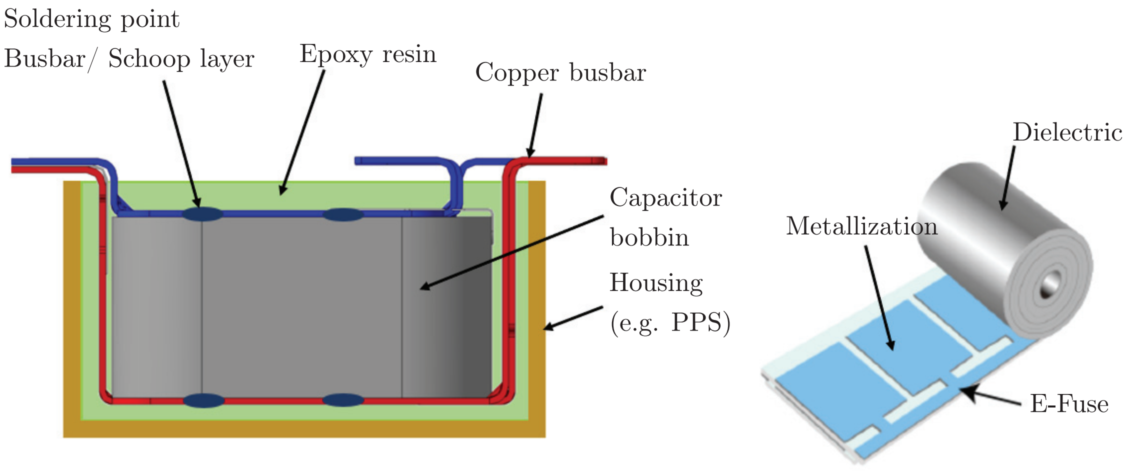

Figure 2.8: Structure of capacitor assembly with plastic housing and epoxy sealing. Bobbin view taken from [85].

The exact composition of the potting compound is usually a well-kept secret of the respective manufacturer and usually contains some additives. Basically, the potting compound must ensure the following properties:

- Good thermal properties for heat dissipation;
- Electrical insulation;
- Low humidity absorption;
- High tracking resistance;
- Mechanical compatibility with the housing material.

Usually, a bubble-free and evenly distributed potting is mandatory to pass the environmental and life cycle tests, which are relevant for film capacitors used in automotive applications. An overview of the environmental tests carried out is provided by the ZVEI [131]. The validation according to ZVEI includes the following sub-tests:

- Temperature cycling test;
- Humidity biased test;
- High temperature operational lifetime test;
- Vibration test;
- Short circuit test.

2.2.3 BOPP as dielectric in film capacitors

Polypropylene is produced from propene by chain polymerization and is both semi-crystalline and non-polar in its initial state. For film capacitors, extremely thin polypropylene films are used. For this reason, the film is stretched in two directions resulting in biaxially oriented polypropylene (BOPP). In order to produce BOPP, a thin film of polypropylene is extruded and then stretched to a minimum thickness of 2 µm by means of either sequential or simultaneous stretching. The stretching process is carried out either with the help of rollers or with special grippers that generate the stretching using linear motors [17, 22].
This manufacturing step also leads to cracks in the material, which are important for electric characteristics, e.g. the maximum breakdown voltage [88]. The cracks and cavities in the material play a crucial role for this work, as they can serve as charge traps and thus lead to electromechanical couplings. The development of these cracks is illustrated in Fig. 2.9.

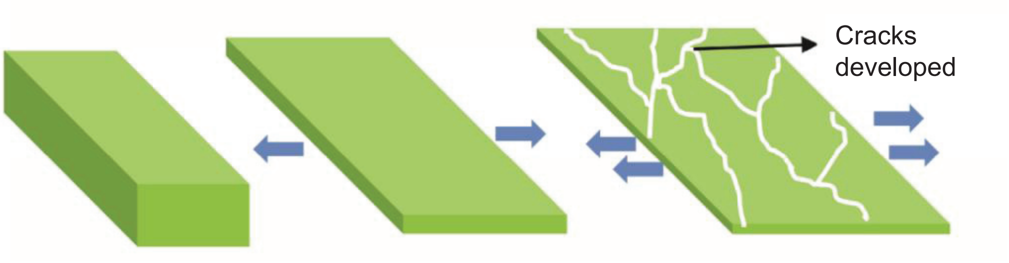

Figure 2.9: The stretching of the PP films leads to cracks inside the material. Illustration taken from [79].

The film can endure an electrical field of up to $300\frac{\mathrm{V}}{\mu\mathrm{m}}$ within automotive applications. BOPP has been widely used for film capacitor applications and is also examined in numerous publications. Recent progress is summarized in [4, 75, 126].

2.3 Acoustical and mechanical basics

In this section, the mechanical strain in BOPP-based capacitors is calculated analytically. A sensor model from Thakur et al., in which electromechanical couplings are taken into account, serves as a foundation of the excitation model [114, 115]. In addition, frequency-dependent material parameters as well as acoustic fundamentals are explained, which are relevant for the subsequent modelling.

2.3.1 Stress-strain relation

When a force is applied to a body, it will undergo deformation. The force acting on the surface of the body generates a stress, denoted as σ_{ij}. This stress leads to a deformation in the direction s_i and can be formulated for a linear elastic material, i.e.

$$\sigma_{ij} = \frac{Y}{1+\nu}\left(\epsilon_{ij} + \frac{\nu}{1-2\nu}\epsilon_{kk}\delta_{ij}\right). \tag{2.3}$$

Here, Y represents the Young's modulus, which is a measure of the material's stiffness, and ν is the Poisson's ratio, which describes the material's tendency to expand in directions perpendicular to the applied force. The deformation tensor ϵ_{ij} can be simplified under the assumption of small deformations, where the deformation is symmetric, meaning $\epsilon_{ij} = \epsilon_{ji}$. This simplification can be expressed as

$$\epsilon_{ij} = \epsilon_{ji} = \frac{1}{2}\left(\frac{\partial s_i}{\partial x_j} + \frac{\partial s_j}{\partial x_i}\right). \tag{2.4}$$

Here, $\partial s_i/\partial x_j$ represents the partial derivative of the displacement s_i with respect to the spatial coordinate x_j, which describes the strain in the material. Rearranging the initial equation, we can express the strain ϵ_{ij} in terms of the stress σ_{ij} according to

$$\epsilon_{ij} = \frac{1}{Y}[(1+\nu)\sigma_{ij} - \nu\sigma_{kk}\delta_{ij}]. \tag{2.5}$$

For orthotropic materials, the stress-strain relation has to be extended for the three spatial directions, i.e.

$$\begin{bmatrix} \epsilon_{11} \\ \epsilon_{22} \\ \epsilon_{33} \\ 2\epsilon_{23} \\ 2\epsilon_{13} \\ 2\epsilon_{12} \end{bmatrix} = \begin{bmatrix} \frac{1}{Y_1} & \frac{-\nu_{21}}{Y_2} & \frac{-\nu_{31}}{Y_3} & & & \\ \frac{-\nu_{12}}{Y_1} & \frac{1}{Y_2} & \frac{-\nu_{32}}{Y_3} & & & \\ \frac{-\nu_{13}}{Y_1} & \frac{-\nu_{23}}{Y_2} & \frac{1}{Y_3} & & & \\ & & & \frac{1}{G_{23}} & & \\ & & & & \frac{1}{G_{13}} & \\ & & & & & \frac{1}{G_{12}} \end{bmatrix} \begin{bmatrix} \sigma_{11} \\ \sigma_{22} \\ \sigma_{33} \\ \sigma_{23} \\ \sigma_{13} \\ \sigma_{12} \end{bmatrix}. \tag{2.6}$$

This relationship is called Voigt-notation in the literature and is the basis for the deformation of a linear-elastic material. The entire matrix is called the compliance matrix and depends essentially on the Young's modulus, the shear modulus and the Poisson's ratio.

2.3.2 Harmonic oscillations

If an oscillating system is excited by a time-dependent force, it will be forced into oscillation. Particularly, if the excitation is periodic, the forced oscillation will transition to a steady state after a settling time that depends on the damping of the system. In this steady state, the system will oscillate at the same frequency as the external excitation. The amplitude of the steady state oscillation depends on the ratio of the excitation frequency to the resonance frequency of the system. When the excitation frequency is close to the resonance frequency, the amplitude of the

forced oscillation can become significantly amplified, a phenomenon known as resonance.
The prediction of the structural dynamic behavior of mechanical systems is often represented using a second-order differential equation, which has gained widespread acceptance in practice. This representation offers the advantage of a clear assignment of the system matrices to the physical properties of the structure. The forced oscillations of a linear, time-invariant, mechanical system are described by the inhomogeneous equation of motion

$$\boldsymbol{M}\ddot{u} + \boldsymbol{C}\dot{u} + \boldsymbol{K}u = F(t). \tag{2.7}$$

In this equation, $\boldsymbol{M}$ represents the mass matrix of the system, $\boldsymbol{C}$ is the damping matrix, $\boldsymbol{K}$ is the stiffness matrix, u is the displacement vector, and $F(t)$ is the time-dependent external force vector acting on the system. This general equation of motion provides a comprehensive framework for the analysis and prediction of the dynamic behavior of a wide range of mechanical systems, such as structures, machines, and vehicles. The equation of motion can be solved by using exponential functions for the force and the displacement, where Φ describes the phase angle, i.e.

$$F(t) = F_{\max}\,\exp\left(i(\omega t + \Phi)\right), \tag{2.8}$$

$$u(t) = u_{\max}\exp(i(\omega t + \Phi)). \tag{2.9}$$

If we insert these expressions into equation (2.7), we obtain the complex expression

$$\left(-\omega^2 M + i\omega C + K\right)\tilde{u} = \tilde{F}. \tag{2.10}$$

Here, $\tilde{u}$ and $\tilde{F}$ represent the complex representations of the displacement vector u and the force vector F, respectively. The expression in equation (2.10) can be simplified as an eigenvalue problem. The solution of this eigenvalue problem forms the basis of the modal analysis and can therefore be written as

$$\det(\lambda^2\boldsymbol{M} + \lambda\boldsymbol{C} + \boldsymbol{K}) = 0. \tag{2.11}$$

The eigenfrequencies can be determined from the eigenvalues of the polynomial. With the help of the eigenvectors, the mode shapes of the modes can also be represented. For simple systems such as single-mass oscillators, this procedure can also be carried out analytically. For more complex geometries, numerical aids must be used.

2.3.3 Acoustic basics

In this subsection, the acoustic basics relevant for this work will be explained. Important parameters are introduced to evaluate the acoustic excitation of capacitors. For an overview of the most important acoustical parameters and correlations, it can be referred to the collections of the German Society for Acoustics (DEGA) [23].

If a solid body starts to vibrate, it also excites the adjacent air layers and radiates sound. This process is described by the parameters sound pressure and sound velocity, which can be linked via the continuity equation

$$\rho v = -\nabla \rho. \tag{2.12}$$

Here, ρ describes the density of the medium, v is the flow velocity and $\nabla\rho$ represents the gradient of the density change. The processes in the sound field are subject to thermodynamic basic laws while airborne sound propagates as a longitudinal wave. Since the corresponding sound velocity depends on pressure and temperature, phenomena such as diffraction, refraction, reflection or scattering of the waves occur in non-isotropic atmospheres. The propagation of sound waves within solids is bound to material characteristics and therefore depends on the quantities strain, shear and stress. This can be described via various wave equations, which are also described in [23]. The schematic excitation path from a vibrating body to an airborne sound field (fluid-structure coupling) is shown in Fig. 2.10.

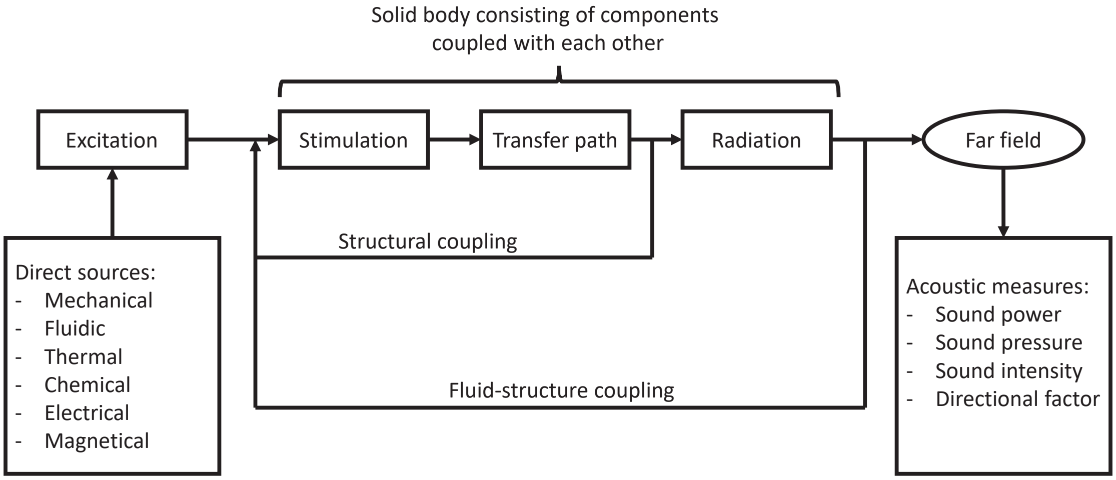

Figure 2.10: Illustration of the excitation path from a solid-state vibration to a sound radiation in the far field. Adapted illustration from [23].

If the vibrating body has a normal surface velocity v_n, the radiated surface pressure p_{rad} is a function of the density of the surrounding medium ρ_0 and the sound velocity c_0, i.e.

$$p_{\mathrm{rad}} = \rho_0 c_0 v_n. \tag{2.13}$$

The resulting pressure can then be converted to the sound pressure level L_p. For this purpose, the reference pressure $p_{\mathrm{ref}} = 2 \cdot 10^{-5}$ Pa is used, which represents an estimate of the hearing threshold at 1000 Hz, i.e.

$$L_p = 20 \log \left(\frac{p_{\mathrm{rad}}}{p_{\mathrm{ref}}} \right) \mathrm{dB}. \tag{2.14}$$

Another important criterion to evaluate the acoustic impact of a vibrating body is the emitted radiated power (ERP). This measure gives a worst case approximation for sound radiation with maximum radiation efficiency $\Xi = 1$ and can be expressed as

$$ERP = \rho_0 \, c \, \Xi(f) \int_S |v_n|^2 \, \mathrm{d}S. \tag{2.15}$$

The ERP depends on the radiation efficiency $\Xi(f)$ and the normal surface velocity of the radiating surface v_n. The frequency dependent radiation efficiency has already been approximated for film capacitor housings within the literature [130]. According to Zhu et al., the radiation efficiency $\Xi(f)$ for a given surface S can be estimated based on the feature size $d_{feature} = \sqrt{\frac{S}{\pi}}$, the sound velocity c and the regarded frequency f, which leads to the approximation

$$\log \Xi(f) = -\log(1 + 0.1 \frac{c^2}{(f d_{\mathrm{feature}})^2}). \tag{2.16}$$

In order to correctly map the transfer paths in capacitor structures, a correct description of the materials is also relevant. For a realistic representation of the electromechanical behavior of power electronic components, the material parameters must be taken into account as a function of frequency. This is especially important for viscoelastic materials, as they behave differently over different frequencies. Therefore, the complex shear modulus $G^*(\omega)$ can be divided into real part and imaginary part, which are also known as storage modulus $G'(\omega)$ and loss modulus $G''(\omega)$, i.e.

$$G^*(\omega) = G'(\omega) + iG''(\omega). \tag{2.17}$$

In general, the division into reversible processes, corresponding to the real part, and into irreversible processes, corresponding to the imaginary part, is a mathematical description, which is also used in many other fields of other areas of physics. The origin of complex material parameters can be found in the solution of appropriate differential equations. Typically, the imaginary part of these parameters corresponds to the damping behavior of the material.

2.4 Electromechanical couplings in film capacitors

This section explains which effects need to be considered to derive a film capacitor excitation model. The Maxwell stress tensor describes the generalised form of electric fields on charges and their momentum. For a detailed derivation, please refer to [33] at this point. In the two-dimensional state, an entry ς_{ij} in the Maxwell stress tensor can be calculated according to

$$\varsigma_{ij} = \varepsilon_0 \left(E_i E_j - \frac{1}{2} \delta_{ij} \boldsymbol{E}^2 \right) + \frac{1}{\mu_0} \left(B_i B_j - \frac{1}{2} \delta_{ij} \boldsymbol{B}^2 \right), \tag{2.18}$$

where $\boldsymbol{E}$ describes the electric field, ε_0 the electric field constant, $\mathbf{B}$ the magnetic flux density and μ_0 the magnetic field constant. Furthermore, the generalized force on a charge can be written as

$$\nabla \cdot \varsigma = \mathbf{f} + \varepsilon_0 \mu_0 \frac{\partial \mathbf{S}}{\partial t}. \tag{2.19}$$

Here, $\mathbf{S}$ represents the Poynting vector, which is defined according to

$$\mathbf{S} = \frac{1}{\mu_0} \mathbf{E} \times \mathbf{B}. \tag{2.20}$$

In the case of perfectly parallel electric field lines and the absence of magnetic fields, the Maxwell stress tensor represents the stored energy. The gradient of the stored energy is proportional to the force acting on charges in the environment. Plate capacitors are well-suited for realizing such a scenario. On one side, the plate generates the electric field, while the other side acts as a charged plate that is attracted to the first plate due to the Maxwell stress tensor. For dielectrics inside the capacitor, ε_0 is extended by the appropriate dielectric constant. The electrostatic forces in capacitors can be divided into [66]:

- Coulomb effect;
- Piezoelectric effect;
- Electrostrictive effect.

While the piezoelectric effect and electrostriction are caused by charge displacements within the dielectric, the Coulomb force can be simply explained by the mutual attraction of the charges of two capacitor plates. For a plate capacitor with a homogeneous electric field $\boldsymbol{E}$ and the stored charge Q this force can be calculated as:

$$\vec{F} = \frac{1}{2} \boldsymbol{E} Q. \tag{2.21}$$

In the following, a mathematical model will be presented, which takes electromechanical couplings within the dielectric into account. The Coulomb force is based on the assumption that only charges occur at the capacitor plates. However, this is not the case with PP-based film capacitors, since there are also voids and air inclusions in the dielectric.

2.4.1 Piezoelectric forces

The piezoelectric effect was discovered in the late 19th century by Pierre and Jacques Curie while investigating salt crystals [21]. Even though the piezoelectric effect is negligible for PP, it should be mentioned here to distinguish it from the electrostrictive effect. For the piezoelectric effect, a differentiation can be also made between the direct and the inverse piezoelectric effect. For the direct effect, the application of a deformation shifts the centers of charge in the crystal, inducing a voltage. In the inverse effect, the electric field induced by an external voltage leads to a deformation, which can be calculated as a function of the piezoelectric coefficients for the linear range. The strain ϵ_{ij} of a piezoelectric material exposed to an electrical field E_k can be calculated according to [88], i.e.

$$\epsilon_{ij} = d_{ijk} E_k. \tag{2.22}$$

Here d_{ijk} describes the third-order piezoelectric deformation tensor, which is material dependent. It should be mentioned that the calculation of strain using the piezoelectric coefficient only works in the linear range since hysteresis effects are not taken into account here. For this work, the inversion center in the molecular structure is not present, which is why the inverse piezoelectric effect is excluded as a potential main impact for the electromechanical excitation of a DC-link capacitor. If other materials than BOPP are used as a dielectric, this effect can become more prominent. This is especially the case for ceramic capacitors where the piezoelectric effect is the main excitation mechanism, when a ferroelectric material is applied.

2.4.2 Electrostrictive forces

The major electromechanical coupling, which is dominant in centro-symmetric crystals and amorphous solids, is called electrostriction and was first mentioned in the late 19th century. The phenomenon of electrostriction was already described by Edmund James Mills in 1887 in the context of electrodeposited metal coatings [80] and was later described mathematically by Drude and Nernst [26]. It is defined as the quadratic coupling between the electrically induced strain ϵ_{ij} and the applied electric field [114, 115].

In the literature, a distinction is sometimes made between a direct effect (mechanical excitation → electrical response) and an indirect effect (electrical excitation → mechanical response), analogous to the direct and the inverse piezoelectric effect. The terms dielectrostriction and electrostriction are used to distinguish between the two mechanical effects [70, 71].

The quadratic coupling originates from the initial polarization of the material, which then undergoes strain due to the polarization and the applied electric field. In contrast to the piezoelectric effect with constant polarization due to the lack of an inversion center, the effect of electrostriction is universal and therefore present in all materials. The mechanism of electrostriction due to polarized voids inside a dielectric is shown in Fig. 2.11.

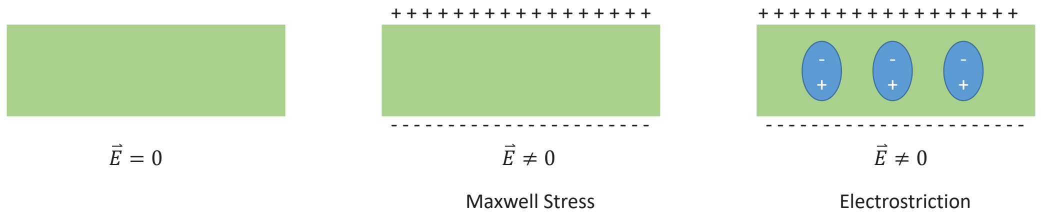

Figure 2.11: Electromechanical couplings. Adapted illustration from [114].

Electrostriction also occurs in piezoelectric materials, even though the amplitude of the excitation is negligible compared to the piezoelectric effect. For the calculation of the three dimensional strain of a plate capacitor with a homogeneous electrical field, the equations can be carried over from a sensor model introduced by Thakur and Singh [114]. In contrast to the piezoelectric effect described above, the strain due to electrostriction depends quadratically on the working electrical field. The coupling constant between the electrostrictive strain ϵ_{ij} and the electric field $\boldsymbol{E}$ is the fourth-order tensor tensor Q_{ijmn}. The effective strain can be calculated according to

$$\epsilon_{ij} = Q_{ijmn} E_m E_n. \tag{2.23}$$

The unit of this 4th order tensor is $[\mathrm{m}^2/\mathrm{V}^2]$, since the strain depends on the externally applied electric field E_m as well as on a field E_n caused by the polarization. If a dielectric material is present between two charged plates, its dielectric constant must also be taken into account. At this point, the electrostriction becomes relevant.

When electrostriction is considered, it is important to note that the coupling between field and strain is not exclusively a material property, but also depends on the geometry of the capacitor. Therefore, electrical and mechanical properties have to be combined. In the following, the most important steps will be summarized. Under small deformations of an originally isotropic material, the dielectric tensor ε_{ij} changes due to the applied strain ϵ_{kl}, i.e.

$$\delta\varepsilon_{ij} = a_{ijkl}\delta\epsilon_{kl},\ a_{ijkl} = \frac{\partial\varepsilon_{ij}}{\partial\epsilon_{kl}}. \tag{2.24}$$

Einstein's summation convention is usually used and summation is done over double indices with respect to all three spatial directions. It is common to approximate all coefficients (except the longitudinal strain coefficients a_{iiii}/a_{iijj} and the transverse shear coefficients a_{ijij}) with zero. As a result, the non-isotropic dielectric tensor can be formulated as

$$\varepsilon_{ij} = \varepsilon_r\delta_{ij} + a_1\epsilon_{ij} + a_2\epsilon_{kk}\delta_{ij}, \tag{2.25}$$

where ε_r denoted the dielectric constant for the undeformed body. If electrostriction in the material is neglected, a_1 and a_2 are equal to zero. In this case, only the Maxwell stress exists. Since electrostriction and Maxwell stress are parallel, the remaining coefficients a_{ijkl} are negligible and a direction-dependent consideration is not necessary. The result of the electrostriction is the mechanical stress σ_{ij}, which is calculated as

$$\sigma_{ij} = \sigma_{ij}^0 + \frac{\varepsilon_0}{2}\left[(2\varepsilon_r - a_1)E_iE_j - (\varepsilon_r + a_2)\mathbf{E}^2\delta_{ij}\right]. \tag{2.26}$$

If no electric field is present, σ_{ij}^0 remains for the stress. This part can be ignored if no external forces are present. As a simple example, it can be assumed that the electric field is present only in the z-direction, e.g. between the plates of a capacitor. This results in the following mechanical stresses due to the field in the body, i.e.

$$\sigma_{11} = \sigma_{22} = \sigma_{11}^0 + \frac{1}{2}\varepsilon_0\varepsilon_r\mathbf{E}^2\left(1 + \frac{a_2}{\varepsilon_r}\right) \text{ and} \tag{2.27}$$

$$\sigma_{33} = \sigma_{33}^0 - \frac{1}{2}\varepsilon_0\varepsilon_r\mathbf{E}^2\left(1 - \frac{a_1 + a_2}{\varepsilon_r}\right). \tag{2.28}$$

With the help of the stress-strain relations presented at the beginning, the electrostrictive strains can be derived accordingly. The strain in the plane (perpendicular to the electric field) and in the thickness direction (parallel to the electric field) are given by

$$\epsilon_{11} = \epsilon_{22} = \frac{1}{2Y}\varepsilon_0\varepsilon_r\mathbf{E}^2\left(1 - \frac{\nu a_1 - (1-2\nu)a_2}{\varepsilon_r}\right) \text{ and} \tag{2.29}$$

$$\epsilon_{33} = \frac{1}{2Y}\varepsilon_0\varepsilon_r\mathbf{E}^2\left((1+2\nu) - \frac{a_1 + (1-2\nu)a_2}{\varepsilon_r}\right). \tag{2.30}$$

The electrostrictive strain in an isotropic material thus represents a supplement to the Maxwell stress. The degree of electrostriction is described by the electrostrictive parameters a_1 and a_2. These can be derived with the help of the so-called Lorentz cavity approximation for a certain material with polarizable voids [15, 63, 64]. This electrostrictive approach has also been used in the literature to describe aortic walls by Lenz et al. [73].

2.4.3 Electrostrictive coefficients

The electrostrictive coefficients can be approximated based on an approach from Shkel and Klingenberg [103]. The following assumptions for dielectric isotropic materials were used to derive the electrostrictive coefficients a_1 and a_2:

- Dipolar polarization is taken into account;
- The dipole moment of each inclusion is proportional to the local electric field;

- The material is isotropic;
- Each void contributes equally to the local field and the overall polarization.

Accordingly, the electrostrictive parameters for a dielectric can be calculated as follows under the above assumptions:

$$a_1 = -\frac{2}{5}\frac{(\varepsilon_r - \varepsilon_c)^2}{\varepsilon_c} \text{ and} \tag{2.31}$$

$$a_2 = -\frac{1}{3}\frac{(\varepsilon_r - \varepsilon_c)(\varepsilon_r + 2\varepsilon_c)}{\varepsilon_c} + \frac{2}{15}\frac{(\varepsilon_r - \varepsilon_c)^2}{\varepsilon_c}. \tag{2.32}$$

The equations are valid for heterogeneous media composed of two non-electrostrictive phases. This in turn results in an electrostrictive material. For ε_r, the material-dependent dielectric constant is used and $\varepsilon_c = 1$ represents, for example, air or vacuum inclusions. It should be mentioned that this model is only valid for correspondingly small deformations, since the dipoles are assumed to move analogously to the macroscopic displacement.

2.5 Polarization in dielectrics

The electrical field inside the dielectric can also be influenced by prior polarization. If a constant electric field acts on a body, electric dipoles align within this body. The response to the external field is characterized by the dielectric constant ε. It should be mentioned that the dielectric constant is not a constant in the general case since it depends on the frequency [53]. For the simplest case of an isotropic material, the polarization P depends on the dielectric constant ε_0, the material dependent susceptibility χ and the electrical field E, i.e.

$$P = \varepsilon_0 \chi E. \tag{2.33}$$

In contrast to this, materials can be referred as anisotropic when the polarization is linearly dependent on the magnitude of the field, but is not parallel to it. If anisotropic materials are polarized, an opposing field results inside the body until a stable state can be reached. In this field, electrical energy is stored. In the case of dielectrics, local dipoles are formed because electric charges cannot move macroscopically. The charges are bound to atoms or molecules and can only oscillate around their equilibrium positions, leading to the formation of local dipoles. In the presence of mobile charge carriers, such as for example in metals, local centers of charge are formed. This can occur at the ends of the body, where an accumulation of positive or negative charges can build up. Additionally, charge carrier traps at impurities in the material offer opportunities for the accumulation of charges.

As already stated beforehand, PP is not polar in its initial state. However, due to the chemical structure of the stretched BOPP film, carrier traps can be stored due to the voids present in the material. This is also concluded in [51].

2.5.1 Electrets

An electret is a permanently electrically charged dielectric or insulator. It resembles a permanent magnet, but maintains an electric charge instead of a magnetic field. The charge in the electret is generated by a process called electrification and remains stable over an extended period of time. Electrets are commonly used in electronic devices and sensors, such as microphones, speakers, and pressure sensors [83, 98, 100].

The charge of the electret can consist of real charges such as surface or space charges or can be present due to internal polarization. It must be taken into account that combinations of the two mechanisms also occur. An overview of the general charge mechanisms is provided in Fig. 2.12.

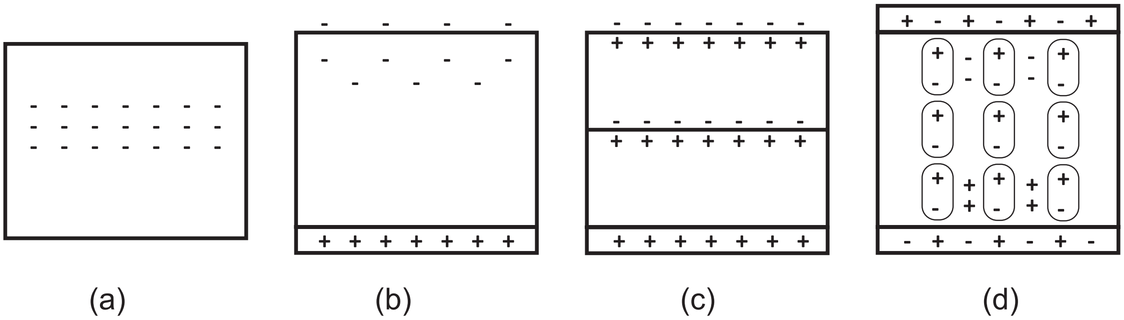

Figure 2.12: Different field storage mechanisms in electrets. Modified from [98].

Real charges are trapped in so-called trap states, which are usually located near the electrodes. These are energetically deeper traps for charge carriers from which the charges cannot thermally free themselves (a). Such space charges are often located near surfaces or contacts (b). If, on the other hand, dipoles are present in the dielectric, for example in domains or molecular structures, they can align themselves in an electric field. This is called dipole polarization (d). If the charges accumulate at domain boundaries, the phenomenon is called Maxwell-Wagner polarization (c) [92, 121].

A current method of charging an electret is presented by Chen et al. It was also found that the charging temperature also plays a role in the stability of the electret. Thus, a higher temperature during the charging process leads to deeper charge traps and a higher stability against depolarization [19].

Nowadays, electrets play a major role in acoustic membranes and small microphones. The electric field stored in the electret is used to amplify the effective amplitude. Other applications where this effect is used are sensors, microelectronic mechanical systems and energy harvesters [18, 113, 129]. Since the capacitors investigated in this work are made of BOPP, reference should also be made here to electret harvesters based on polypropylene. For example, so-called irradiated cross-linked polypropylene IXPP can be used, which has significantly stronger electret properties than BOPP. It can be assumed that the manufacturing processes during capacitor winding production favour the electret properties detected later, in particular the metallization process and the hot pressing of the windings. The polarization capability of the base film could probably be increased significantly if foamed polypropylene films were used. However, using foamed polypropylene films would not be optimal for achieving a high dielectric strength and a high dielectric constant. The increased polarization from the foamed structure would come at the expense of reduced dielectric strength and dielectric constant, which are important properties for film capacitor applications [127].

2.5.2 Detection of polarization in dielectric films

In order to evaluate the polarization inside a dielectric, several measurement techniques can be used. In the following, two of these methods will be considered in more detail, since the measurements performed in this work on the polarization of DC-link capacitors have similarities.

Thermally stimulated charging and discharging

When an electret or polymer is charged with space charges, it can store this field for a long period of time. In order to accelerate the discharge process, a thermal excitation can be used. Then, the charged electret is heated at a constant rate and the discharge current is measured. Based on peaks at certain temperatures in the current spectrum, it is possible to determine which type of relaxation process is predominant. With detailed analysis, this technique can also be used to make observations about the density or activation energy of the dipoles and the concentration of trap states can be evaluated. This measurement method can also destroy the electret if the applied heating is too high [119, 120, 123, 124].

The thermally stimulated charging/discharging (TSC/TSDC) process follows certain steps. At first, the dielectric is charged, mostly by corona charging. Then, the dielectric is cooled in order to stop the relaxation and to guaranty a steady state. After that, the discharge process can start by applying an increasing temperature load while the current flow between the two electrodes of the film is measured by an electrometer. The relaxation thus releases charges, which causes the discharge currents to spike when certain limit temperatures are reached [112, 116].

Comparable studies containing TSDC measurements based on BOPP are available in the literature. In this context, reference should also be made to the work of Ritamäki, Rytöluoto et al., which already provides relevant results for this work. Based on their measurements, discharge peaks in BOPP occur at certain limit temperatures, especially just below 90°C and 120°C [90, 91, 93, 94].

Pulsed electroacoustic analysis

Another technique for the measurement of the dynamic space charge distribution in solid dielectrics is the pulsed electroacoustic anaylsis (PEA). This method is also based on the elctroacoustic excitation of dielectric films, similar to the measurements presented within this work [52, 89].
The method was developed around 1980 and has been refined ever since to improve measurement accuracy. PEA is interesting in the context of the work because the effects of the capacitor excitation are also comparable. The schematic measurement setup of a PEA is shown in Fig. 2.13.

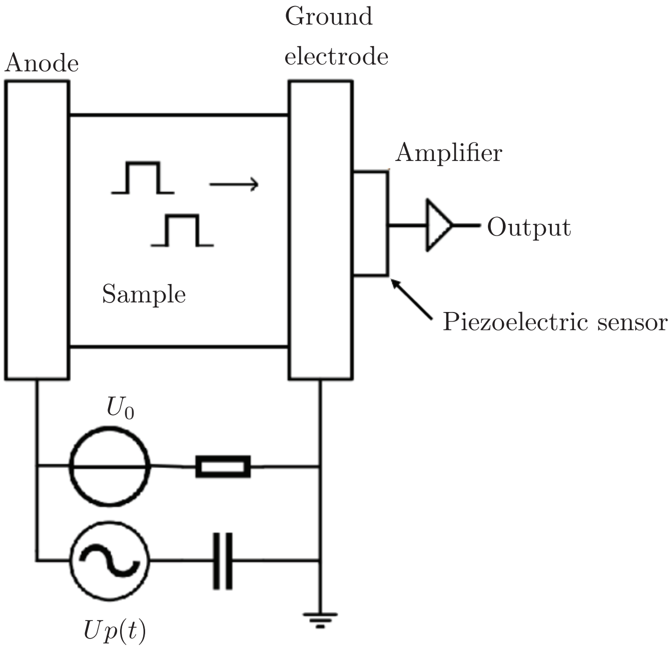

Figure 2.13: Basic Setup for PEA measurement [89].

In the measurement, the dielectric is excited via an electric field. This can be achieved analogously for a DC-link capacitor by a pulsating DC voltage. The electromechanical excitation is then recorded by sensors and provides information about the charge distribution within the dielectric. The relevant excitation effects have been discussed by Bodega et al. [7]. These effects can be summarized in equation 2.34, i.e.

$$f = \rho_c \cdot E - \frac{\varepsilon_0}{2} \cdot E^2 \cdot \nabla \varepsilon_r - \frac{\varepsilon_0}{2} \cdot \nabla (E^2 \cdot a) + \Pi \cdot \nabla E. \tag{2.34}$$

The force acting on the dielectric due to the applied electric field depends on the following parameters:

- Distribution of free charges ρ_c;
- Permittivity of the material ε;
- Electrostrictive coefficient a of the Material;
- Permanent dipoles in the material Π.

Eq. (2.34) contains a compact notation to cover all acoustic excitation effects relevant for a dielectric. These effects are valid for the DC-link capacitors investigated in this work.

Capacitance-voltage characterization

Another measuring method that can be applied to DC-link capacitor windings is the so-called capacitance-voltage measurement, also known as C-V measurement. This is often applied for electrostatic transducers [81, 101]. By varying the bias voltage and measuring the resulting capacitance, the C-V characteristic of the converter is obtained. This characteristic curve provides information about the operation and properties of the electromechanical transducer. The bias voltage is therefore an important parameter that determines the operating point of the transformer and thus influences the change in capacitance.

2.5.3 Interfacial polarization of metallized films

Besides trapped space charges at defects in the material, boundary layers can also be the reason for intrinsic polarization [27, 88]. This applies in particular to dielectrics composed of two different phases. In research, these composites are being tested for capacitors, since it is possible to combine the advantages of several different dielectrics. Promising results are shown by the investigations of Chen et al. [20].

Apart from capacitor applications, boundary layers have also been detected in other research fields. For example, Struller et al. [107–111] have investigated the use of metallized BOPP in food packaging. A boundary layer at the transition between BOPP and metallization was also detected, as shown in the transmission electron microscope image in Fig. 2.14.

The aim of metallization in the presented application is to improve water repellency, which allows food to be preserved for a longer time period. The appearance of the boundary layer depends in particular on the activation of the BOPP, for example with oxygen plasma treatment. Fig. 2.14 illustrates that activation by oxygen plasma creates a multilayer system. Based on conventional film capacitor windings for automotive applications, a TEM measurement will also be applied within this thesis. Therefore, reference to chapter 5 is made.

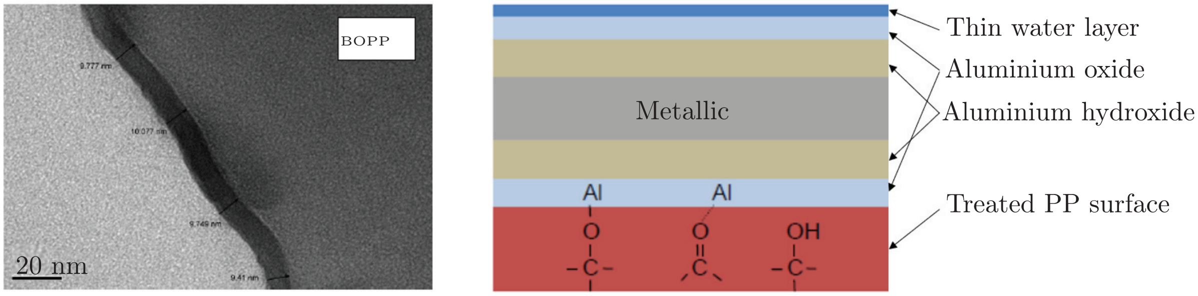

Figure 2.14: Left: TEM measurement of interface between BOPP and metallization [108].
Right: Layer model of metallized BOPP according to Struller [107].

2.5.4 Relaxation mechanisms

This section describes the depolarization mechanisms commonly mentioned in literature. Essential here are the Debye equations, which correspond to the Clausius-Mossotti equation for non-polar materials [95]. In addition, the dielectric behavior according to Jonscher is described.

Debye model

The Debye model is based on ideal dipoles which do not interact with each other and depolarize at a constant relaxation time. The model can be described analogous to Hill and Dissado [45]. It is assumed that the change rate of the polarization is proportional to the actual polarization $P(t)$ with the relaxation time τ :

$$\frac{\mathrm{d}P(t)}{\mathrm{d}t} = -\frac{P(t)}{\tau}. \tag{2.35}$$

This simple differential equation holds for an exponential approach for $P(t)$

$$P(t) = P_0 e^{-\frac{t}{\tau}}. \tag{2.36}$$

The current can be approximated with

$$i(t) = \pm P_0 \tau^{-1} e^{-\frac{t}{\tau}}, \tag{2.37}$$

wherein the ± sign states, if the dielectric is charged or decharged. In this case, the relaxation in a material is only dependent on the initial polarization. A simple variation for illustrating of an aberrant behaviour is provided by adopting a distribution of the relaxation times. Thus, the current during discharge can be expressed as

$$i(t) = -P_0 \int\limits_0^\infty g(\tau)\tau^{-1} e^{-\frac{t}{\tau}} \mathrm{d}\tau. \tag{2.38}$$

Here, $g(\tau)$ describes a distribution function of the relaxation times. A polarization P_d is defined, which can therefore be expressed as

$$P_\mathrm{d} = P_0 \int\limits_0^\infty g(\tau) e^{-\frac{t_\mathrm{d}}{\tau}} \mathrm{d}\tau. \tag{2.39}$$

Here, it is adopted that this integral is solvable. If the discharge of the polarization P_d is delayed until a point of time t_d, the discharge current $i(t \geq t_\mathrm{d})$ can be calculated according to

$$i(t \geq t_\mathrm{d}) = P_0 \int\limits_0^\infty g(\tau) e^{-\frac{t_\mathrm{d}}{\tau}} \mathrm{d}\tau \int\limits_0^\infty g(\tau)\tau^{-1} e^{-\frac{t-t_\mathrm{d}}{\tau}} \mathrm{d}\tau. \tag{2.40}$$

Therefore, eq. (2.40) can only be equivalent to eq. (2.38), if $g(\tau)$ describes a δ distribution. The difference between these equations is particularly easy to recognize if the simplest possible distribution is adopted. As a result, two Debye-relaxation times independent from each other include the depolarization rates τ_1 and τ_2. Then, eq. (2.40) can be written as

$$i(t \geq t_\mathrm{d}) = \frac{P_0}{4} \left[\tau_1^{-1} e^{-\frac{t}{\tau_1}} (1 + e^{\frac{t_\mathrm{d}}{\tau}}) + \tau_2^{-1} e^{-\frac{t}{\tau_2}} (1 + e^{\frac{t_\mathrm{d}}{\tau}}) \right]. \tag{2.41}$$

Even for this simple example it is obvious that the discharge current is dependent on the distribution of the relaxation times to a large extent and hence cannot be determined using only the initial polarization [44, 45].

Universal dielectric behavior from Jonscher

In general, it can be differentiated between two fundamental different dielectric reactions:

- Dipole relaxation;
- Discharge via charge carriers.

While the dipolar relaxation after discharge does usually not leave any remaining polarization, during discharge of charge carriers a finite polarization remains. For the universal dielectric relaxation model, which is typical for dipoles and charge carriers at high frequencies, for the time dependent decrease of the polarization a power law results. This leads to the expression

$$P(t) \propto t^{-n}. \tag{2.42}$$

This formula is based on the measurements of Jonscher, who could prove a behaviour expressed by the following equation [56–59] :

$$\chi'' \propto \omega^{n-1}. \tag{2.43}$$

Here, χ'' describes the imaginary component of the susceptibility of the material depending on the frequency. Via Fourier transformation, eq. (2.43) can be achieved as an answer within the time-domain. Most of the dielectric materials show such a behaviour when current is applied as an answer on the excitation via polarization. This behaviour can also be addressed as Law of Curie von Schweidler [97]. As within an isotropic dielectric material the polarization is proportional to the electric field and as the voltage is proportional to the electric field as well, the same behaviour over time as expressed in eq. (2.42) can be adopted for the compensation voltage. Hereby, a complete depolarization of the material is adopted for the course of time.

2.6 Major findings of this work and delimitation to the state of research

After describing the state of research relevant to the present work, this section serves as an orientation guide and summary of the contents. The aim is to clarify which newly acquired findings represent an extension of the current state of research.

An excitation model for PP-based film capacitors will be introduced in chapter 3. The basics of this model have been taken from the field of sensor modelling, where a precise calculation of the excitation amplitude is indispensible. For this reason, the electrostrictive excitation model from Thakur et al. [114, 115] has been adapted to describe the excitation of film capacitor bobbins. This results in a new excitation model for commercially used capacitor bobbins based on BOPP films in power electronics applications. The focus of this work is to fit the analytical excitation model as precisely as possible to film capacitor windings. For this purpose, the polarization of the capacitor windings is included for the first time and its influence on acoustics is examined in more detail. The results provide information about all relevant excitation mechanisms of film capacitors and can be used to reduce noise directly as it arises.

In the state of research, DC-link capacitors are not currently in focus as a primary source of excitation for electric vehicles. In order to derive a holistic excitation model for film capacitors, the following research questions are the focus of this work:

I) Can the presented model for sensor excitation be applied to film capacitors and is the electrostriction relevant?

II) Which influence does the geometry of a capacitor winding have and how can it be mapped within FE simulation models?

III) How can suitable simulation models be built at the capacitor level and what simplifications can be made to optimize the efficiency of these models?

IV) Are polarization effects in capacitor windings relevant and what effect do they have on acoustic excitation?

V) To what extent do capacitor windings have similar properties as electrets and how can this be explained within the dielectric?

Chapter 3

Electromechanical excitation model for metallized film capacitors

The electrostrictive model for a metallized film capacitor winding based on BOPP has been initially published and verified in [11].

In order to calculate strains due to electrostrictive forces in film capacitors, the basic model is derived from a plate capacitor geometry. Then, the excitation model is transferred to winding geometries using homogenized material properties. In order to take the geometric properties of the windings into account, the excitation model is then converted into a FE model. Therefore, two different simulation approaches are presented in this chapter.

3.1 Electrostrictive excitation model for a plate capacitor

In order to derive an excitation model, a plate capacitor analogous to Fig. 3.1 is exposed to a homogeneous electric field. This results in a strain in the field direction $\epsilon_{\parallel}$ as well as a strain in the perpendicular direction $\epsilon_{\perp}$.

Due to the previously introduced electrostrictive couplings, the resulting strain $\epsilon_{\parallel}$ in electric field direction cannot be directly calculated with the Poisson ratio ν and the strain $\epsilon_{\perp}$ perpendicular to the electric field, which means:

$$\nu\epsilon_{\perp} \neq -\epsilon_{\parallel}. \tag{3.1}$$

The relationship between transverse and longitudinal strain must be extended to include the electromechanical couplings, which will be addressed in the following.

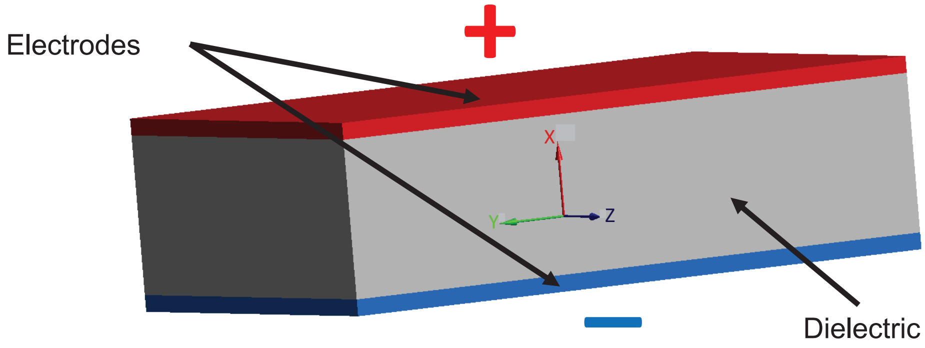

Figure 3.1: Model of a plate capacitor exposed to a homogeneous electric field.

3.1.1 Electrostrictive deformation

The deformation based on an electrical field can be calculated based on the formulas introduced in section 2.4, respectively eq. (2.30).
In order to calculate the deformation, the electrostrictive coefficients a_1 and a_2 are required. As presented in section 2.4.3, these coefficients can be calculated with an analytical model presented by Shkel and Klingenberg [103]. The resulting electrostrictive parameters are based on the dielectric constants for PP $\varepsilon_{PP} = 2.2$ and the dielectric constant of the included cavities $\varepsilon_c = 1$ in the material and are shown in Tab. 3.1.

Electrostrictive coefficient	Value
a_1	0.58
a_2	1.49

Table 3.1: Comparison of electrostrictive parameters from literature. The values are obtained by the presented analytical model from Shkel and Klingenberg [103] and also have been applied by Thakur and Agrawal [115] for PP.

The further calculations and simulations presented in this chapter are based on these electrostrictive parameters, which were also used by Thakur and Agrawal [115]. The resulting deformations are then validated by a comparison to measurements, presented in section 3.3.
With the electrostrictive parameters, the deformation of a plate capacitor can be calculated. It must be taken into account that eq. (2.30) only provides static deformations and dynamic effects such as resonances are not considered. This is possible by harmonic analysis with the help of FE simulation tools. The corresponding strain coefficients $\epsilon_{x,y,z}$ used for further calculations are summarized in Tab. 3.2

Orthotropic parameter	Value
Strain coefficient ϵ_x	-1,310E-09
Strain coefficient ϵ_y	0,887E-09
Strain coefficient ϵ_z	0,887E-09

Table 3.2: Electrostrictive strain coefficients of polypropylene. The material parameters are orthotropic.

Furthermore, the deformation of the capacitor depends on the dielectric used and the geometric boundary conditions. To explain the effects, the analytical model based on a plate capacitor will be described in more detail.

3.1.2 Capacitor voltage

For a plate capacitor, the homogeneous electrical field depends on the applied voltage and the plate distance. The regarded excitation effects have a quadratic dependency on the voltage of the DC-link capacitor U_{cap}, wich can be written as

$$U_{\mathrm{cap}}(t) = U_{\mathrm{DC}} + U_{\mathrm{AC}}(t). \tag{3.2}$$

The capacitor force F_{cap} is then directly proportional to the square of the voltage U_{cap}. As a result, the constant c can be used, i.e.

$$F_{\mathrm{cap}}(t) = c\,(U_{\mathrm{DC}}^2 + 2U_{\mathrm{DC}}U_{\mathrm{AC}}(t) + U_{\mathrm{AC}}(t)^2). \tag{3.3}$$

The AC voltage U_{AC} with the amplitude $U_{\max}$ can be written as

$$U_{\mathrm{AC}}(t) = U_{\max}\sin(\omega t). \tag{3.4}$$

Combining eq. (3.3) and eq. (3.4) and applying the sine addition theorem

$$\sin^2(x) = \frac{1}{2}(1 - \cos(2x)), \tag{3.5}$$

the relation between capacitor force and applied voltage can be written as

$$\begin{aligned} F_{\mathrm{cap}} &= c\,(U_{cap})^2 \\ &= c\,(U_{\mathrm{DC}}^2 + \frac{U_{\max}^2}{2} + 2U_{\mathrm{DC}}U_{\max}\sin(\omega t) - \frac{U_{\max}^2}{2}\cos(2\omega t)). \end{aligned} \tag{3.6}$$

This force consists of three parts triggered by DC-voltage, AC-voltage or a coupling of both:

- Pretension $\propto U_{\mathrm{DC}}^2 + \frac{U_{\max}^2}{2}$;
- Fundamental oscillation $\propto 2U_{\mathrm{DC}}U_{\max}\sin(\omega t)$;
- Harmonic oscillation $\propto \frac{U_{\max}^2}{2}\cos(2\omega t)$.

The pretension is not time-dependent and can be treated as a constant. As a result, this excitation component does not lead to acoustic sound radiation. However, since it depends quadratically on the DC voltage, its value in capacitors of electric vehicles is relatively large. This is due to the fact that the DC voltage or battery voltage is usually much higher than the AC ripple caused by the conversion.

When it comes to electric vehicles, the fundamental oscillation is the most relevant acoustic excitation. It is present at the same frequency as the external excitation and is specifically filtered out during further measurements via a bandpass filter.

The first harmonic oscillation is present at twice the frequency of the fundamental oscillation. If the excitation frequency of the fundamental is usually still within the audible range for humans, the first harmonic can often be disregarded for this reason alone since it moves out of the audible spectrum. In electric vehicles, switching frequencies between 8 and 10 kHz are common, which means that the first harmonic is already in the range of 16 to 20 kHz. In addition, it is usually less prominent due to the smaller magnitude of the AC voltage.

3.1.3 Analytical calculation of the acoustic excitation in BOPP film capacitors

In this section, the excitation of a capacitor stack is calculated based on the sensor model from Thakur et al. [114, 115], presented in chapter 2. The influence of electromechanical couplings will be analysed using the example of a typical capacitor geometry used for an electric vehicle. If the dielectric film is exposed to an electric field, it contracts according to Fig. 3.2 in the direction of the field lines.

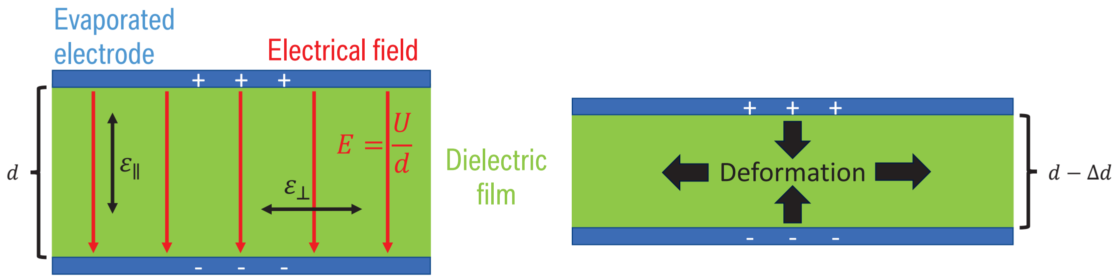

Figure 3.2: Schematic representation of a film layer deformation in direction of and transverse to the applied electric field.

- Film thickness d: 2.5 µm
- Stacked layers: 1000
- Poission ratio ν: 0.42
- Youngs modulus Y: 1400 MPa

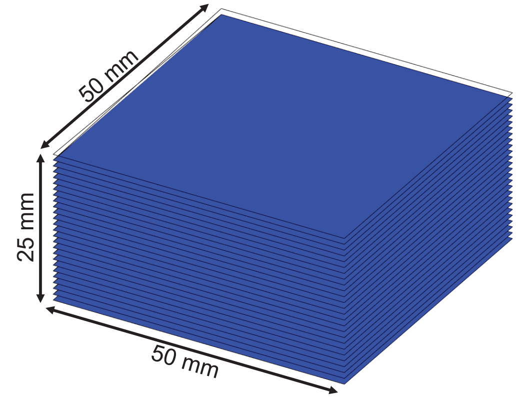

Figure 3.3: Capacitor film stack consisting of 1000 layers.

For an exemplary capacitor stack (e.g. in Fig. 3.3), the deformations can either be calculated based on the previously presented electrostrictive model or by applying the Coulomb model:

Coulomb model

The force between the plates of the capacitor is given by:

$$F = \frac{1}{2}\varepsilon_0\varepsilon_r A\left(\frac{U}{d}\right)^2.$$

The deformation Δd then results from

$$\Delta d = \frac{Fd}{AY}.$$

Together with the force F, the deformation is obtained by

$$\Delta d = \frac{\varepsilon_0\varepsilon_r U^2}{2Yd}.$$

Using the Poisson ratio, the strain $\epsilon_\perp$ transverse to the electric field can be calculated with the expression

$$\nu\epsilon_\perp = -\epsilon_\parallel.$$

Electrostrictive model

If the electromechanical couplings are taken into account, the deformation of the capacitor can be expressed using the electrostrictive parameters a_1 and a_2, i.e.

$$\Delta d = \frac{\varepsilon_0\varepsilon_r U^2}{2Yd}\left((1+2\nu) - \frac{a_1 + (1-2\nu)a_2}{\varepsilon_r}\right).$$

For the direction transverse to the electric field, the strain can be calculated according to

$$\epsilon_\perp = \frac{1}{2Y}\varepsilon_0\varepsilon_r\mathbf{E}^2\left(1 - \frac{\nu a_1 - (1-2\nu)a_2}{\varepsilon_r}\right).$$

The strain relation between the two directions can no longer be expressed via the Poission ratio, meaning

$$\nu\epsilon_\perp \neq -\epsilon_\parallel.$$

In order to get a practical reference for an automotive application, a capacitor winding with a width of 25 mm is considered. This winding can be represented as a capacitor stack, as already presented in Fig. 3.3. If a ripple voltage is applied to the capacitor element with a DC component of 400 V and an AC component of 5 V, the deformation parts corresponding to eq. (3.6) can be calculated. The resulting deformations are shown for the pretension, the fundamental and the first harmonic in Fig. 3.4, in each case with and without consideration of electrostriction.

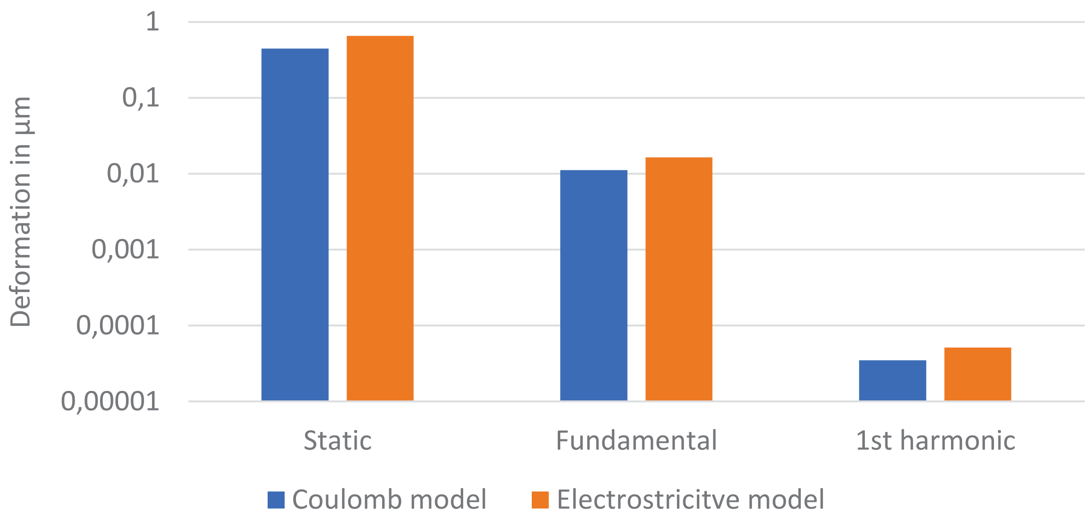

Figure 3.4: Analytical calculation of the deformation in the direction of the electric field at a realistic operating point for automotive applications. The influence of resonances is not taken into account here.

It can be concluded that the the deformations of the capacitor in automotive applications are strongly driven by the DC voltage. The consideration of electromechanical couplings increases the excitation amplitude (by a factor of approx. 1.47 for the example capacitor) and is therefore taken into account in the further course of the work.

The static pretension leads to the largest amplitudes in comparison due to its quadratic dependence on the DC voltage. However, as this deformation is not time-dependent, it does not play a significant role for acoustic phenomena in DC-link capacitors.

Acoustic interference therefore emanates from the fundamental oscillation and its harmonics. The calculation example shows that the fundamental oscillation is much more relevant than its 1st harmonic due to the DC dependency, considering the dominance of the battery voltage. For this reason, it is not necessary to consider further harmonics, as their excitation amplitude continues to decrease.

Any resonance behaviour was neglected in the above calculation, which means that enlargement and damping effects are not taken into account. However, the consideration of resonance effects is essential for a comparison between the analytical calculation with simulations and measurements. A simple way to consider this effect is to use the enlargement function A_ω

$$A_\omega = \frac{A_{static}}{\sqrt{(1-\eta^2)^2 + (2D\eta)^2}} \quad \text{with} \tag{3.7}$$

$$\eta = \frac{\omega}{\omega_{res}}. \tag{3.8}$$

This allows to predict the amplitude ratio over the frequency below the first resonance frequency. Here, the influence of possible resonances is expressed by applying the frequency ratio η and Lehr's damping ratio D. If, for example, a capacitor winding with a resonant frequency of 5500 Hz is considered, the peak in the resonance depends on the assumed damping ratio. This behaviour is shown for different damping values in Fig. 3.5.

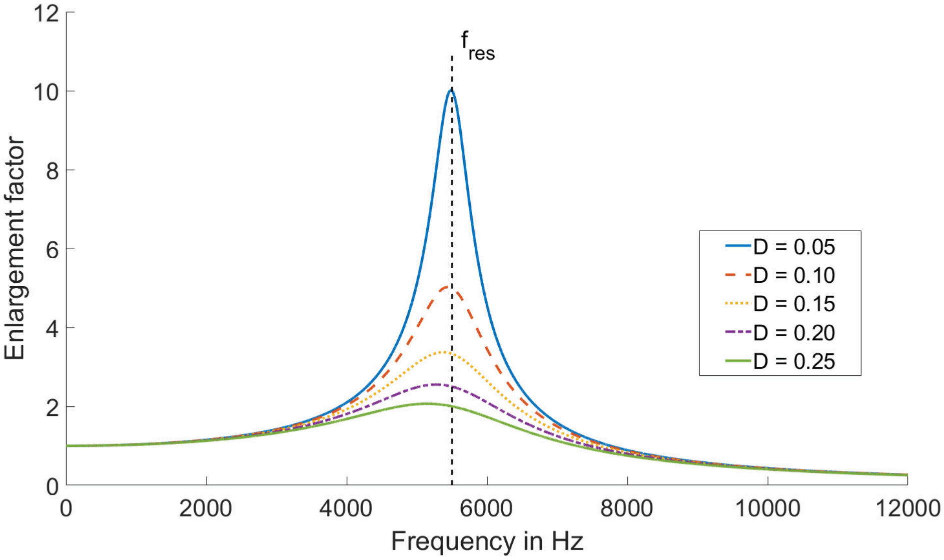

Figure 3.5: Enlargement function of an oscillating system with a resonant frequency of $f_{\text{res}} =$ 5500 Hz and different values for the Lehr's damping factor D.

Since the analytically calculated deformation neglects the resonance effects, only the static amplitude A_{static} is obtained. When comparing with measurements and harmonic simulations, the enlargement function must therefore be taken into account. This is only possible for the first resonance. For the examined windings, a damping ratio of D=0.14 was determined in validation measurements within this work, therefore reference is made to section 3.3.

3.2 FE modelling of film capacitor windings

The simulation approach used in this work has been published in Herrnberger et al. [41] and all simulations have been performed with ANSYS Workbench 2020R1. In order to apply the excitation calculated from the analytical model, two different simulation approaches are presented. These excitation models can be subdivided into:

- Temperature-based excitation model;
- Pressure-based excitation model.

Both approaches are verified with vibrometer measurements and lead to a good agreement based on the modal matching and the excitation amplitudes determined in the harmonic analysis. For the models investigated, a film thickness of 2.5 µm was assumed. Since film capacitor windings are made of more than 1000 layers, simulating every single layer is out of scope as it would lead to an unmanageable number of degrees of freedom. As a result, the winding has to be modelled with homogenized material parameters. A typical winding geometry is mainly consisting of metallized BOPP as well as of alloy for the electrical contacting, as it is depicted in Fig. 3.6.

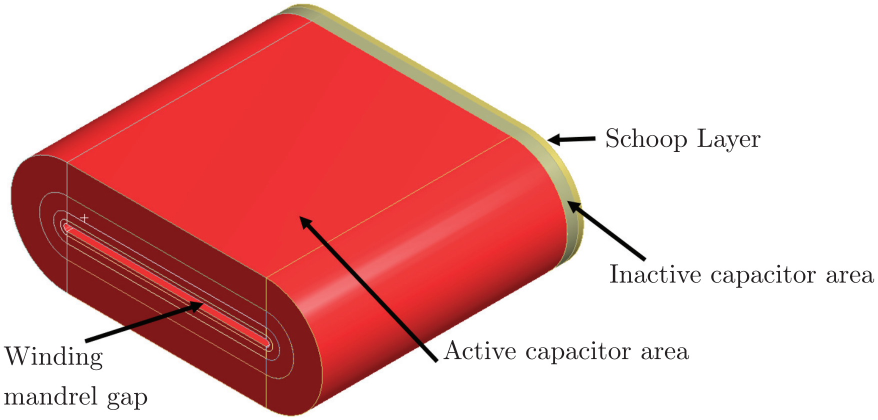

Figure 3.6: Structure of the capacitor winding in FE simulation environment. The capacitor is subdivided into an active and an inactive part since the two BOPP films are overlapping with a free margin in order to avoid creepage between the two potentials.

For the simulation, the metallization of the film is neglected, since the winding consists mainly of BOPP. However, the Schoop layers must be taken into account, since they increase the stiffness at the end faces decisively. The corresponding mechanical material properties for the materials used for a winding model are summarized in Tab. 3.3.

Material	Density [kg/m^3]	Young's modulus [GPa]	Poisson ratio [-]
Metallized BOPP	978	1.4	0.418
Schoop layer	7175	108	0.36

Table 3.3: Material properties used for the capacitor winding simulation models.

The winding deformation due to an electrical excitation can be represented either by thermal loads and corresponding expansion coefficients or by equivalent pressures. The use of equivalent pressures allows an accelerated calculation in ANSYS Workbench 2020R1, since modal superposition (MSUP) can be used. The disadvantage of using the replacement pressure model presented in [41] is that additional work is required to calibrate the individual pressure components. All simulations carried out in this thesis are based on implicit solvers.

Both the temperature-based and the pressure-based approach are presented here. The harmonic analysis is calculated based on full matrices (FULL) as well as based on a model reduction approach. Therefore, modal superposition (MSUP) is applied. Both methods can be summarized as follows:

FULL

With the full calculation, all results (stresses, displacements, etc.) are calculated in one step using matrix inversion. Since the mass matrix does not have to be approximated compared to the other methods, it is the most accurate method for a given mesh. The calculation offers further advantages, such as the setting of frequency-dependent material data based on the frequency-dependent description. This means that any damping of partial or complete structures is possible. Furthermore, due to the general calculation, there are no restrictions with regard to loads that can be imposed. Compared to the modal superposition, the main disadvantage of this method is the significantly higher numerical effort.

MSUP

In the first step of modal superposition, the eigenvectors are calculated using the Block-Lanczos algorithm for a pre-defined frequency range. The modal superposition then uses factorised eigenmodes of vibration to calculate the response of the structure. For the modal analysis, a frequency range should be selected that is at least 1.5 times larger than the range to be analysed in the harmonic analysis. This ensures that all natural frequencies that can contribute to the harmonic response are calculated. The main advantage of the MSUP variant is the significantly lower computational effort and the resulting reduction in time compared to the simulation methods mentioned above. A significant disadvantage is that it is not possible to take frequency-dependent material damping into account.

In addition to model reduction, structural meshing of the windings is another way of increasing numerical efficiency. For this reason, the simulations carried out in the thesis were all performed with structured meshed windings. To ensure the contact conditions between the Schoop layer and the winding body, the shared topology setting was used in ANSYS Workbench, as a result no further contact conditions are necessary. This ensures that two bodies share their boundary nodes. The meshed winding with hexahedral elements is shown in Fig. 3.7. Elements of type Solid186 were used, which are based on quadratic polynomials.

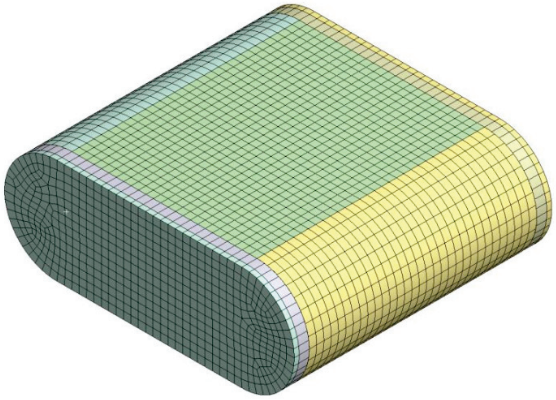

Figure 3.7: Capacitor winding with structured mesh consisting of 92k nodes. The elements have an edge length of max. 1.5 mm.

In order to minimize the influence of the boundary conditions for the subsequent comparison with experimental measurements, it is advantageous to avoid constraining any degrees of freedom. This can be achieved in the ANSYS Workbench environment. However, when performing a modal analysis, one must ensure that the first six modes determined correspond to the rigid body modes.

3.2.1 Temperature-based excitation model

The volumetric strain can be applied on the capacitor winding by using a thermal equivalent model. For this reason, orthotropic thermal expansion coefficients analogous to Tab. 3.2 are defined in a way that 1 V^2 is proportional to 1 K. These coefficients are defined for the direction of the electric field as well as in perpendicular direction. The strain in the transversal directions is neglected since it is much smaller compared to the strain in principle directions.

Since it is not common to use temperature variations in harmonic analysis up to 16 kHz, this option is not provided by default within ANSYS Workbench. In order to apply the equivalent temperatures to the capacitor winding geometries, ANSYS parametric design language (APDL) commands must be used. If a single capacitor winding is exposed to a voltage of 100 V^2, the corresponding command is:

```
thexpand, on
bf,all,temp,100
```

If this excitation is transferred to more complex geometries, the corresponding nodes belonging to the winding must be selected via APDL commands beforehand. A disadvantage of thermal analysis is that modal superposition cannot be used, which leads to comparatively higher numerical costs. This may not be a problem for a single winding, but it leads to difficulties when applied to larger structures. As a result, the thermal excitation approach can therefore only be recommended up to a maximum of 100000 DoFs.

3.2.2 Pressure-based excitation model

The pressure-based simulation is realized with different pressure components. If these pressure components are used analogously to [41], an optimization is necessary to get a good agreement between the thermal reference model and the pressure based model. This step can also be omitted if the pressure components are applied in layers. This allows to approximate a plate capacitor based on the winding geometry.

Since the FULL calculation leads to increased numerical costs, various pressure components can be applied to the winding, thus achieving a deformation equivalent to the thermal model. Within this work, the deformation is applied by six different pressure components. These pressure components are chosen in a way that the deformation of the temperature model is almost matched identically. This requires some recursions of optimization. Therefore, the modal assurance criterion (MAC) is used as the target variable. This value represents a way to compare the modes of two mechanical systems by calculating the MAC value based on the modal deformation vectors φ_1 and φ_1, i.e.

$$\mathrm{MAC}(\varphi_1, \varphi_2) = \frac{|\varphi_1^T \varphi_2|^2}{(\varphi_1^T \varphi_2)(\varphi_1^T \varphi_2)}. \tag{3.9}$$

The MAC value can be between zero and one, where zero is no match and one is a perfect match between two mode shapes of two mechanical systems. Values greater than 0.9 indicate a consistent match, while smaller values indicate a low similarity between two mode shapes [86]. The different pressure components used for this approach on capacitor winding level are shown in Fig. 3.8 [41].

The temperature-based excitation can also be modelled by these substitute pressures. In order to achieve a good correlation between temperature model and pressure model, the shown pressure components were selected. They can be divided in outer pressures (red) and inner pressures (green). As a next step, the amplitudes of the pressure components are optimized to achieve a good MAC correlation between the thermo-mechanical substitute model and the pressure-based model. The optimization steps used are shown in Fig. 3.9 where the individual steps increase the accuracy. After MAC optimization and differentiation of pressures depending on frequency, both models provide

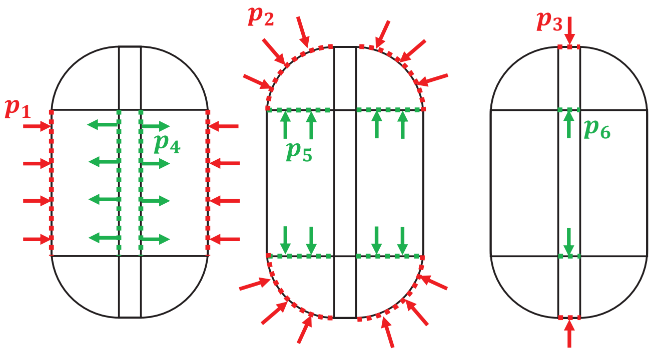

Figure 3.8: Substitute pressure components. Red: Pressure components on outer surface. Green: Inner pressure components for compensation.

almost identical results.

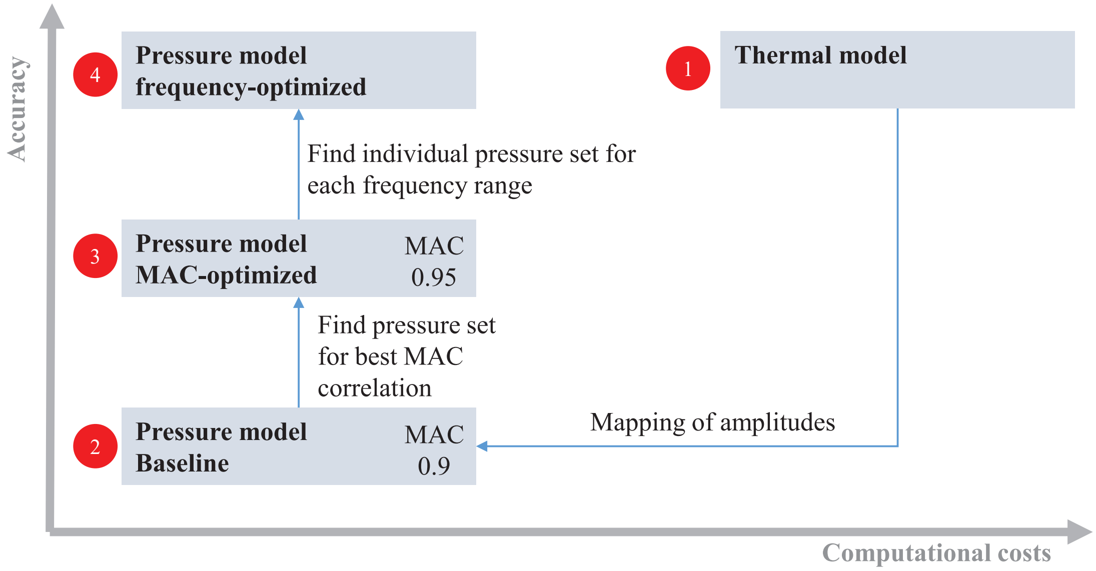

Figure 3.9: Process of pressure calibration introduced in [41].

In the baseline model, the amplitudes of the pressure components are evenly distributed and the excitation amplitude of a reference point is adjusted to map the substitute variables temperature and pressure. As a next step, the pressure distribution is optimized for a good MAC correlation of the static deformation shapes. At last, the pressure distribution is adjusted for different frequency ranges. In order to evaluate the agreement of the thermal model and the pressure-based model, the corresponding ERP to the optimization steps are compared in Fig. 3.10.

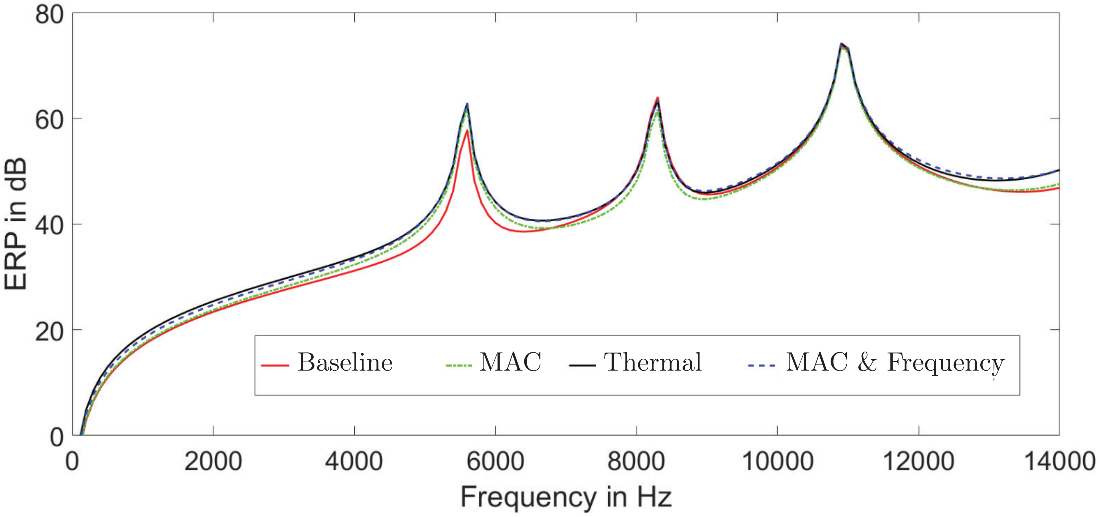

Figure 3.10: Consistency of the different modeling steps. After the optimization steps, the temperature-based model and the pressure-based model are almost identical.

If the pressure components are in a certain relation, the ERP of the pressure model shows a good agreement with the initial thermal model. Tab. 3.4 describes the pressure distribution of the different modelling stages for the baseline model, the MAC optimized model and the MAC optimized model separated in four different frequency ranges.

	Frequency [kHz]	Input parameters [Pa]					
		p1	p2	p3	p4	p5	p6
Baseline	0-14	100	100	100	100	100	100
Optimized MAC	0-14	103.68	83.05	79.52	100.97	98.42	88.23
Optimized MAC FREQ	0 - 5.6	116.06	92.97	89.02	113.03	110.17	98.76
	5.6 - 8.3	127.70	102.29	97.94	124.36	121.22	108.67
	8.3 - 10.9	112.51	90.12	86.29	109.57	106.80	95.74
	10.9 - 14	154.42	123.69	118.44	150.38	146.58	131.40

Table 3.4: Optimized pressure distribution to match the temperature-based excitation model [41].

There, the baseline model has been normalized to 100 Pa, since the amplitude has not yet been taken into account and only the modal behaviour is regarded. A further simplification of the pressure model with six different components is a multilayer model where only two pressure components are required. The winding is divided in a way that the individual segments approximate plate capacitors. In order to achieve this, small segments are used inside the winding, which increase in size towards the outside. An exemplary segmentation is shown for a winding geometry in Fig. 3.11.

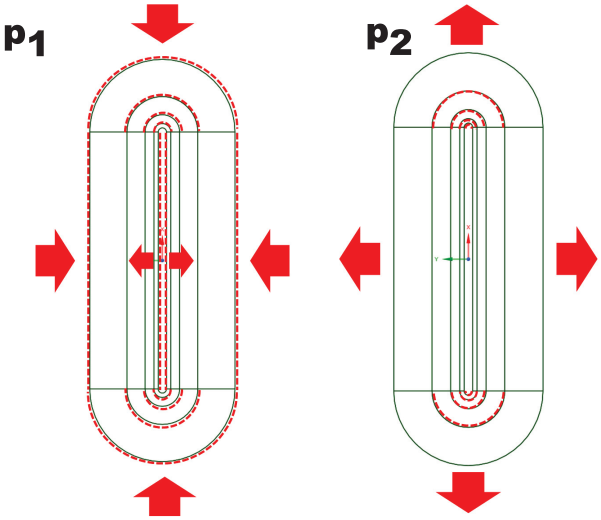

Figure 3.11: Excitation with inner and outer pressure components based on four layers.

The growth of each layer radius is given by the growth constant K which is composed of the largest layer radius R_n, the smallest layer radius R_1 and the number of layers n as follows:

$$K = \sqrt[n]{\frac{R_n}{R_1}} \tag{3.10}$$

The increasing radii ensure that the inner and outer surfaces of the round segments always have the same ratio. The more layers are used, the closer this area ratio approaches one, which would correspond to an ideal plate capacitor geometry. For the fast generation of the winding geometries, a parameterized ANSYS Workbench script was created to generate different winding geometries with an arbitrary number of layers.

Since this distribution of pressures is much closer to the real excitation, the simulation quality of the thermal reference model can be achieved in the multi-layer approach even without optimization loops. It must be mentioned that the number of layers required depends on the geometrical conditions of the capacitor. In general, it can be stated that flat windings (fewer windings and higher strip width of the film) require a reduced number of layers than thicker windings, since the influence of the round segments increases in the latter. This relationship is illustrated in Fig. 3.12.

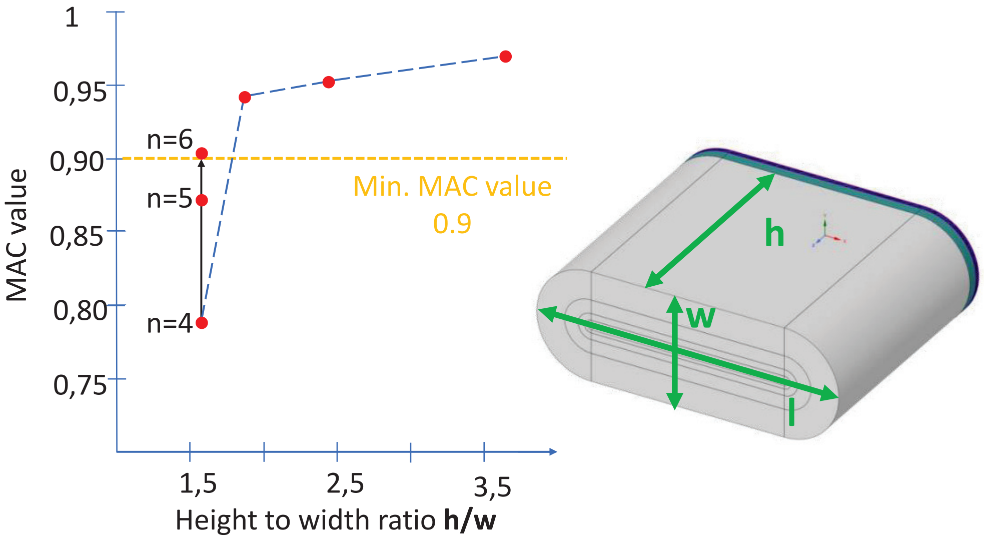

Figure 3.12: MAC correlation of different winding geometries. For a low height to width ratio, the number of layers had to be increased from n=4 to n=6 to achieve a MAC value of 0.9.

For thicker windings, a good MAC correlation with the thermal reference model is more difficult to achieve than for thinner windings, where the straight segments predominate. As a result, for the winding with the lowest height to width ratio, the number of layers n had to be increased from four to six in order to achieve a good MAC correlation. For the other geometries, the required MAC value of 0.9 can already be achieved with four layers.

As already mentioned, the major advantage of the pressure-based excitation approach is the reduced computing time. The reason for this is that the previously described modal superposition can be used here. This consists of a modal analysis and a subsequent harmonic analysis, whereby the deformations of the linear FE model are described by superposition of its eigenmodes. For high-quality results, it must be ensured that the modal analysis is carried out for frequencies that are 1.5 times the frequency range of the harmonic analysis. The calculation times of the winding model for both approaches are compared in Tab. 3.5.

Simulation approach	Harmonic response	Modal analysis
Thermal	557 s	-
Pressure-based	23 s	30 s

Table 3.5: Comparison of computing times in seconds: mode-superposition vs. direct solution of the simultaneous equations of motion. The model of the winding was solved for 140 frequency points [41].

The modal superposition therefore enables computing time savings of approx. 90 percent. The use of the pressure-based approach is therefore highly recommended, especially for large models based on capacitor assemblies or power electronic units.
The calibration workflow for the pressure-based approach always compared the MAC values of the static deformation fields due to an external force excitation. The MAC values of the different modes usually fit very well with the temperature model, independent of the adequacy of the pressure model. As a result, the static consideration provides the worst case. However, MAC matching between the two simulation approaches provides good agreement across the frequency range, as depicted in Fig. 3.13.

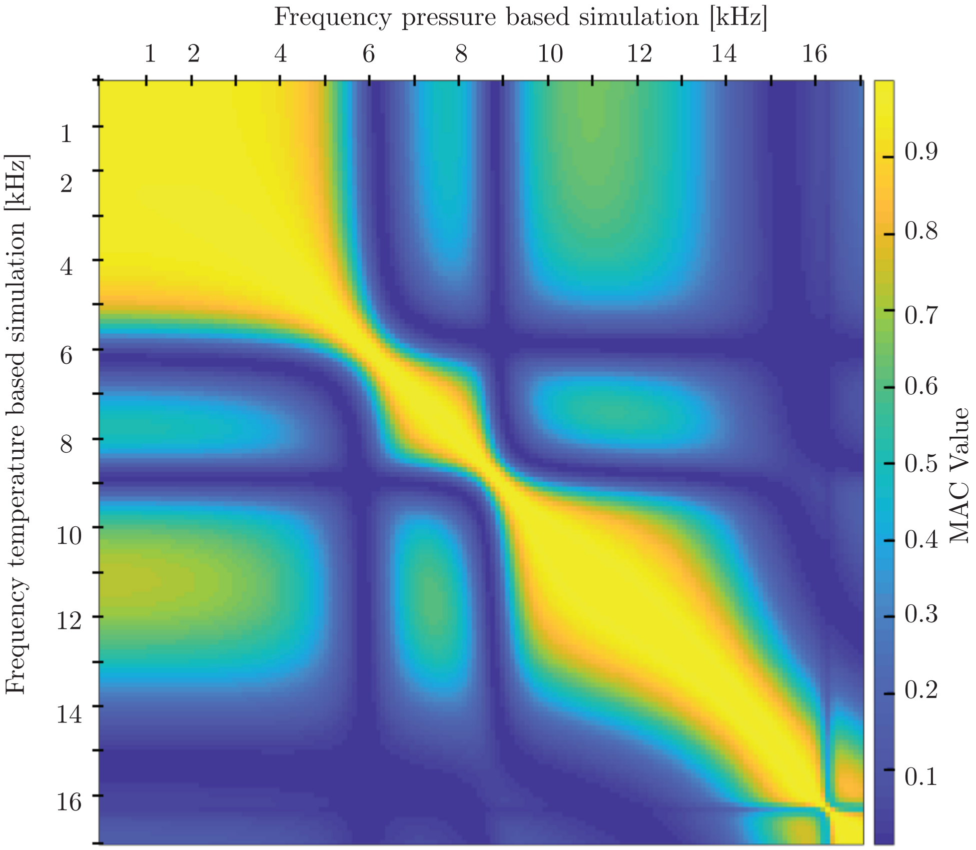

Figure 3.13: MAC comparison of temperature-based and pressure-based winding models.

It can be seen that the mode shapes on the diagonal are always above the required MAC value of 0.9, which means that both excitation models achieve a very similar deformation over the entire frequency range.

3.2.3 Simulation results for film capacitor windings

With the help of the presented models, any arbitrary winding geometry can now be simulated. In the acoustically relevant range up to approx. 16 kHz, four different modes of the bobbin will occur. In particular, the pump mode and the bending mode are most relevant, since they excite the structure in later measurements even in assembled capacitors. The two modes are shown in Fig. 3.14.

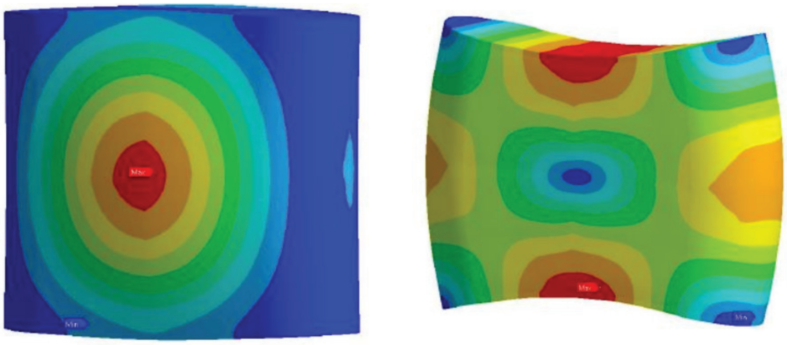

Pumping mode

Bending mode

Figure 3.14: Typical modes of film capacitor windings in the audible frequency range.

In the higher frequency range, the double pump mode as well as a combination of pump and bending mode occur, analogous to Fig. 3.15. However, these are only in the audible range for thinner windings and can theoretically be excluded by a suitable choice of winding dimensions for acoustic interference.

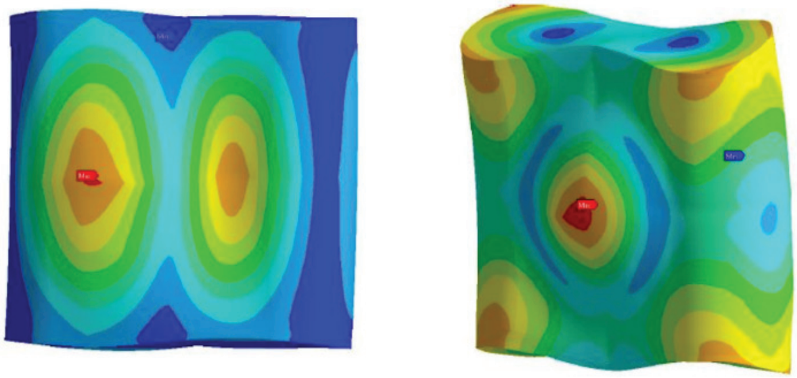

Double pumping mode

Pumping and bending mode

Figure 3.15: Typical modes of film capacitor windings in the audible frequency range.

For a given winding geometry, the system can be detuned with the aid of minimal adjustments. This allows to avoid the unfavorable overlapping of resonance and excitation frequency. It is obvious that the resonance frequency of a winding should not coincide with the PMW carrier frequency. Shifting the frequencies is possible, for example, by adjusting the thickness of the Schoop layer. The influences on the ERP of different Schoop layer thicknesses are shown in Fig. 3.16.

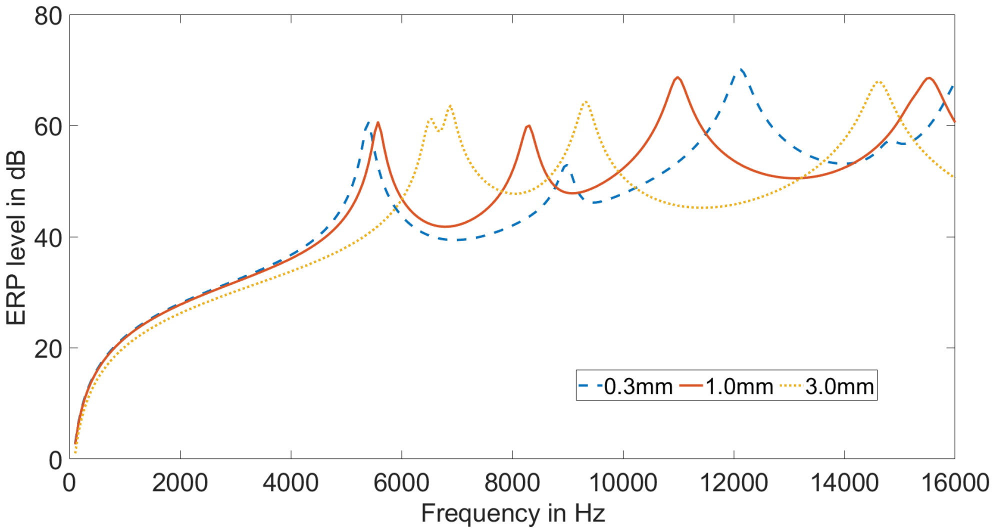

Figure 3.16: Acoustic detuning of the capacitor windings by variation of the Schoop layer thickness.

A thicker Schoop layer stiffens the capacitor winding, which tends to shift the modes to the higher frequency range. This is visible, for example, in the bending mode across the Schoop surface. In summary, the system winding can be detuned by the following measures:

- Changing the number of turns;
- Dimension of the mandrel gap;
- Schoop layer thickness;
- Film cutting width.

In the examined winding geometries, a further trend can be seen which influences the frequency of the pump mode. The pressing of the initially round winding into an elongated shape is crucial for the first natural frequency. This becomes clear when the ratio of winding length and winding width is taken into account (see Fig. 3.12). The four examined winding geometries are shown in Tab. 3.6.

Length l [mm]	Width w [mm]	Frequency of pumping mode [Hz]
75	28	5580
65	34	7120
65	40	8850
54	52	10940

Table 3.6: Influence of the length-to-width ratio on the frequency of the main resonance of the capacitor winding. Thinner, more compressed bobbins exhibit lower resonant frequencies than rounder shapes with less compression. The winding height was kept constant at h=62 mm.

To summarize, more compressed windings lead to a lower frequency of the pumping mode, which is important for acoustic excitation within the capacitor assembly. If this frequency needs to be increased, round winding geometries with small compression rates are recommended. However, this is not always useful for an optimized package, since larger areas remain free between the windings.

3.3 Validation of the capacitor excitation model

In this section, the simulation models are compared to vibrometer measurements. It can be shown that the excitation modes of the windings can be predicted well with the presented approaches. In addition, the simulated excitation amplitude is compared with the measured excitation amplitude of the winding. To achieve a precise match between measurement and simulation, polarization effects in the winding must be taken into account. These effects could be demonstrated in the experiments and will be introduced in the following section.

3.3.1 Measurement of the electromechanical excitation of capacitor windings

The electromechanical excitation of capacitor windings is measured with a laser vibrometer. Therefore it is possible, to measure dynamic deformations without contact and thus without influencing the measured object by changing its mass or stiffness. The corresponding measurement setup is shown in Fig. 3.17.

The measuring principle is based (in standard measuring mode) on the monitoring of the frequency shift caused by the Doppler effect. As a result, the laser signal reflected from the measured object is compared to a reference signal via interference. The frequency shift f_d depends on the surface velocity v and the laser wave length λ, i.e.

$$f_d = 2\frac{v}{\lambda}. \tag{3.11}$$

In the case of the helium neon laser, which is used almost exclusively for vibrometers, this corresponds to a wavelength of 316 nm. In order to measure the electromechanical frequency response

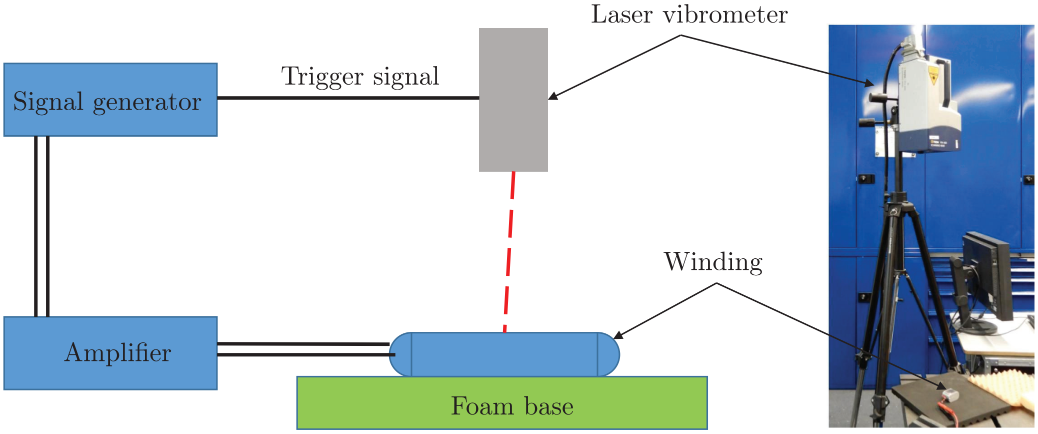

Figure 3.17: Measurement setup for the validation of the electromechanical excitation model based on BOPP film capacitor windings.

function of a capacitor, a voltage signal is applied to the winding and the resulting surface velocity is measured. The capacitor winding is placed on a foam base to provide free boundary conditions. The excitation is done by a ripple voltage, i.e. a DC voltage which is superimposed with an AC Voltage. The generated signal is also used as a trigger signal for the fast Fourier transform (FFT). For this reason, the voltage applied to the bobbin is used a a phase reference.

3.3.2 Introduction of the compensation voltage

At first glance, the measured amplitudes show inconsistencies and are not symmetrical to the applied DC voltage. This is evident from the fact that relatively high amplitudes were measured for the fundamental oscillation even in the absence of an external DC voltage. According to the derived capacitor voltage in sec. 3.1.2, the first fundamental oscillation would not be present at a DC voltage of zero. In addition to that, the measured amplitudes were significantly higher at a DC voltage of 40 V than at a DC voltage of -40 V. The excitation curves for different voltage levels are shown in Fig. 3.18. The evaluated point is located in the centre of the winding, where the greatest deflection is to be expected due to the pumping mode.

As already introduced in chapter 2, this behaviour can be traced back to polarization effects. The exact analysis of the polarization effects will be part of chapter 5. The behaviour of the winding is reminiscent of the adaptation of electrostatic transducers to an externally applied voltage measurement, comparable to a capacitance-voltage characterisation. In contrast to the measurements known in the literature, the acoustic response of the bobbin is analysed via a DC voltage in this work. As this leads to a deformation, a C-V measurement analogous to electrostatic transducers

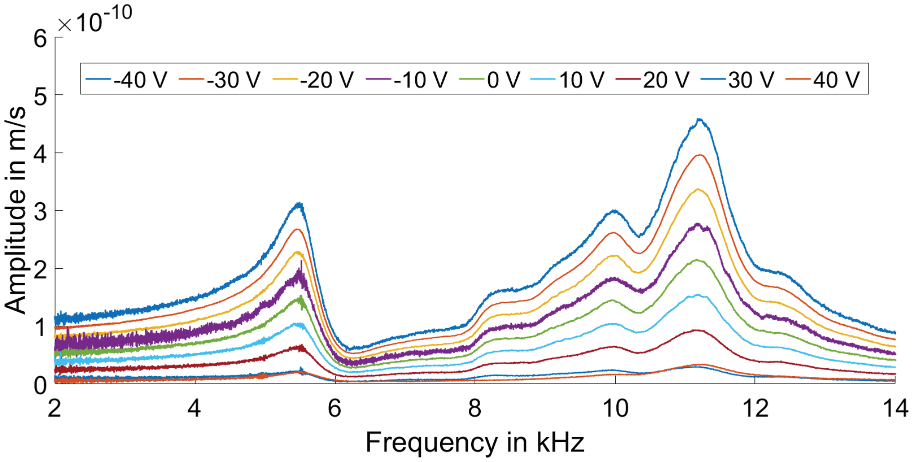

Figure 3.18: Measurement of amplitudes at different DC voltage levels.

could be carried out as an alternative.

In order to predict the excitation amplitude of the windings correctly, the excitation model from eq. (3.6) has to be adapted. The amplitude $A_{\text{Fundamental}}$ of the fundamental oscillation additionally depends on a compensative voltage U_{comp} from polarization inside the dielectric, i.e.

$$A_{\text{Fundamental}} \propto 2(U_{\text{DC}} + U_{\text{comp}})U_{\max}\sin(\omega t). \tag{3.12}$$

This compensation voltage has an impact on the electromechanical excitation amplitudes measured for the capacitor bobbins. This means that the amplitude depends on the polarity of the external DC-voltage. If the first resonance of the measurements from Fig. 3.18 is evaluated, the polarization of the bobbin can be calculated according to Fig. 3.19. In simple terms, this means that a BOPP film capacitor can be louder or quieter by changing the polarity at an otherwise identical voltage point.

The existence of the compensation voltage of BOPP film capacitor windings has been described in [11]. Although the polarization effects have not been considered for the acoustic excitation of capacitors, the relevant effects have been studied in literature. One of the first publications to observe the influence on polarized dielectrics on the acoustic excitation has been presented by Kuhl et al. in 1954 [65]. This publication also mentions a compensating voltage, but the charging mechanism was not explained in detail. The effect was later used for acoustic applications, in particular for the development of the electret microphone by Gerhard Sessler [99]. This design is still a widely used type of microphone today, as it allows the development of low-cost and compact microphones.

As described in chapter 2, the manufacturing process of DC-link capacitors leads to a preferred

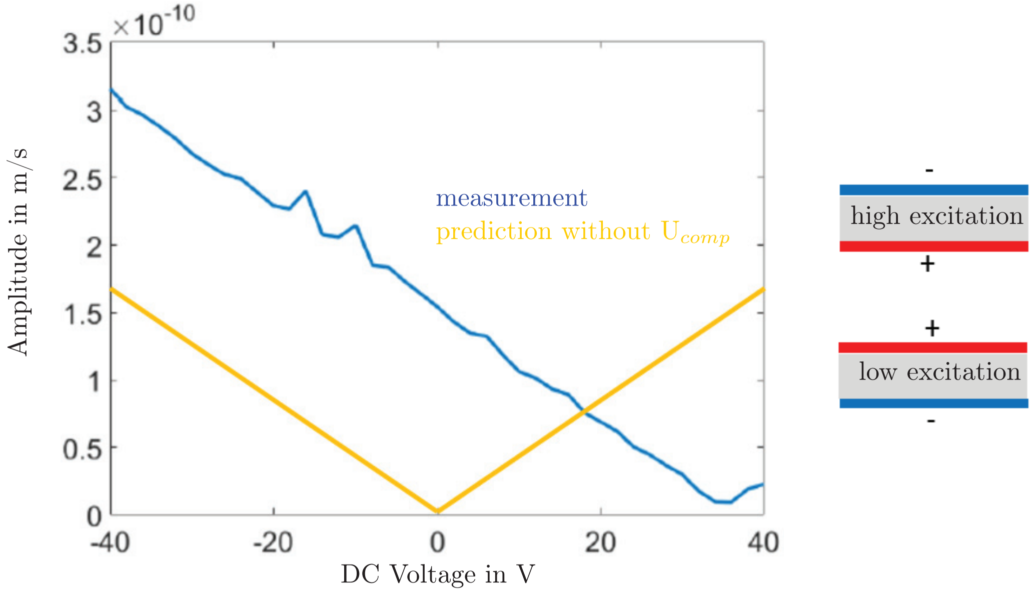

Figure 3.19: Evaluation of the first resonance via the applied DC voltage. Pre-polarization makes it possible to excite the same PP capacitor to different degrees by changing the polarity [11].

direction with regard to the externally applied DC voltage. In the following, the compensation voltage U_{comp} describes the necessary externally applied voltage to compensate for this preferred direction. As a result, the square capacitor voltage $(U_{\mathrm{cap}})^2$ from eq. (3.12) can be written according to

$$(U_{\mathrm{cap}})^2 = (U_{\mathrm{DC}} + U_{\mathrm{comp}})^2 + \frac{U_{\mathrm{max}}^2}{2} + 2(U_{\mathrm{DC}} + U_{\mathrm{comp}})U_{\mathrm{max}}\sin(\omega t) - \frac{U_{\mathrm{max}}^2}{2}\cos(2\omega t). \tag{3.13}$$

Accordingly, the compensation voltage will only affect the fundamental oscillation and the pretension. The compensation voltage can either have the same or the opposite polarity as the external applied DC voltage. This is affecting the fundamental oscillation and has the potential to either improve or to aggravate the acoustic properties of DC-link capacitors.

3.3.3 Comparison of measurement and simulation model

The excitation amplitude measured with the setup in Fig. 3.17 can be calculated either analytically or with the help of the presented FE model for a reference point on the winding. One can calculate the analytical deformation per V^2 by applying eq. (2.30). Given the geometry of the capacitor, the plate distance of the layers and the resulting electrical field, the deformation is calculated for a plate capacitor geometry.

Regarding the capacitor winding, this assumption is most valid in the middle of the flat winding surface. However, in order to consider the winding geometry, the analytical value can be compared to the evaluated deformation from the FE model presented in the previous section. For the validation measurements, different voltage loads were applied to the capacitor. The operation points of these measurements are summarized in Tab. 3.7.

Measurement set	AC voltage in V	Effective voltage in V^2	Deviation in %
1	2.5	3.125	1
2	2	2	1.25
3	2	2	1.25
4	1.5	1.125	1.67
5	1	0.5	2.5
6	0.5	0.125	5
7	0.5	0.125	5

Table 3.7: Operation points for the validation of the excitation model.

The potential measurement error is inversely proportional to the effective voltage of the winding. This can be explained by the fact that the signal-to-noise ratio increases with a decreasing measurement voltage. A signal noise of 0.05 V was determined in the measurement.

The validation also allows to evaluate a damping coefficient, which can be used for the analytical model as well as in the FE simulation. Since the winding was excited with an AC voltage of 5500 Hz, the effects of resonances have to be considered for the comparison. This allows to compare the measured amplitudes of different frequencies below the first resonance. A damping factor of $D = 0.014$ was used to compare the measurement data with the analytical model.

The comparison of the electrostrictive deformation from the measurements with the analytical model and the FE simulation is depicted in Fig. 3.20.

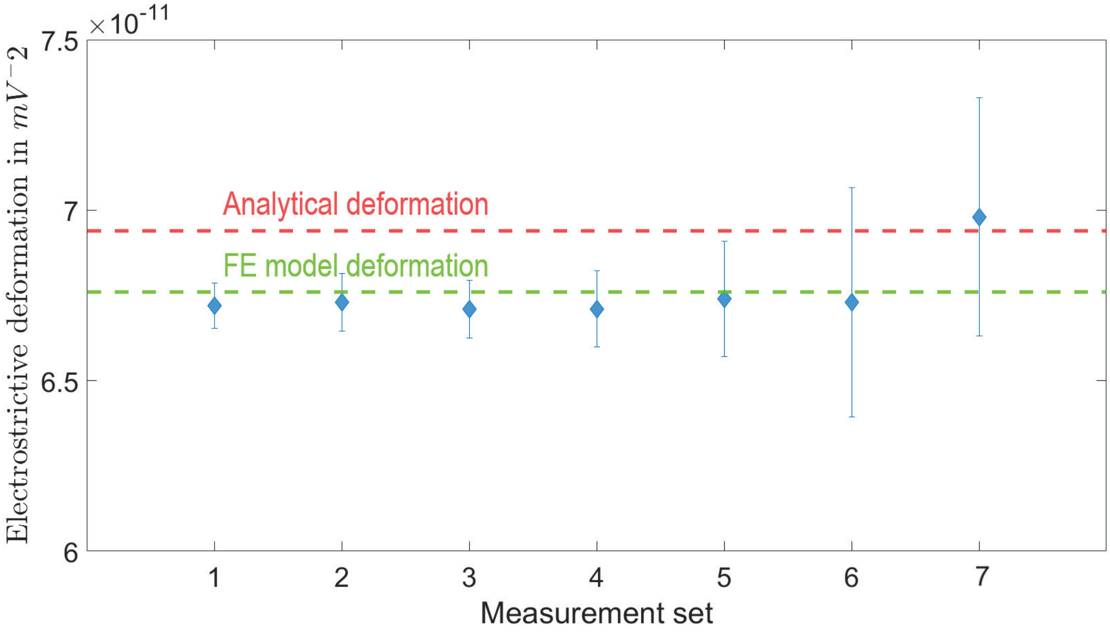

Figure 3.20: Verification of the excitation amplitudes of capacitor windings. The error bars are calculated due to the voltage sensitivity of the measurement setting. This leads to a bigger deviation for operating points with low voltages. The corresponding voltages for measurement one to seven are shown in Tab. 3.7 [41].

3.4 Summary

Within this chapter, a sensor model for PP-based strain sensors has been used to describe the electromechanical couplings of film capacitors. It has been shown that in order to neatly describe the electromechanical excitation of metallized film capacitors, the electrostriction has to be considered. The analytical excitation model has successfully been carried over to FE simulation in order to consider more complex geometries than plate capacitors. For this purpose, homogenized materials can be used. The excitation can either be applied via a thermal subsitute model with orthotropic strains or with the help of substitute pressures. The advantage of a pressure-based excitation is that model order reduction techniques can be applied, which safes computational costs.

The excitation model has also been successfully verified with laser vibrometer measurements based on low voltage operation points. As a result, the linear concept of electrostrictive strain coefficients is valid. However, this linear behaviour cannot be assumed for high voltage operation points, which will be discussed within the next chapters.

Chapter 4

Acoustical modelling of highly integrated power electronics

The film capacitor excitation model described in the previous section can be applied for highly integrated power electronics. Depending on the respective problem, different simulation levels can be considered. In this case, the excitation model has been applied to capacitor windings, full capacitor stacks and also to full inverter simulations. The different levels simulated within this work are shown in Fig. 4.1.

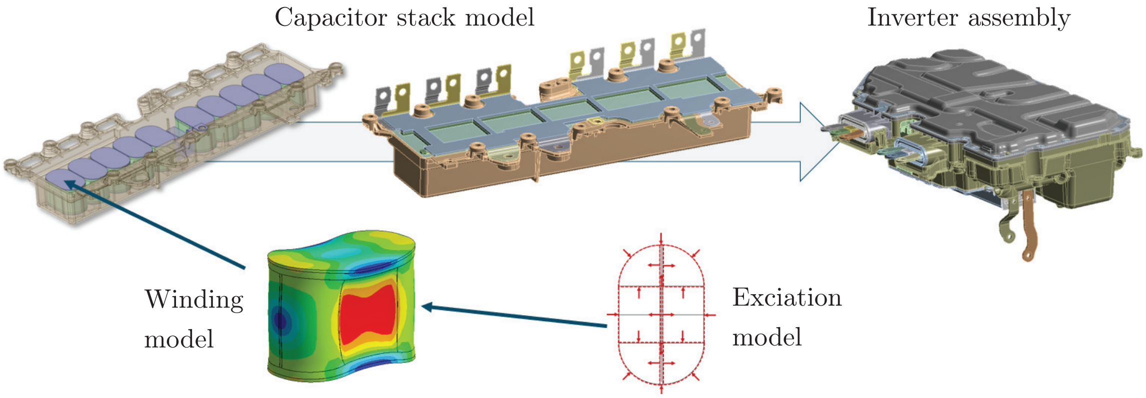

Figure 4.1: Simulation levels for the study of electromechanical excitation sources in power electronics.

4.1 FE modelling of film capacitor stacks

The structure of film capacitors has already been described in chapter 2. In the following, special features of the simulation of the DC-link capacitors will be discussed. In particular, the modelling of the potting compound is a challenge, since the mechanical parameters are usually not known a priori. This is not at least due to the fact that manufacturers of film capacitors provide only few information, since a suitable composition of the potting compound can represent an important competitive advantage. For this reason, it is important to know the mechanical properties of the capacitor materials.

As explained in chapter 3, the windings contract due to the voltage applied to the capacitor elements. This contraction is simulated in the FE environment as an orthotropic strain. For this purpose, orthotropic thermal expansion coefficients can be assigned to the capacitor windings, as described in chapter 3. Alternatively, the winding can also be modelled by the presented pressure-based substitute model. This is particularly recommended for more complex structures, e.g. a DC-link capacitor consisting of several windings. A meshed DC-link capacitor with a complex structure is shown in Fig. 4.2.

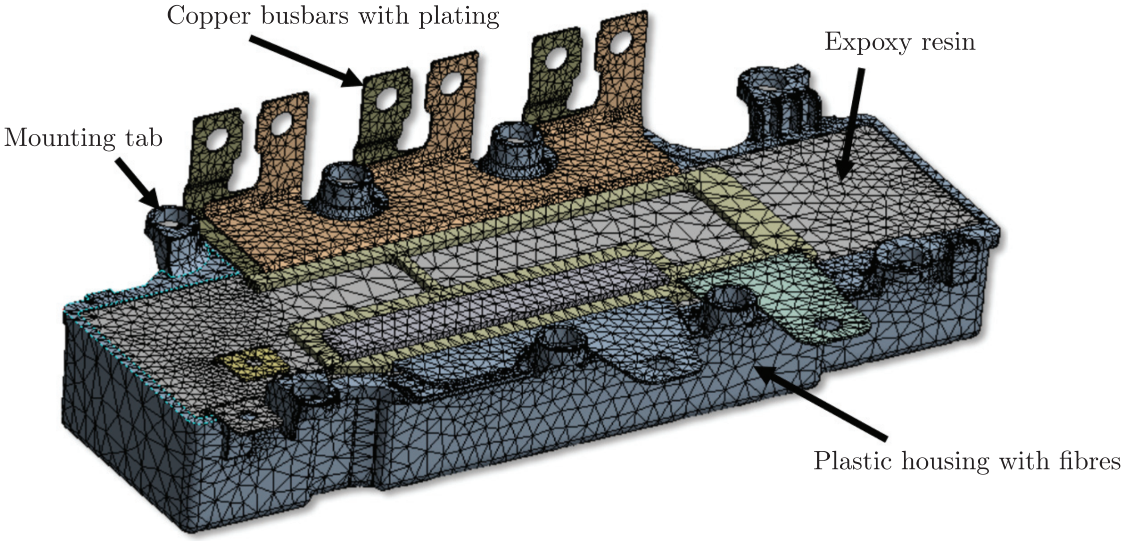

Figure 4.2: DC-link capacitor networked in FE environment consisting of 485000 nodes corresponding to 1455000 DOFs.

When setting up the simulation model, it is important to ensure that the potting compound shares its nodes with the windings, as this reduces modelling errors. This can be ensured in ANSYS Workbench via the shared topology setting and replaces contact conditions between the windings and the epoxy resin. The required strain for each winding can be calculated with the electrostrictive model presented before and is used to map DC and AC voltages applied to the capacitor.

The simulation model is based on material properties from literature as well as from dynamic mechanical thermal analysis (DMTA), which are shown in the appendix in section A.3. Against expectations, the measurements did not show a significant frequency dependence in the relevant temperature range, so the epoxy resin and the housing were simulated with a constant material damping. The derived material damping was 0.7 percent for the epoxy resin and 0.5 percent for the housing, respectively 1.4 percent and 1 percent of modal damping. Relevant material properties used for the simulation model are described in Tab. 4.1.

Material	ρ in kg/m^3	Y in GPa	ν
Expoxy resin	1.54	3.5	0.33
Housing PPS(GF+MD)	1.43	10.15	0.45
Copper busbars	8.93	110	0.3
Polypropylene	0.91	1.1	0.42
Schoop layer	7.14	108	0.36

Table 4.1: Material properties for capacitor simulation model.

As the capacitor is a complex geometric model, housing, busbars and epoxy were meshed with tetrahedral elements of the ANSYS element type Solid187. Only the windings have been meshed with hexahedral elements (Solid186), as presented in chapter 3. These solid elements use three translational degrees of freedom and have a middle node at every edge. Even though the busbar structures in particular suggest shell elements, the modelling effort exceeds the potential numerical performance improvement. The solid elements used for the simulation are based on quadratic polynomials.

4.2 Validation of the simulation model

In this section, the capacitor simulation is compared to measurement results. For this purpose, the exact electrical operating point in the measurement is relevant, so that the excitation can be set in relation to the acting voltage. This operating point is determined by a simple electrical model. In addition, the pre-polarization must be taken into account for each winding, which is described in section 3.3.2.

4.2.1 Measurement setup

The measurement setup for film capacitor stacks has also been described in [40]. In order to examine the relation between electrical operation points and the mechanical vibrations on the capacitor surface, vibrometer measurements are conducted. Therefore, the DC-link capacitor is exposed to different loads with a signal amplifier. As a result, the frequency-dependent AC voltage is a function of the impedance within the measurement. This includes the impedance of the capacitor as well as the impedance from the ripple generator and the supply cable itself. During the measurement, the capacitor is mounted with elastic bands to obtain free boundary conditions. Thus, no degrees of freedom are blocked, which allows a good comparability with the modal analysis results obtained by FE simulation. The AC excitation is superimposed with a constant external DC voltage, which is varied within the test. The corresponding setup is shown in Fig. 4.3.

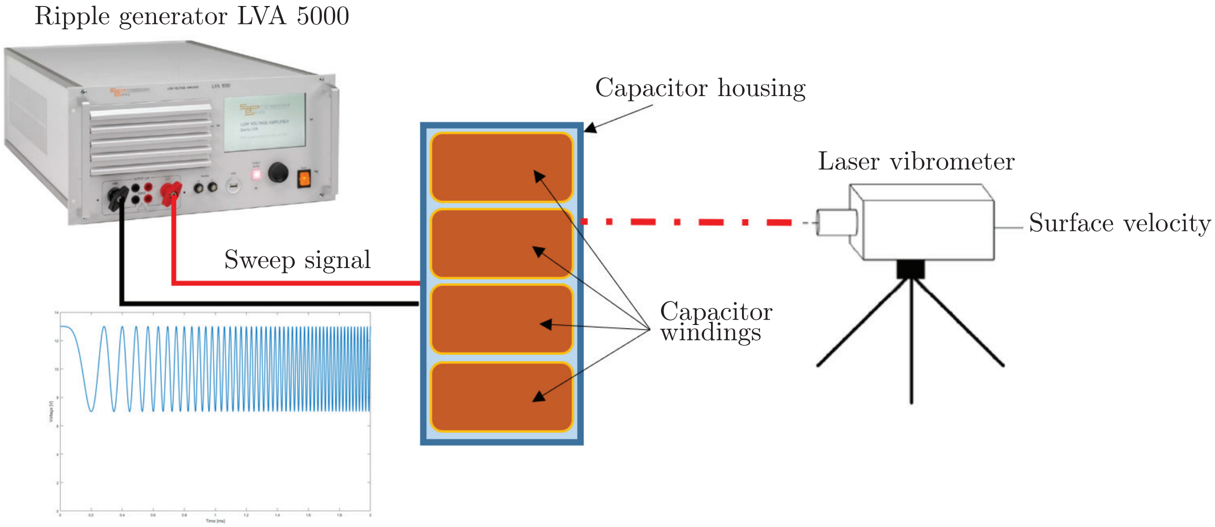

Figure 4.3: Excitation and measurement of a BOPP film capacitor stack. The electro-mechanical response is tracked via a laser vibrometer.

The ripple current signal is provided by the signal amplifier LVA 5000 from Spitzenberger and Spies [106] and consists of a direct part U_{DC} and an alternating part U_{AC}. The alternating part is controlled as a constant current signal I_{AC}. Depending on the frequency, the stimulating voltage U_{AC} is varying proportional to the frequency-dependent electrical impedance $Z(\omega)$. The voltage $U(\omega)$ can be calculated according to

$$U(\omega) = Z(\omega) I_{\mathrm{AC}}. \tag{4.1}$$

The AC signal is realized as a linear sweep signal in order to excite the full frequency range from 2 to 16 kHz in a short time. The sweep duration t_{sweep} in the experiment is 400 ms. The sweep is described in eq. (4.2) by using the increasing rate $\kappa = 17500$ and the initial frequency $f_{\mathrm{start}} = 2\mathrm{kHz}$. The sweep function $y(t_{\mathrm{sweep}})$ can be expressed as

$$y(t_{\text{sweep}}) = \sin(2\pi(f_{\text{start}} + \kappa\, t_{\text{sweep}})t_{\text{sweep}}). \tag{4.2}$$

Within the measurements, four surfaces of the capacitor housing are scanned. It should be mentioned that only one side is scanned directly and mirrors were used for the other 3 surfaces. This ensures that there is no influence on the device under test (DUT) by adjusting the measurement setup. In Fig. 4.4, the measurement setup is depicted from the view of the laser vibrometer.

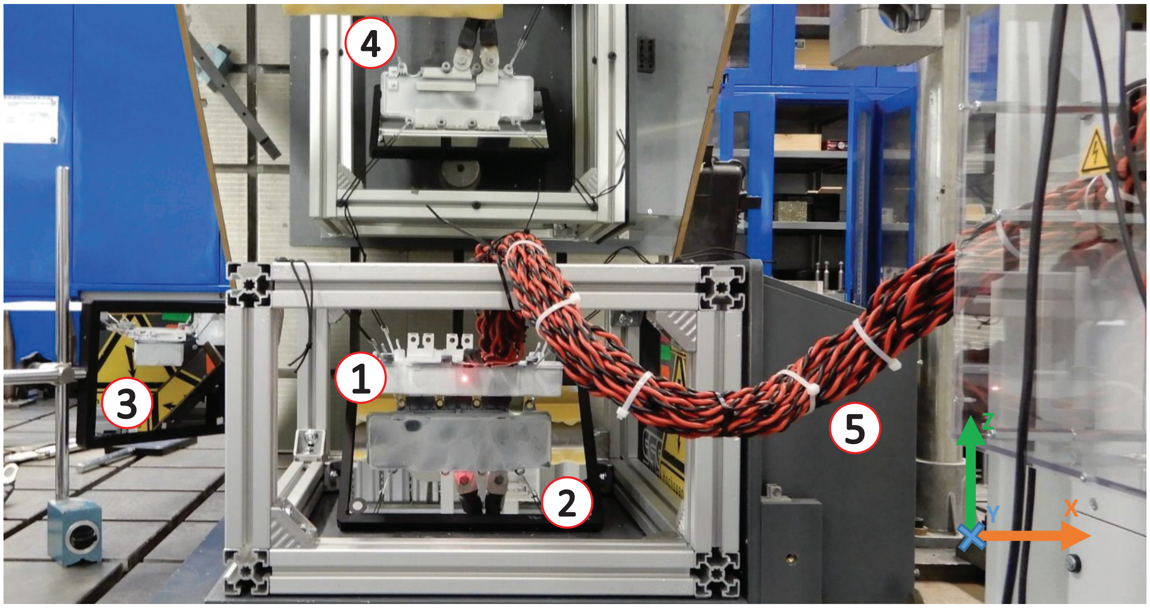

Figure 4.4: Configuration view from vibrometer perspective 1) Direct measurement of front view. Indirect measurement of 2) bottom view 3) side view 4) top view. 5) Low inductance cable.

In order to compare the measurement with the simulation model, the point velocities of one surface are used. A drilled low inductance cable is required to excite the capacitor efficiently. Since the capacitor was excited via a constant supply current, the voltage changes over the frequency range. This depends on the electrical impedance, which can either be taken from measurement or can be modelled via a simple substitute model shown in Fig. A.2 in the appendix. Since there is a phase shift between current and voltage over the frequency range (except at the resonant frequency), the voltage is defined as the phase reference for the excitation amplitude.

The frequency-dependent electrical properties of the capacitor can be modelled with a simplified approach. The impedance of the total system is composed from resistance, inductance and capacity of the supply cable, the capacitor and the output characteristics of the amplifier itself. For simplification, the capacitor can be seen as a component without resistance and inductance while the capacity of the supply cable can also be neglected. The corresponding impedance curve can either be taken from measurement or can be simulated according to a simplified model. The frequency-dependent impedance $|Z(\omega)|$ can be described as

$$|Z(\omega)| = \sqrt{(ESL \cdot 2\pi f - \frac{1}{C \cdot 2\pi f})^2 + ESR^2}. \tag{4.3}$$

Here, the ESL represents the equivalent series inductance of the supply cable while the ESR is defined as the equivalent series resistance of the measurement setup for the capacitor with its know capacity C. The corresponding phase angle $\phi_z(\omega)$ can be expressed as

$$\phi_z(\omega) = \cos^{-1} \frac{ESR}{|Z(\omega)|}. \tag{4.4}$$

Both approaches show a good agreement and are compared in Fig. 4.5. The electrical resonance in the measurement setup is just below 13 kHz and represents the point at which the phase angle between voltage and current corresponds to zero degrees.

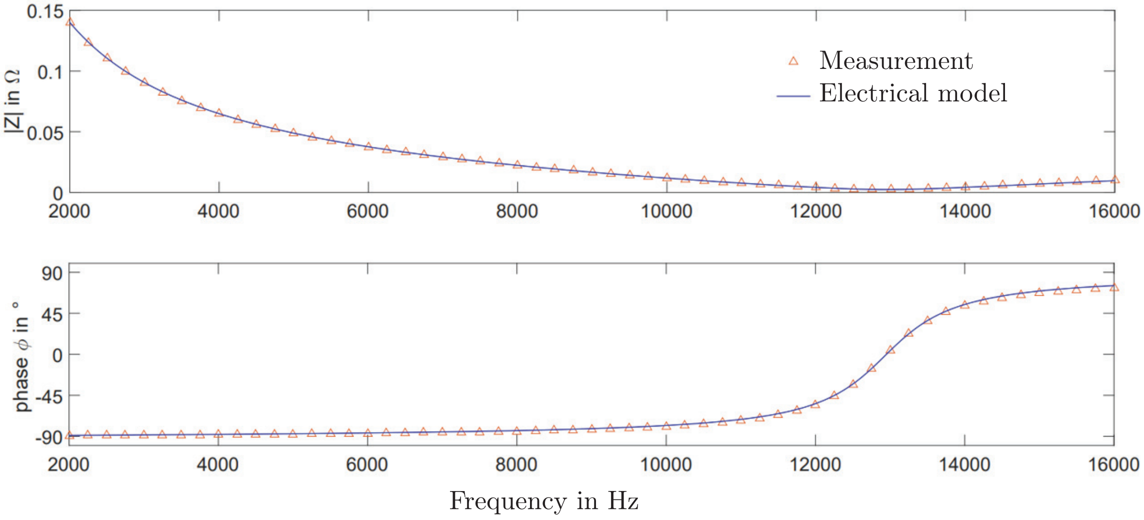

Figure 4.5: Alignment between electrical impedance model and impedance measurement.

The corresponding parameters evaluated for the measurement setup are summarized in Tab. 4.2. During the measurement or when changing the DUTs, it must be ensured that the supply cable is not moved, as this affects the inductance in the system and can change the voltage applied to the capacitor.

Parameter	**Value**
ESL	272 nH
ESR	3.4 mΩ
Resonant frequency	12953 Hz

Table 4.2: Fitting parameters for impedance curve.

While capacitive effects dominate in the lower frequency range, inductive effects prevail in the upper frequency range above the electrical resonance. At the resonance point, the impedance is at a minimum, which means that the capacitor is subjected to a minimum voltage. This resonance point f_0 is determined according to

$$f_0 = \frac{1}{2\pi\sqrt{ESL \cdot C}}. \tag{4.5}$$

It should be noted that the position of the resonance also depends on the exact position of the supply cable. It is therefore advisable to mechanically fix the supply cable throughout the measurement. In addition, the supply cable is twisted, which reduces its inductance and thus less current is required to excite a desired voltage ripple.

4.2.2 Comparison between measurement and simulation

In order to compare the measurement data to the simulation model, the point velocities of the top surface are used. If this surface is described with n scanning points where every point has the complex velocity v_i, the averaged surface velocity v_{avg} can be calculated as

$$v_{\text{avg}} = \frac{1}{n}\sum_{\text{i}=1}^{n}\sqrt{\Re(v_{\text{i}})^2 + \Im(v_{\text{i}})^2}. \tag{4.6}$$

Here, the effect of the phase cancellation is not considered. Nevertheless, it can be seen as a measure for the energy in the system and is proportional to the excitation from the capacitor windings.

During the measurement, both the AC component and the DC component of the excitation were varied. It was found that the excitation amplitude scales directly proportional to the AC component, as shown in Fig. 4.6.

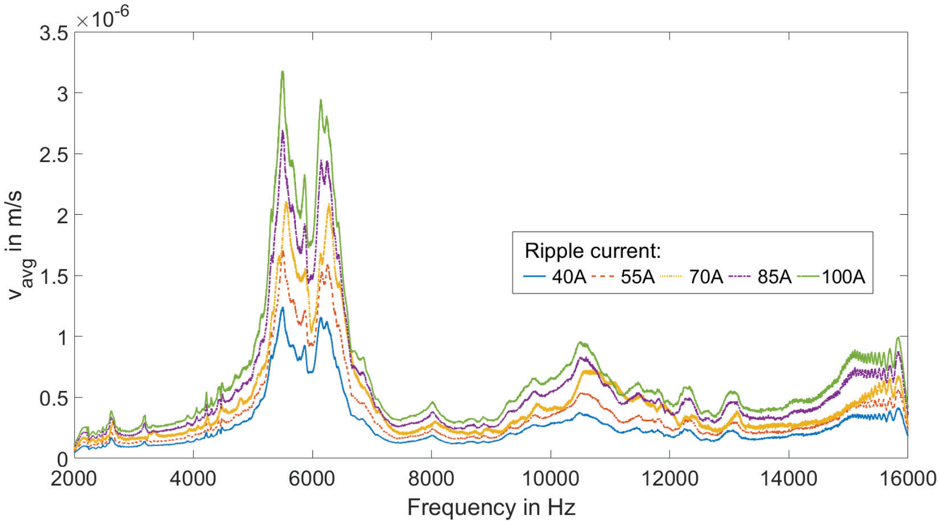

Figure 4.6: Scaling of the excitation amplitude with increasing ripple current.

The DC component does not follow the same logic. For example, a doubling of the applied DC voltage did not lead to a doubling of the excitation amplitude for the investigated capacitor. The measured spectra of the surface velocities with different DC excitations are shown in Fig. 4.7.

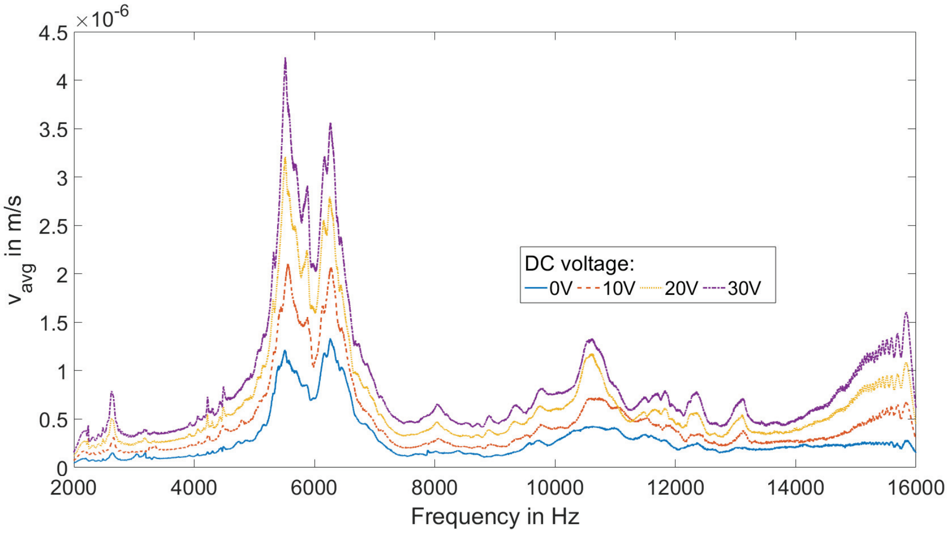

Figure 4.7: Scaling of the excitation amplitude with increasing DC voltage. Amplitude does not scale directly proportional to the applied DC voltage.

The reason for the non-intuitive response due to the DC excitation can be found in the compensation voltage introduced in section 3.3.2 . The pre-polarization leads to an electric field inside the windings, which can either compensate or increase the electric field from the external excitation voltage. Thus, it is possible to determine the value of the present compensation voltage of a capacitor winding even in the assembled state by evaluating the response to an external DC voltage.
In order to distinguish between the four windings, they must be localized. For this reason, the two main modes depicted in Fig. 4.8 can be used for an evaluation.

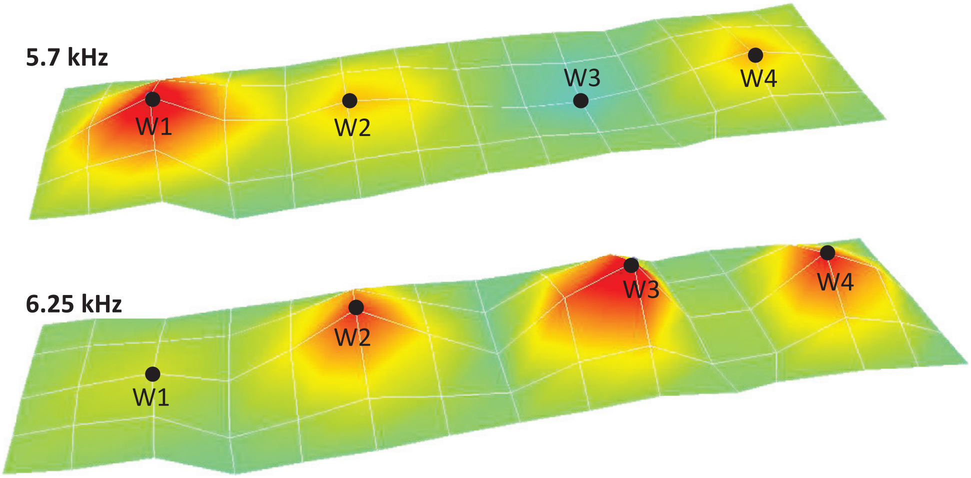

Figure 4.8: Localization of the windings one to four (W1-W4) inside the capacitor assembly. The main pumping modes can be used to calculate the pre-polarization.

Subsequently, the reaction of the windings to the external DC voltage can be evaluated and thus the present compensation voltage can be calculated for each winding independently. The surface velocities of the measurement point directly above the windings W1 to W4 for different external DC voltages and a constant AC voltage are summarized in Tab. 4.3.

U_{DC} [V]	W1 [m/s]	W2 [m/s]	W3 [m/s]	W4 [m/s]
0	8.76e-7	6.21e-7	7.65e-7	7.49e-7
10	15.37e-7	10.04e-7	12.49e-7	11.51e-7
20	21.53e-7	13.77e-7	17.11e-7	15.49e-7
30	28.62e-7	17.69e-7	22.21e-7	19.47e-7

Table 4.3: Surface velocities for measurement points directly above the capacitor windings.

These values show that even at an external DC offset of 0V, the fundamental oscillation is present. This can be explained with a DC offset or compensation voltage U_0 of the windings, which can be calculated for each winding separately. To calculate the compensation voltage from the values, linear interpolation can be performed as shown in Fig. 4.9.

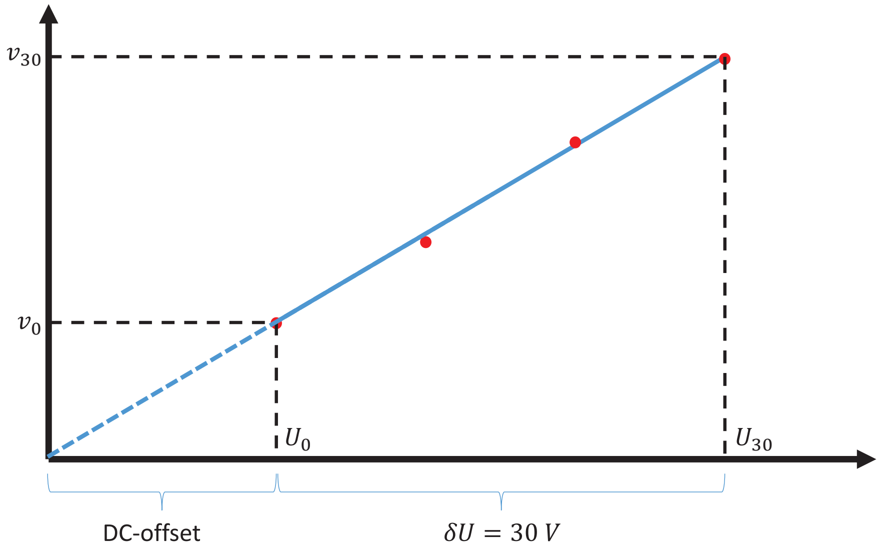

Figure 4.9: Calculation of the compensation voltage in assembled stage due to variation of the external DC-voltage.

Accordingly, the relation of the voltages of two operation points are proportional to the corresponding surface velocities, i.e.

$$\frac{U_{30}}{U_0} \propto \frac{v_{30}}{v_0} \qquad \Rightarrow \qquad U_{30} - U_0 = \delta U = 30. \tag{4.7}$$

These equations can be rearranged, which leads to an expression for the expected DC-Offset U_0. The DC offset can be calculated according to:

$$U_0 = \frac{\delta U}{\frac{v_\mathrm{i}}{v_0} - 1}. \tag{4.8}$$

As a result, the measured surface velocity is triggered by the sum of the external DC voltage U_DC and the initial polarization voltage U_0. This means that a switch of the polarity would have an influence on the excitation of the capacitor. The different compensation voltages for the exemplary capacitor are content of Tab. 4.4.

Winding	U_0 in V
W1	13.21
W2	16.23
W3	15.76
W4	18.76

Table 4.4: Compensation voltages of the different capacitor windings.

It must be mentioned that at least 14 months have passed between the production of the investigated capacitor and the acoustic measurement. Accordingly, a quasi-stationary state of the compensation voltage can be assumed.

These values can be used for FEM simulations in order to consider the divergent forces of the different capacitor windings. Using the electrical model and the experimentally determined compensation voltage of the windings, the effective excitation voltage of the capacitor can be determined. This can then be converted into an excitation model for the windings in the capacitor, for example, using the analogy model introduced in the previous chapter. The averaged surface velocity from the FE simulation can be compared with the vibrometer measurement, as shown in Fig. 4.10.

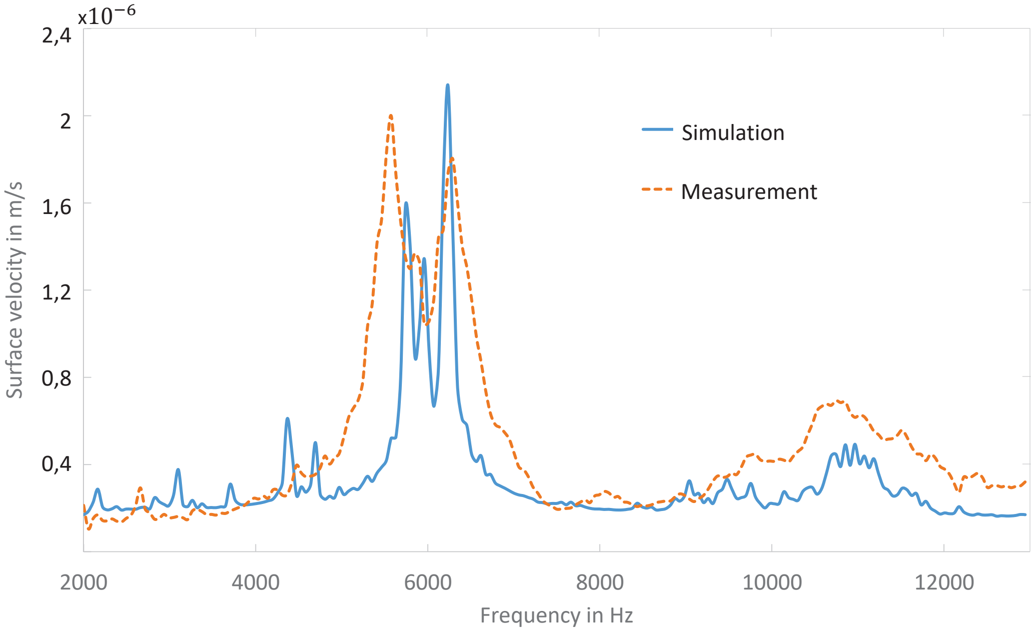

Figure 4.10: Superposition of the spectra based on the averaged surface velocity. The main modes can be predicted with the help of the FE simulation.

The comparison of the spectra shows a good match of the main excitation modes, where the excitation of the capacitor is at its peak. The largest amplitudes occur when the windings are excited in their pumping modes, which are transferred to the surface of the capacitor housing. The corresponding mode shapes of simulation and measurements are depicted in Fig. 4.11.

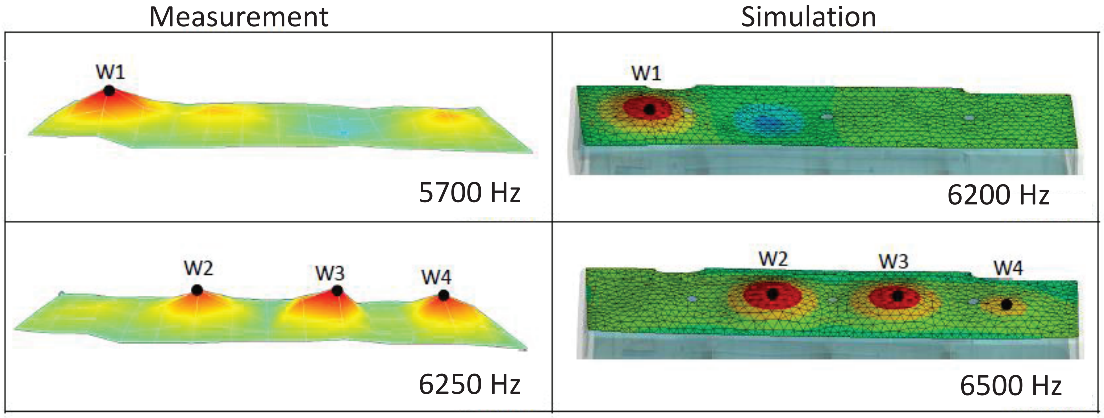

Figure 4.11: Comparison of modes from vibrometer measurement and simulation.

It should be emphasized that at a frequency of 5.7 kHz only the winding W1 goes into resonance, whereas the outer windings are excited at a slightly higher frequency of 6.25 kHz. The reason for this behavior is the different bond cross-sections on which the windings are connected to the copper busbar. In the capacitor under investigation, windings W2-W4 are connected with significantly more copper, which is presumably due to a thermally optimized busbar design with minimal copper use. As a result, the stiffness of the outer winding is lower, which leads to a lower resonant frequency.

Although the simulation method is able to predict the resonant frequencies, the simulation accuracy decreases for investigations at higher frequencies due to numerical reasons. An additional reason why the modes are missed by up to 500 Hz in the simulation is also the scattering among identical capacitors. For example, the winding positions of the condensers can differ significantly from each other, since they are often inserted into the capacitor by hand. Furthermore, the soldering process between the winding and the busbar is often subject to fluctuations, which is why the connection stiffness of the capacitors varies.

During the sweep measurement, the capacitor was already clearly audible, although the DC voltage of 30V is an order of magnitude lower than the real operating point in the vehicle. This can be easily understood on the basis of the surface pressure p, which can be estimated with the help of the density of the surrounding medium ρ_{air}, the sound velocity c_{air} and the surface velocity v using the expression

$$p = \rho_{air} c_{air} v. \tag{4.9}$$

A sound pressure of approx. 80×10^{-5} Pa is obtained for the resonance, which already exceeds the hearing threshold by a factor of 40. If this resonance frequency is now excited exclusively, the amplitude can be increased significantly, as in contrast to sweep excitation, a steady state is achieved. Despite a DC voltage of only 30 V, a sound velocity of $1,52 \times 10^{-4}$ m/s has been observed. This results in a theoretical maximum surface pressure of 6×10^{-2} Pa or a sound pressure level of almost 69.5 dB. This roughly corresponds to the sound pressure level of a loud conversation.

For an external DC voltage of 30 V, the previously introduced compensation voltage must be considered in order to derive the correct excitation. Since this voltage is around 16 V on average for the four windings, the effective DC voltage is in the region of 46 V. If the capacitor is now exposed to the battery voltage of 400V that prevails in the vehicle, the effective voltage should be 416 V, i.e. the effective voltage would scale by a factor of nine. The theoretical maximum surface pressure is then 0.54 Pa, which corresponds to a maximum sound level of 88.6 dB. However, as these values are based on worst-case assumptions and do not take into account the radiation efficiency, reference is made in the following section.

4.3 Airborne sound radiation

The electrical excitation of the capacitor leads to mechanical oscillations on the housing surface, which result in airborne sound radiation. Since the simulative determination of the radiated sound power is connected with high expenditure and is not the focus of this work, an approach from the literature can be used. The radiated sound power is estimated by applying the radiation model for film capacitors from Zhu et al. [130].

As a reference, the capacitor introduced within the previous sections will be used. More specifically, the mode shape with three pumping windings from Fig. 4.8 can be examined for the corresponding sound radiation. Based on known normal surface velocities v_n, the radiated power W_{rad} can be approximated by

$$W_{\text{rad}} = \rho_{\text{air}} c_{\text{air}} S v_n^2 \Xi. \tag{4.10}$$

The pumping modes of the capacitor windings W2, W3 and W4 are expected to cause sound radiation at three hotspots. The corresponding mode from the measurement occurs at 6250Hz. The propagation of the acoustic wave can be resolved in time domain with a slightly different experimental setup using a laser vibrometer. For this reason, the space above the capacitor is scanned with a fine grid. The scanning laser is reflected at a rigid panel.

If the laser intersects with the sound wave, the higher pressure inside the wave has a different refractive index, which results in a frequency shift of the laser frequency. These pressure induced fluctuations can be visualized. The corresponding measurement setup is shown in Fig. 4.12.

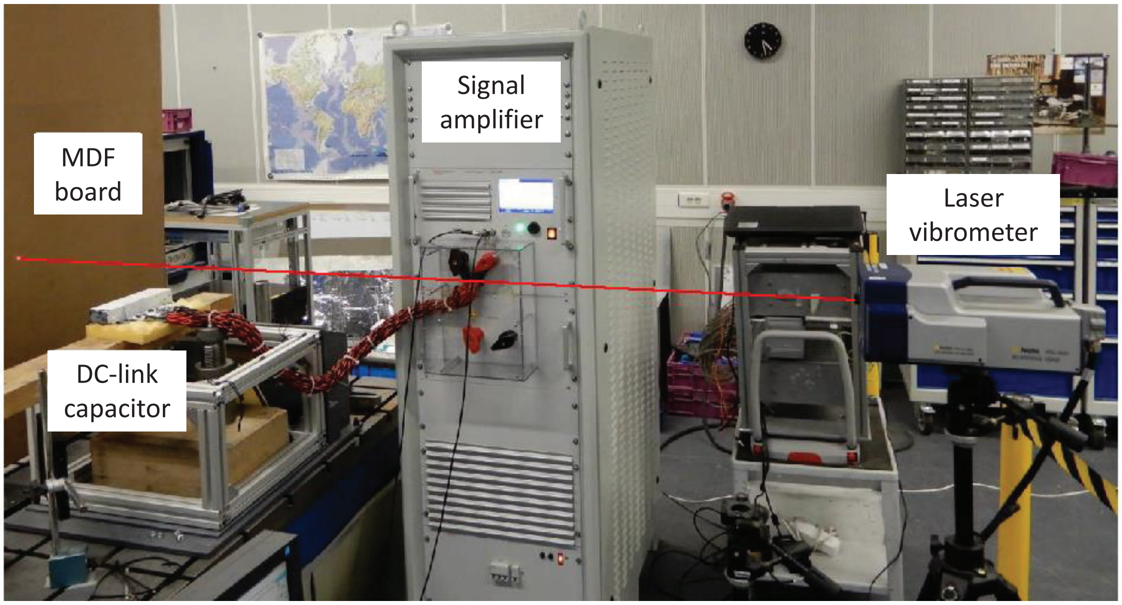

Figure 4.12: Measurement setup for the visualisation of the acoustical sound wave based on capacitor vibrations.

The propagating sound wave is depicted at a certain time in Fig. 4.13. It must be noted that the reflection panel may not be perfectly rigid, which could influence the measurement results. Nevertheless, the radiation spots and the measured wavelength of the corresponding sound wave depicted in Fig. 4.13 matches with the expected airborne sound radiation.

The radiated sound power of a winding can be approximated by using the capacitor sound radiation model of Zhu et al. [130]. The relation between radiation efficiency Ξ, frequency f, sound velocity c and geometrical feature size d of the radiating surface can be written as

$$\log \Xi = -\log(1 + 0.1\frac{c^2}{(fd)^2}). \tag{4.11}$$

The corresponding size of the radiating surface can be derived from the size of the excitation hotspot. For the capacitor excited at a frequency of $f = 6253$ Hz, this surface has a size of $1.25 \cdot 10^{-3}$ m^2, which corresponds to a feature size $d = \sqrt{\frac{S}{\pi}} = 2 \cdot 10^{-2}$ m. Inserting these values into eq. (4.11), the radiation factor can be approximated as $\Xi = 0.57$.

Combining the measured average surface velocities of the windings 2, 3 and 4, the radiated sound

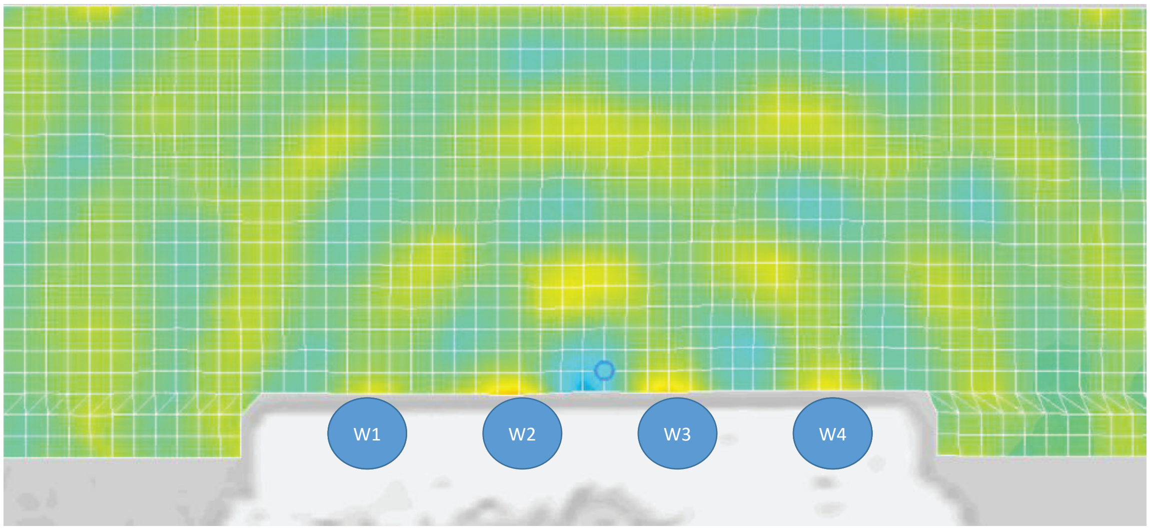

Figure 4.13: Measurement of sound wave propagation.

power levels L_w can be calculated for each winding. Here, the sound power can be transformed into a sound power level by using the reference value $W_{\text{ref}} = 1 \cdot 10^{-12}$ W. This leads to the expression

$$L_w = 10 \log \frac{W_{\text{rad}}}{W_{\text{ref}}} = 10 \log \frac{\rho c S v_i^2 \Xi}{W_{\text{ref}}}. \tag{4.12}$$

The average surface velocity v_i above each winding as well as the radiating surface can be approximated from the measurement data. The evaluated results are summed up in Tab. 4.5.

Winding	1	2	3	4
Radiating surface [m^2]	1.25 e-3	1.25 e-3	1.25 e-3	1.25 e-3
Compensation voltage [V]	13.21	16.23	15.76	18.76
v_i for $U_{\text{DC}} = 30V$ [µm s^{-1}]	127	554	503	449
L_w for $U_{\text{DC}} = 30V$ [dB]	30.4	43.2	42.3	41.4
v_i for $U_{\text{DC}} = 400V$ [µm s^{-1}]	1215	4991	4567	3853
L_w for $U_{\text{DC}} = 400V$ [dB]	56.3	68.6	67.9	66.4

Table 4.5: Estimation of radiated sound power of pumping windings.

The results show that capacitor windings excited at the resonant frequency are a relevant source of interfering noise. If the three winding hotspots are understood as three sound sources, the total sound power level emitted at a DC voltage of 30 V is 47.9 dB, which is limited to only one frequency and thus has considerable potential as a source of interference.

If the compensation voltage of the windings is taken into account, a radiated sound power level of 72.6 dB can be expected at an external DC voltage of 400 V. This corresponds to the sound power level of a normal conversation. However, due to the tonality of the noise, the radiation of the capacitor will be perceived as significantly more disturbing.

4.4 Capacitor excitation on the assembly level

Within the scope of this work, complete inverter models were also simulated. Thereby, the presented pressure models provide an important advantage, since the DOFs increase to a very high level. Without the use of modal superposition, the model size can only be handled with large resources. To investigate the influence of the DC-link capacitor, different modelling approaches can be used. The structures modelled in this work with different levels of detail are shown in Fig. 4.14.

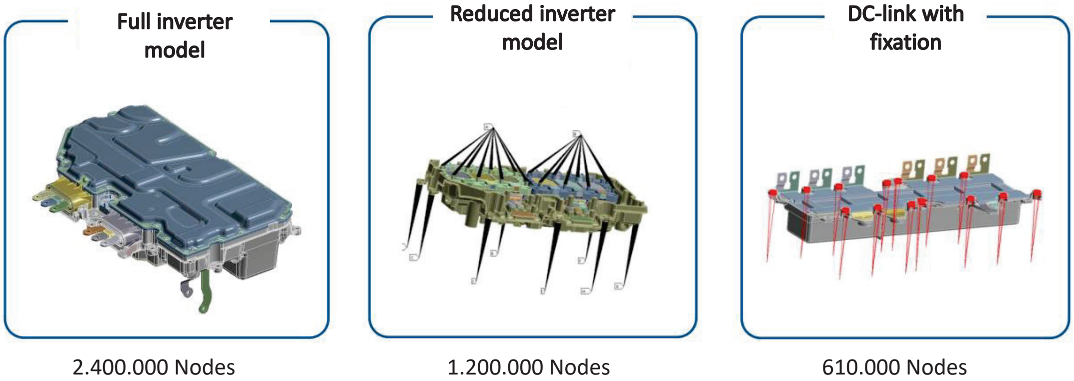

Figure 4.14: Models of different levels of detail to assess capacitor excitation.

The capacitor can be supported using bearing conditions at the screw-on points to map the stiffness in the inverter. Another possibility is the simplified modelling of the inverter. For this purpose, only heavy components are modelled, which are important for the stiffness and mass distribution of the inverter. The different ERP spectra of the capacitor surface between the modelling approaches is shown in Fig. 4.15.

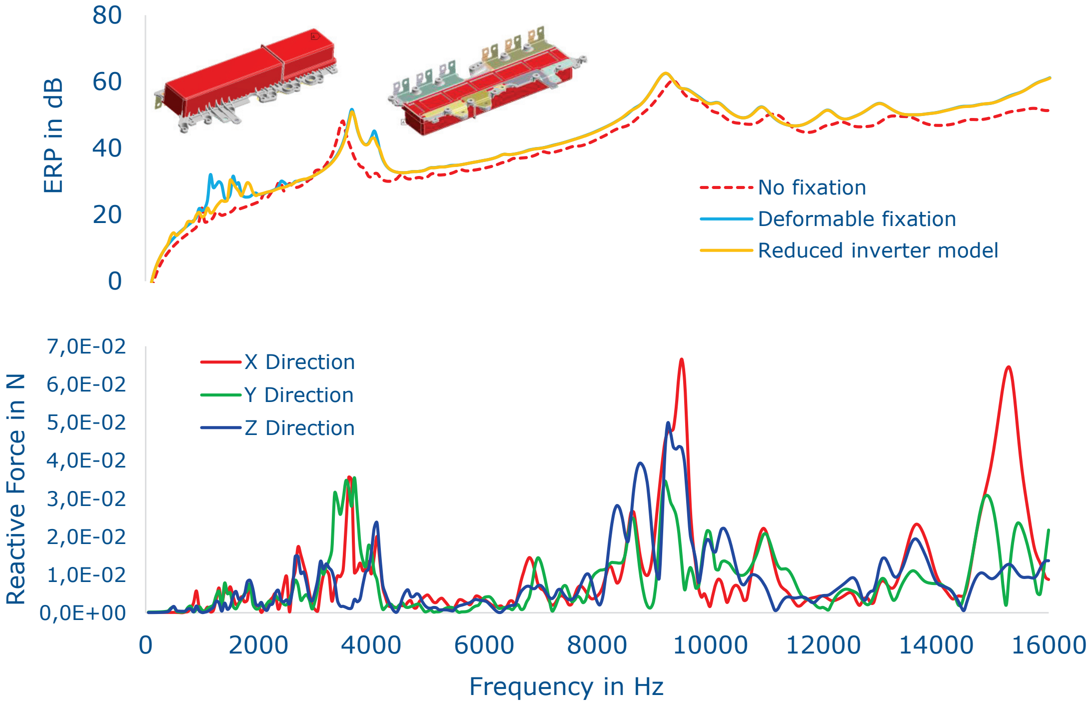

Figure 4.15: Simulation on assembly level.
Top: Sound power of the capacitor in the inverter estimated by models of different complexity.
Bottom: Three-dimensional evaluation of the reaction forces at an inverter screw-on point.

It becomes clear that even capacitor-based models are already suitable for assessing the acoustic excitations in power electronics. The full inverter model without simplifications is not suitable for harmonic analyses due to the high resource requirements. In particular for the airborne noise emissions to be determined, this model also does not provide any added value compared to the reduced models.

4.5 Summary

In this section, a multiphysical substitute model was presented. It describes the excitation mechanisms in a DC-link film capacitor. Thus, it is possible to qualitatively map an experimentally determined frequency spectrum for a film capacitor in a frequency range of 2-14 kHz.

For the validation, a capacitor was excited with the help of a ripple generator and the surface velocity was measured with a laser vibrometer. Different modes became visible, which can be traced back to excitations of the capacitor windings.

The applied ripple currents lead to an electromechanical excitation which is triggered both by the constant DC voltage and by the time-dependent AC voltage. The frequency-dependent operating point is determined using an electrical model. The comparison with the measurement results also requires the consideration of the previously introduced compensation voltage. Apart from the electromechanical excitation, the sound radiation of film capacitor stacks was also investigated. If the capacitor is excited at a resonant frequency, interference noise can occur even at low voltages. For one characteristic mode, the sound radiation was visualized with the help of a laser vibrometer. In addition, the radiated sound power level was estimated using an analytical model.

Finally, the film capacitor was also simulated within a full inverter assembly. For these simulations, it is highly recommended to apply reduced models based on the pressure based substitute excitation. By considering only the most important structural components and using modal superposition, the acoustic modeling of a complete inverter could be implemented with a reasonable expenditure of resources.

Chapter 5

Investigation of polarized dielectrics

For the prediction of the acoustic excitation of BOPP-based capacitor windings, polarization effects described in Section 2.5 are considered. As mentioned before, these polarizations are generated within the production process of film capacitor windings and remain quasi-stable at a certain value. This can be concluded from the fact that even after a storage period of two years at room temperature, the polarization in the winding is still acoustically detectable. The storage of charges and the quasi-permanent electrical field inside the dielectric material can also be linked in the context of electret materials. As a result, a polarized bobbin can be compared to an electret microphone, where a small external voltage can lead to a comparatively high excitation amplitude. On the other hand, the field triggered by the external voltage can also point in the opposite direction than the field stored internally, which enables a cancellation of the external and the internal field. This effect can potentially be used to improve the acoustic properties of a film capacitor winding.

5.1 Electro-acoustic measurement of the compensation voltage

For the acoustic measurement of the compensation voltage introduced earlier, a measurement approach for a simplified characterization is provided. Using a combination of AC and DC voltage, a minimum in the radiated sound power level can be found as a function of the applied external DC voltage. The measurement consists of two steps:

- AC Sweep for frequency characterization;
- DC Sweep for determination of the compensation voltage.

In order to specify the initial polarization caused by the manufacturing process of BOPP-based capacitor windings, a measurement setup is introduced. For the bobbin characterisation, the interaction between polarization and acoustic emission is evaluated. Therefore, the capacitor is excited by a combination of AC- and DC-voltage, while the acoustic answer from the electromechanical excitation is monitored with a condenser microphone. The basic measurement setup is shown in Fig. 5.1.

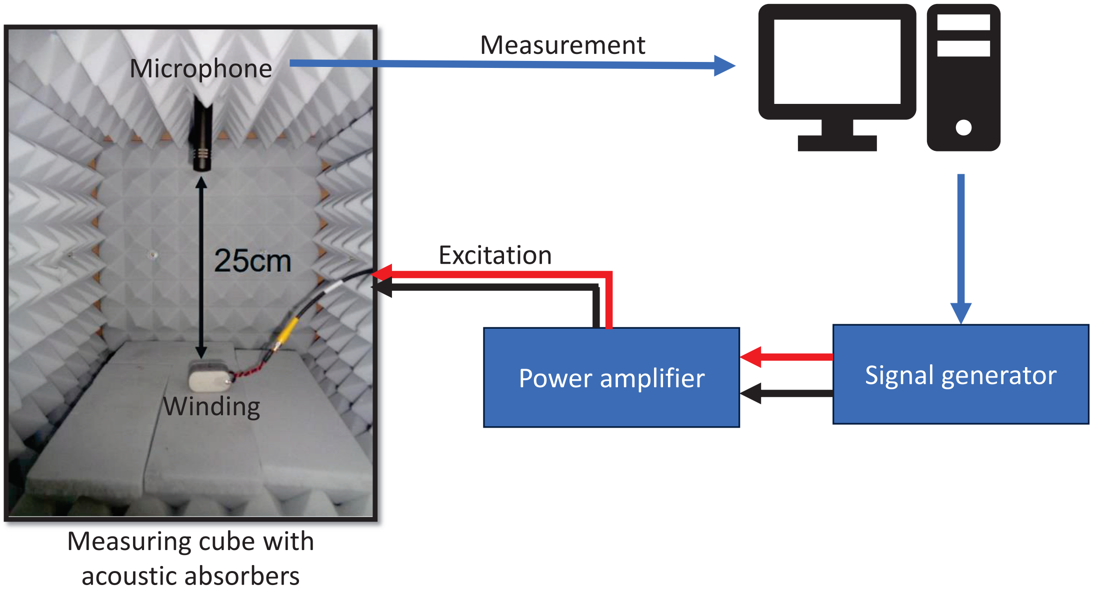

Figure 5.1: Measurement setup for acoustic AC-Sweep and DC-Sweep measurements to determine the compensation voltage. Condenser microphone used: AKG P170 [2].

The acoustic measurement is conducted inside a cube lined with sound absorbers in order to avoid a standing wave due to sound reflections from the walls. This ensures that the measured sound pressure level depends only on the distance to the winding and not on other position coordinates. At first, the AC sweep measurement is required to find an optimized excitation frequency in order to have high excitation amplitudes, in particular at resonance frequencies. Then, the signal to noise ratio is optimized, which allows precise measurements at low power operation points. The spectra for three exemplary capacitor windings with the same geometry are shown in Fig. 5.2 and differ only slightly from each other.

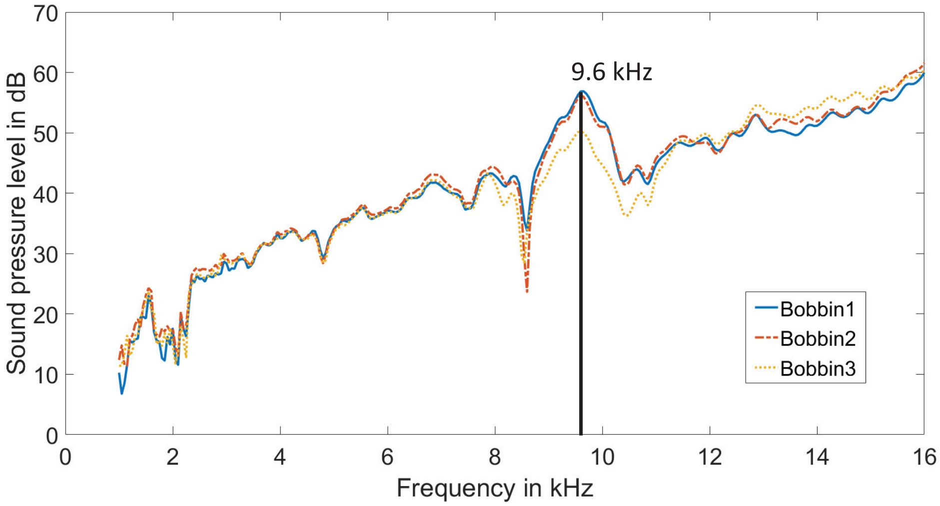

Figure 5.2: AC sweep to determine the first resonance of capacitor bobbins.

In a second step, the DC voltage is varied while the frequency of the AC voltage is kept constant at a fixed amplitude. The corresponding measurement is used to evaluate the compensation voltage U_{comp}. An exemplary result curve of this DC sweep is depicted in Fig. 5.3.

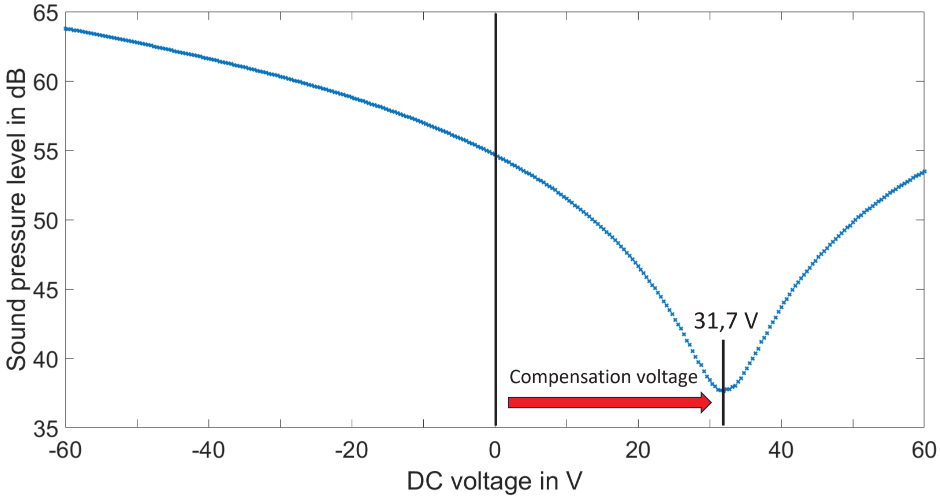

Figure 5.3: DC Sweep for a specific bobbin. The DC voltage with the lowest acoustic amplitude corresponds to the compensation voltage of approx. 31.7 V for the examined bobbin.

In the DC sweep measurement, the point of the lowest amplitude is the only one relevant for the subsequent evaluations. This enables conclusions about the intrinsic polarization of the capacitor bobbin, as the minimum directly corresponds to the compensation voltage. The sound pressure level is irrelevant here, which is why a voltage signal can be processed directly as microphone output. This is evaluated linearly in the further course, thus the curves shown for the determination of the compensation voltage can be de-logarithmized.

If the capacitor excitation voltage is increased to a certain level, saturation effects can be observed. As a result, the saturation has to be considered especially for high voltages. In particular, if the compensation voltage is not inside the measurement range, it has to be approximated by a suitable fit function. The function used in this work is an empirical approach. The tangent hyperbolicus is suitable to represent saturation effects at higher voltages. The fit function $f(x)$ for the de-logarithmized measurement curve is written as

$$f(x) = a + b \cdot |\tanh(c(x-d))|. \tag{5.1}$$

An exemplary measurement were the compensation voltage is not inside the measurement range is shown in Fig. 5.4.

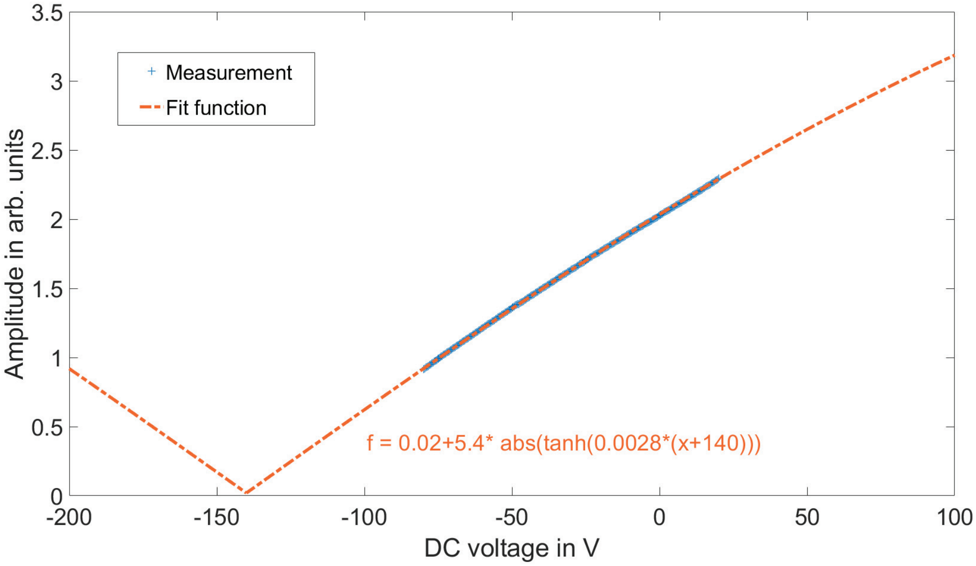

Figure 5.4: Fitting the measurement data with a tangens hyperbolicus function to consider saturation effects within the excitation.

The fit function shows almost a perfect match with the measured data. This is only achievable by supplying a sufficiently long voltage signal for every DC point during the DC sweep. Within the measurements, a settling time of 200 ms is used. Significant measurement deviations were found for lower settling times. This effect can be seen in Fig. 5.5. It becomes clear that if the settling time is too short, the measured values will deviate to lower amplitudes since the maximum acoustic level cannot be reached.

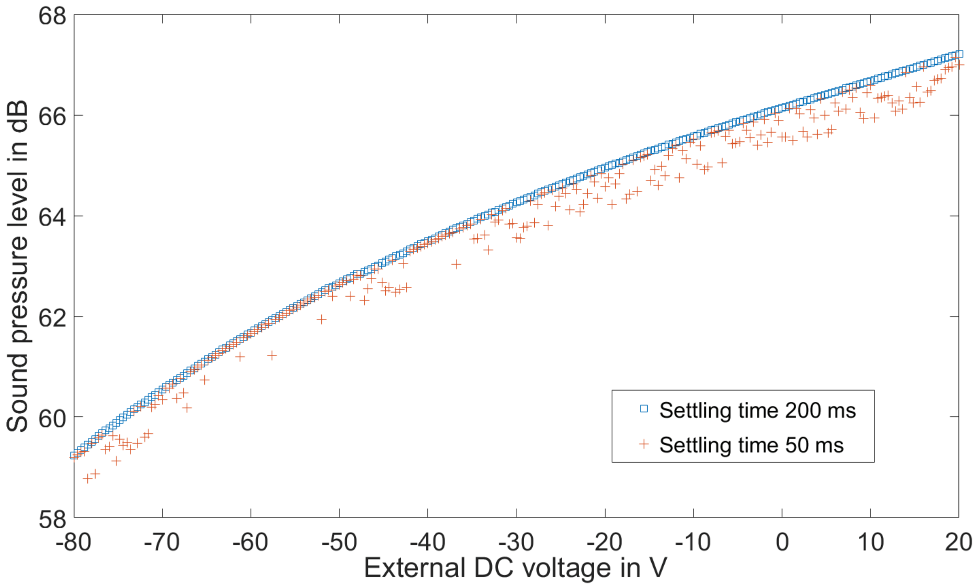

Figure 5.5: Influence of settling time on measurement noise.

5.2 Influences on the compensation voltage

In this section, the stability of the compensation voltage is investigated. The polarization is always done by applying a short voltage pulse, further referred to as HV conditioning. All tested capacitor windings are designed for a nominal voltage of 450 V and have a BOPP film with a thickness of 2.4-2.7 μm as a dielectric. Nevertheless, a voltage pulse up to 1100 V can be applied for a short time at room temperature without having a significant effect on the capacitance.

5.2.1 High voltage conditioning of capacitor windings

Utilizing an isolation testing device, it is possible to externally manipulate the compensation voltage with high voltage test pulses. Depending on the capacitor geometry, a certain voltage level leads to a distinct change of the polarization and thus the compensation voltage. It has been ensured to completely discharge the capacitor after HV treatment before starting the acoustic measurements. In order to not damage the capacitor, the amplitude of the HV pulses was within 2.5 times the rated voltage for the capacitors. In the following, the application of voltage pulses will be referred to as HV conditioning, which allows to increase, decrease or even change the sign of the compensation voltage. The stability of the changed polarization depends on the magnitude of the pulse. For a higher compensation voltage, a faster decay can be monitored.

To verify that the HV conditioning is reproducible, an untreated winding is first polarized in both directions at ± 550 V. This was an unused winding that had already been stored for almost two years. Nevertheless, in the inital state it showed a compensation voltage of 39.2 V. The change of the compensation voltage due to external HV pulses is shown in Fig. 5.6.

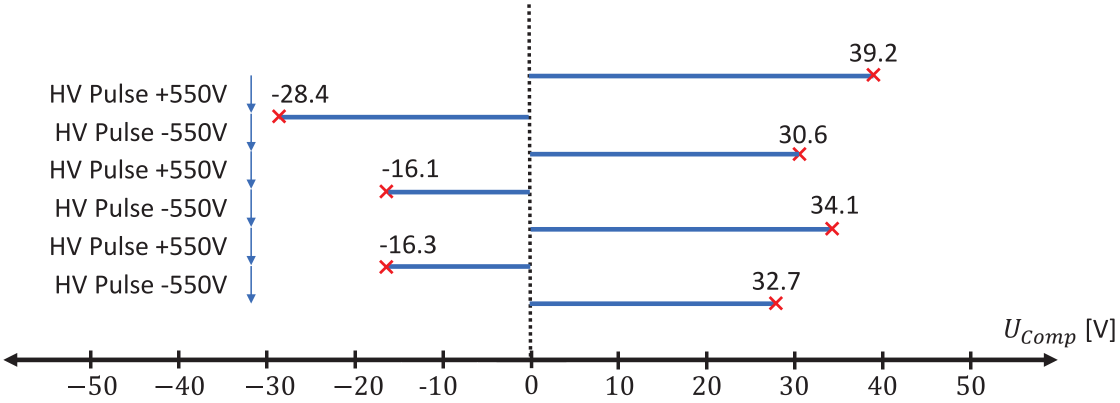

Figure 5.6: Reference winding for HV conditioning.

HV conditioning enables the reversal of polarization within the winding. In this case, the winding was discharged after each conditioning step and the voltage can not be measured directly on the capacitor contacts. Due to the existing pre-polarization in the winding (from manufacturing), the values of the compensation voltage are shifted to the positive half-plane. In the example of the measured winding, the value settles in the range -16 V/ +33 V during conditioning, that means it settles approximately symmetrically to +8.5V. It can be concluded that the preferred direction of the winding cannot be completely eliminated by the applied voltage pulses.

5.2.2 Relaxation over time

Since compensation voltages of 31 V to 40 V were measured for bobbins stored for over two years at room temperature, these values can be assumed as quasi-stable, depending on the bobbin geometry and the capacitor supplier. If a voltage pulse near the breakdown limit of the dielectric is applied, much higher values for the compensation voltage can be achieved.

For this reason, another capacitor winding is exposed to a voltage pulse of 1100 V. As a result, a compensation voltage of around 210 V is achieved directly after the HV conditioning process.

However, a compensation voltage of this margin is not stable over time. The measured decay of the compensation voltage over one month is therfore shown if Fig. 5.7.

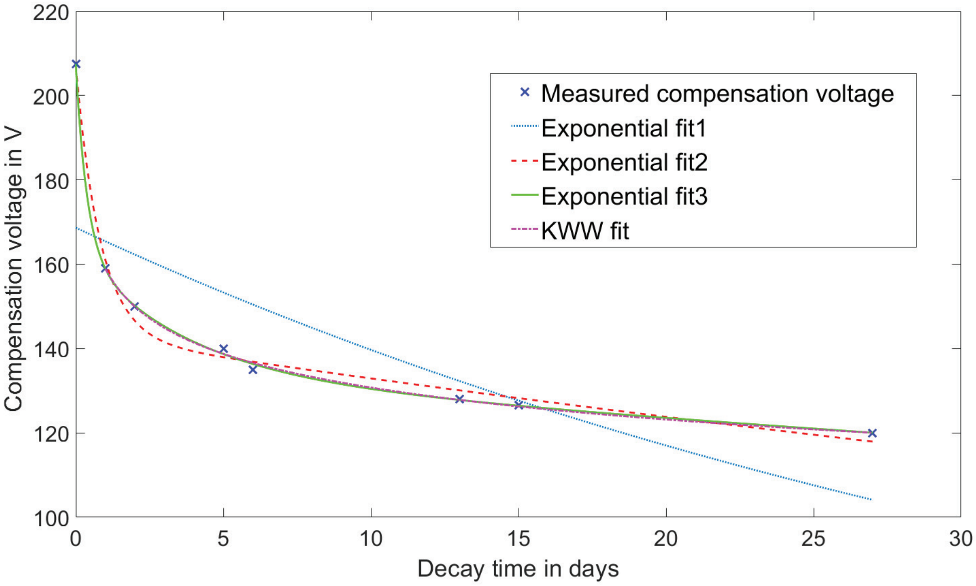

Figure 5.7: Relaxation of the compensation voltage over time.

In order to describe this decay as a function of time at room temperature, one can employ an exponential decay function as a sum of numerous exponential terms with the form

$$U_{comp}(x) = ae^{-bx} + ce^{-dx} + fe^{-gx} + h. \tag{5.2}$$

The constant h represents the quasi-stable long-term compensation voltage, e.g. 35V in the case of the analysed capacitor winding. If the measured data is fitted by using one to three exponential decay terms, different fit errors are obtained as shown in Tab. 5.1.

Another fit function presented within the fundamentals is proposed by Kohlrausch-Williams-Watts (KWW) and can be formulated analogous to

$$U_{comp}(x) = 162.7 \exp\left(-0.0047x\right)^{0.228} + 35. \tag{5.3}$$

This fit leads to a good quality with a RMSE = 1.43. Even though the fit quality is similar to the exponential fit functions, it should be mentioned, that the KWW-fit has no connection to a physical model and is rather a purely empirical function that fits the data to the same degree as the sum of three exponential functions with a similar coefficient of determination. However, it has the advantage of a lower amount of fit parameters.

Fit parameter	**Function 1**	**Function 2**	**Function 3**
a	124.6	105.8	32.57
b	0.0126	0.00631	0.0972
c	-	56.19	86.73
d	-	1	0.00122
f	-	-	43.16
g	-	-	1.798
h	35	35	35
RMSE	16.48	3.51	0.69

Table 5.1: Fit parameters for exponential fit functions.

The measurements show that even higher values of the compensation voltage remain stable for a relatively long time. The decay can best be described with several exponential terms, which indicates the presence of different discharge mechanisms. This suggests that several depolarization mechanisms overlap in the dielectric. This behaviour is also common to electrets, comparable measurements were presented in a recent study by Gerlach et al. [29]. Here, fluorocarbon electrets are investigated under elevated temperatures and the potential decay is monitored over 1200 days. It was also found that the decrease in polarization in samples can be reduced if they are charged at elevated temperatures. This would also be an interesting field of research for capacitor windings, as HV conditioning can also take place at elevated temperatures. However, this was not investigated in this thesis and represents a potential prospect for future investigations.

5.2.3 Temperature stimulated relaxation

In order to better understand the behavior of the compensation voltage, the capacitors reaction to temperature loads is tested. This is achieved by a comparison of the compensation voltages before and after HV conditioning and before and after heat treatment. In total, four capacitor windings are exposed to thermal treatment. Two windings (W1 and W2) are only exposed to higher temperatures, either 90 °C or 120 °C. The other two windings (W3 and W4) are exposed to a combination of HV pulses and heat treatment. In order to make sure that the capacitors undergo a significant temperature treatment, a reference winding with a drilled hole and a thermal sensor in the center of the bobbin is used. This additional measurement bobbin for a temperature reference signal is shown in Fig. 5.8.

This makes it possible to keep track of the core temperature since the other capacitor windings have the same geometry. As soon, as the core temperature reaches a temperature of 2 °C less than desired, the timer for the effective treatment starts. The capacitors are kept at this temperature for 30 minutes. This procedure guarantees that the desired temperature is reached for all layers of the bobbin. The temperature profile for a reference temperature of 100°C is shown in Fig. 5.9.

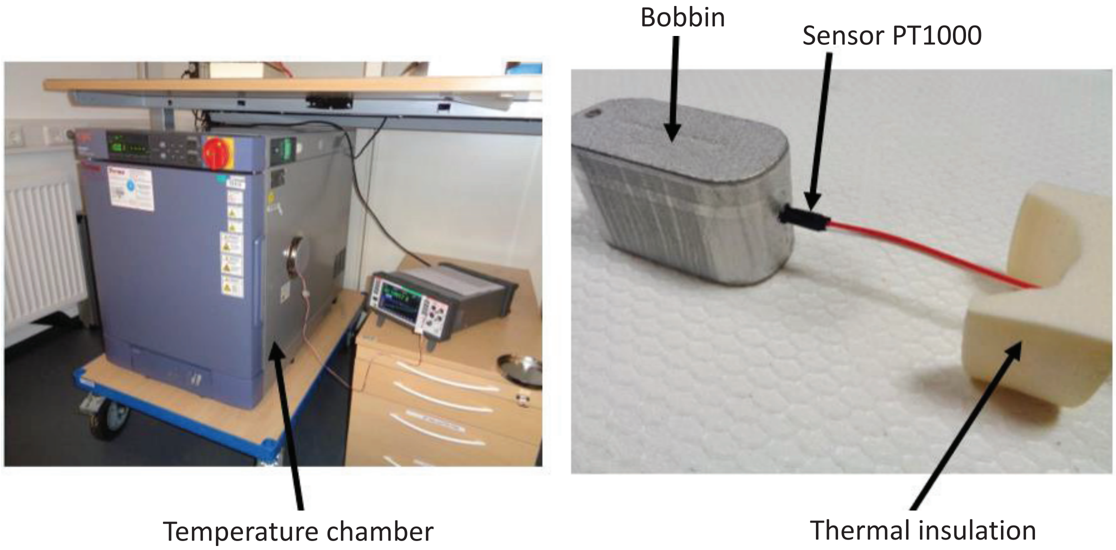

Figure 5.8: Left: Measurement setup with temperature chamber for heat treatment.
Right: Reference bobbin with thermal sensor for temperature tracking inside the winding core.

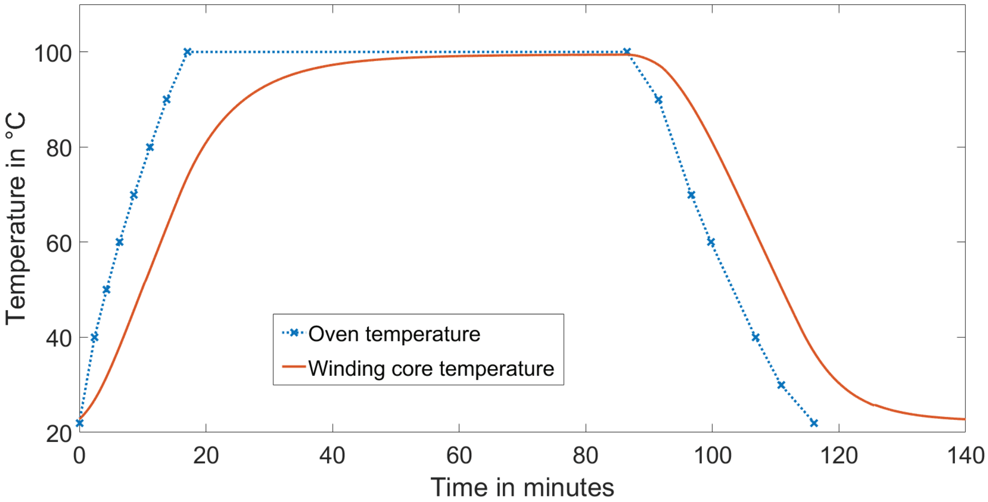

Figure 5.9: Exemplary temperature profile used for depolarization of film capacitor windings monitored with a sensor inside a prepared reference winding.

In order to examine the influence of the temperature on the depolarization of the windings, the four identical capacitor windings are first characterized and then subjected to different HV and/ or temperature treatments. The course of the compensation voltages of the temperature reference windings W1 and W2 is shown in Fig. 5.10.

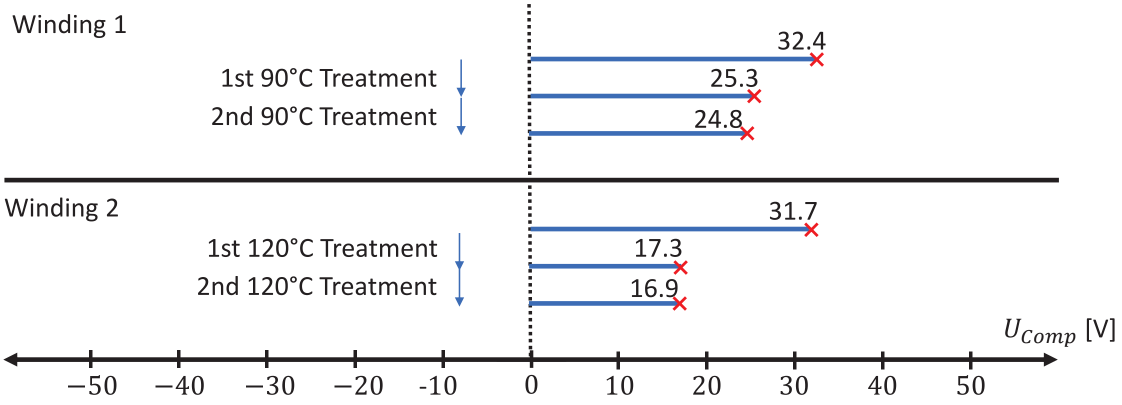

Figure 5.10: Reference Winding subjected to either temperature or HV pulses.

It can be monitored that a significant reduction of the compensation voltage is already achieved for both temperatures during the first temperature treatment. In the second application, the compensation voltage was only marginally reduced in both cases, and no significant change was measured in a repeated temperature application.

The temperatures 90 °C and 120 °C were chosen for the experiment because they are above known decomposition temperatures from thermally stimulated discharge measurements for polypropylene conducted by Weber [123]. Thus, the higher temperature of 120 °C should trigger an additional depolarization mechanism. In addition, both temperatures (as long as they occur for a short time and without electrical voltage) do not damage the capacitor under investigation.

It can be concluded from the measurements that additional discharge mechanisms are triggered at higher temperatures. A potential explanation for this is that the so-called deep charge traps can be reached at 120 °C, but at 90 °C this is not possible. Nevertheless, even 120 °C was not sufficient to achieve a complete discharge of the compensation voltage.

In the vehicle, PP-based DC-link capacitors may usually reach a maximum of 105 °C during operation. In addition to this temperature limit, a safety factor must be kept in the design, as the self-heating of aged components will continue to increase due to a higher internal resistance. It is therefore possible that the compensation voltage in the capacitor is also maintained during use in the electric vehicle.

5.2.4 Combination of temperature stimulation and high voltage conditioning

In addition to the temperature reference windings, further tests were conducted with an overlay of temperature loads and HV pulses. Therefore, the thermal cycles were varied by using 120 °C for W3 and 90°C for W4. The course of the compensation voltage exposed to HV conditioning and temperature treatment is shown in Fig. 5.11.

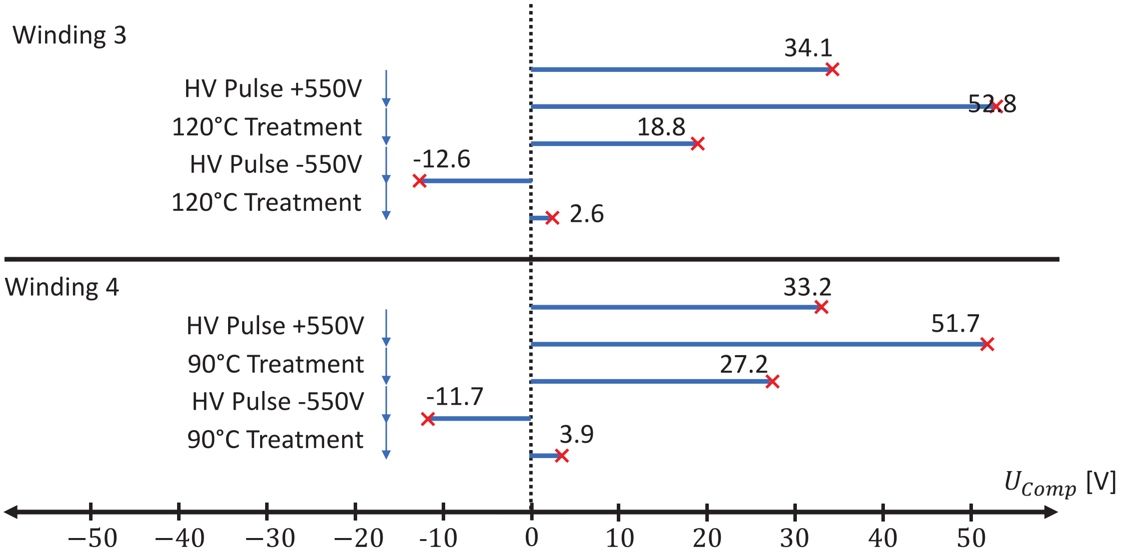

Figure 5.11: Influence of HV conditioning and temperature on compensation voltage. The impedance curves of W3 are show in the appendix in section A.4 and remain unchanged due to HV-conditioning or temperature loads.

Before the test, W3 and W4 had similar quasi-stable compensation voltages, which were induced during the self healing or the EoL test. After the HV conditioning process with a voltage pulse of +550 V, both windings still behave similar, which means that the compensation voltage is increased around 19V. Then, the temperature loads of 90 °C and 120 °C are applied, while the higher temperature leads to a higher depolarization, as expected.

At a next step, the HV conditioning process was repeated with a negative voltage pulse of -550 V. After that, both windings had a similar level of the compensation voltage while W3 had a higher negative value but a lower jump induced by the conditioning. Then, the corresponding thermal loads were applied. It can be observed that the prior negative compensation voltage is changed to a small positive polarization corresponding with a compensation voltage of 2-4 V for both windings. Surprisingly, temperature loads alone are capable of reversing the polarity of the compensation voltage. The existing preferred direction in the winding is therefore visible, which cannot be eliminated by external re-polarization.

One possible explanation for this behavior is that the initial polarization took place during production with more than 550 V, and therefore deeper charge traps were achieved. HV pulses with twice the nominal voltage, i.e. 800 V for the tested windings, are conceivable.

5.3 Origin of the compensation voltage

The purpose of this section is to investigate if an intermediate layer is present between the metallization and the dielectric, as it is proposed for food packaging materials investigated by Struller et al. [107–111]. The existence of a corresponding boundary layer would provide an explanation for the favoured direction of the polarization in the material, which cannot be eliminated by voltage pulses or temperature loads. To prove this, the metallized dielectric was examined using both a scanning electron microscope (SEM) and a transmission electron microscope (TEM).

5.3.1 SEM analysis

In scanning electron microscopy (SEM), the surface of a material sample is scanned with a focused ion beam. This scanning process causes the release of secondary electrons from the sample surface. These secondary electrons can then be captured by a detector and are used to generate a surface image of the sample. Compared to conventional light microscopes, the scanning electron microscope is characterized by a significantly higher resolution. Using a SEM, structures on the sample surface down to the nanometer scale can be examined.

The high resolution of the scanning electron microscope results from the use of electrons instead of light as the radiation source. Furthermore, the focusing of the electron beam using electromagnetic lenses enables efficient beam guidance and scanning of the sample surface.

As part of this work, a film capacitor bobbin was prepared and a pocket was cut into its surface using a focused ion beam. The resulting cross-section was then scanned with a SEM to obtain information about the layer structure. Therefore, a Zeiss Crossbeam 550 is used for the measurements in this work. This combines the technology of a SEM with the possibilities for processing samples using a focused ion beam (FIB) [128]. The resulting cross-section can be seen in Fig. 5.12. It is important to note that the inlense detector is used for the SEM images in this work. Angle-corrected images can also be used to determine layer thicknesses. The exact boundaries of the layers are difficult to identify due to similar grey values. According to the film supplier, the nominal thickness of the examined BOPP film is 2.3 ± 0.1 µm.

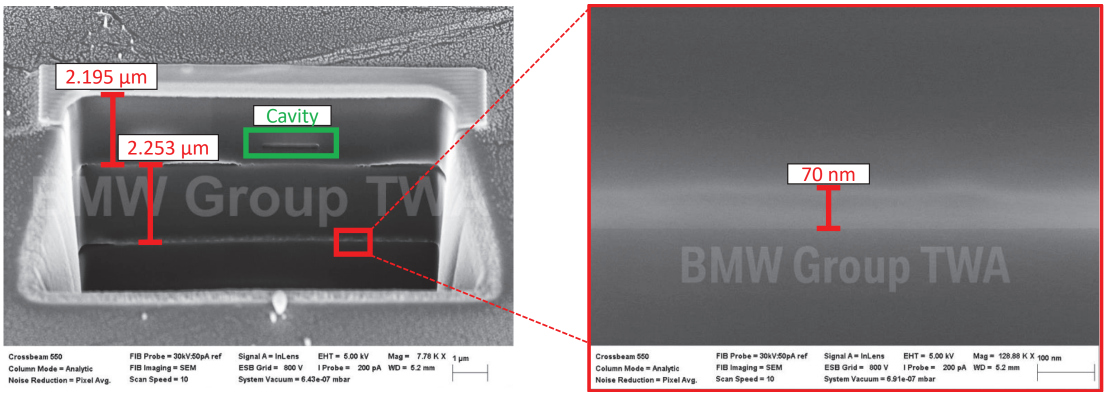

Figure 5.12: SEM analysis of a BOPP film stack. Left side: FIB probe with two metallized BOPP layers. Right side: Enlargement of metallized layer.

The individual dielectric layers can be clearly seen in the image. It is noticeable that there is delamination of the aluminium from the BOPP. However, this is probably not relevant as it most likely occurred during sample processing.

In the area of the dielectric, a cavity can be recognised, which is presumably the result of the strong stretching of the BOPP film. These cracks may represent polarizable air pockets, which favour the effect of electrostriction. However, in order to estimate the distribution and number of cavities in the film material, larger cross-sectional areas need to be investigated.

The enlarged section view of the metallic phase suggests different layers due to the different grey values in Fig. 5.12. The presumed layer system has a thickness of approximately 70 nm, but cannot be further resolved here. It must be admitted that the resolution of the SEM image is not sufficient for the identification of a suspected boundary layer. It can therefore be concluded that the SEM analysis can dissolve thicker layer systems in metallized film capacitors and defects and delaminations of the film becomes visible. However, this measuring method does not appear to be suitable for precisely analysing the layer structure of the metallization. Therefore, TEM measurements are applied and presented in the next section.

5.3.2 TEM analysis

The metallized BOPP film is examined using transmission electron microscopy (TEM) to verify the presence of the expected intermediate layer. For this purpose, a $5x5$ mm piece of film is cut out of the capacitor using an ultra short-pulsed laser. Using a focused ion beam (FIB; in our case a Zeiss crossbeam 55: Gemini II) a cut into the first layers of the film is done. This technique brings the least possible stress on the layers while simultaneously delivering a high resolution. The FIB test sections are shown in Fig. 5.13.

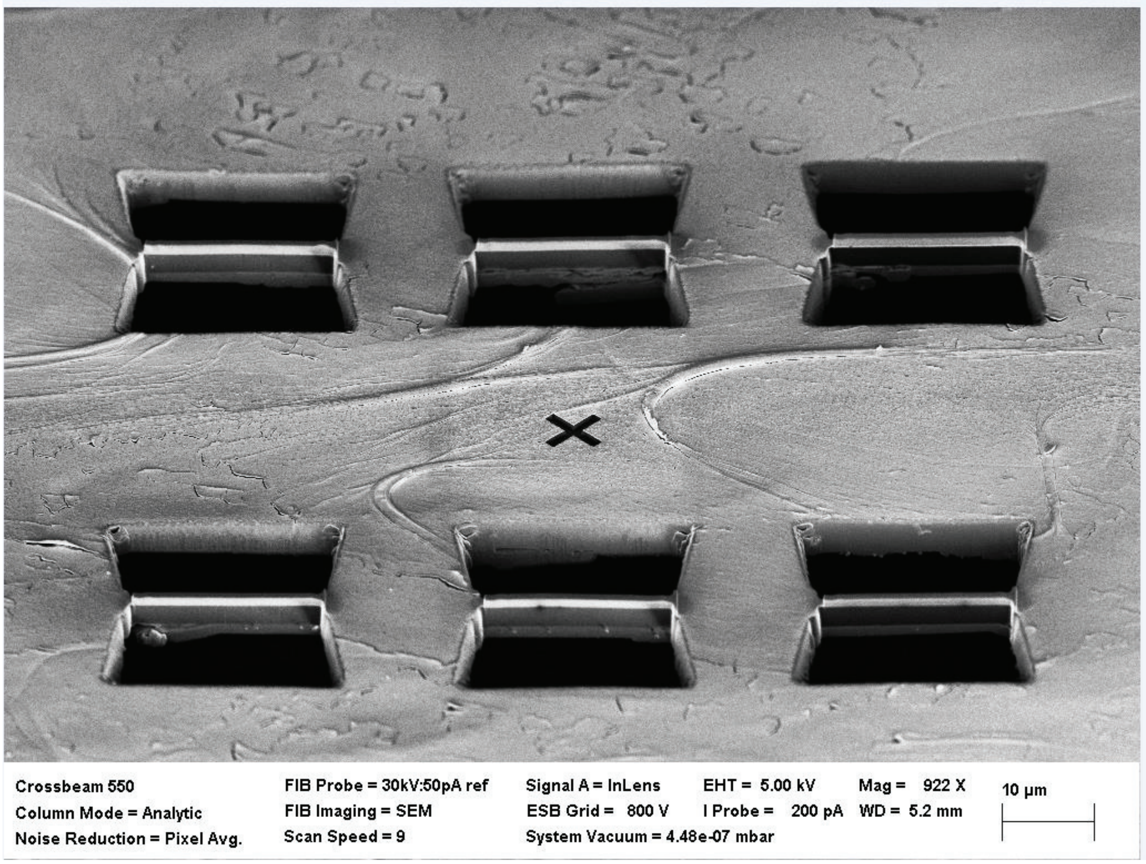

Figure 5.13: FIB cutting of metallized BOPP probe. A thin membrane remains between the cut-out ramps.

The test specimens are prepared by precision-cutting of two intersecting ramps into the film from opposing directions, leaving a narrow central bar. Given the exceptionally thin nature of the samples (on the order of only a few nanometers), the primary technical challenge lies in carefully extracting the samples from the pockets without inducing any damage.

In a next step, this narrow bar is lifted out and transilluminated with an electron beam. In this process, the electrons are reflected only by the metallic structures, allowing a further layer system to be resolved. These layers near the metallization are shown in Fig. 5.14.

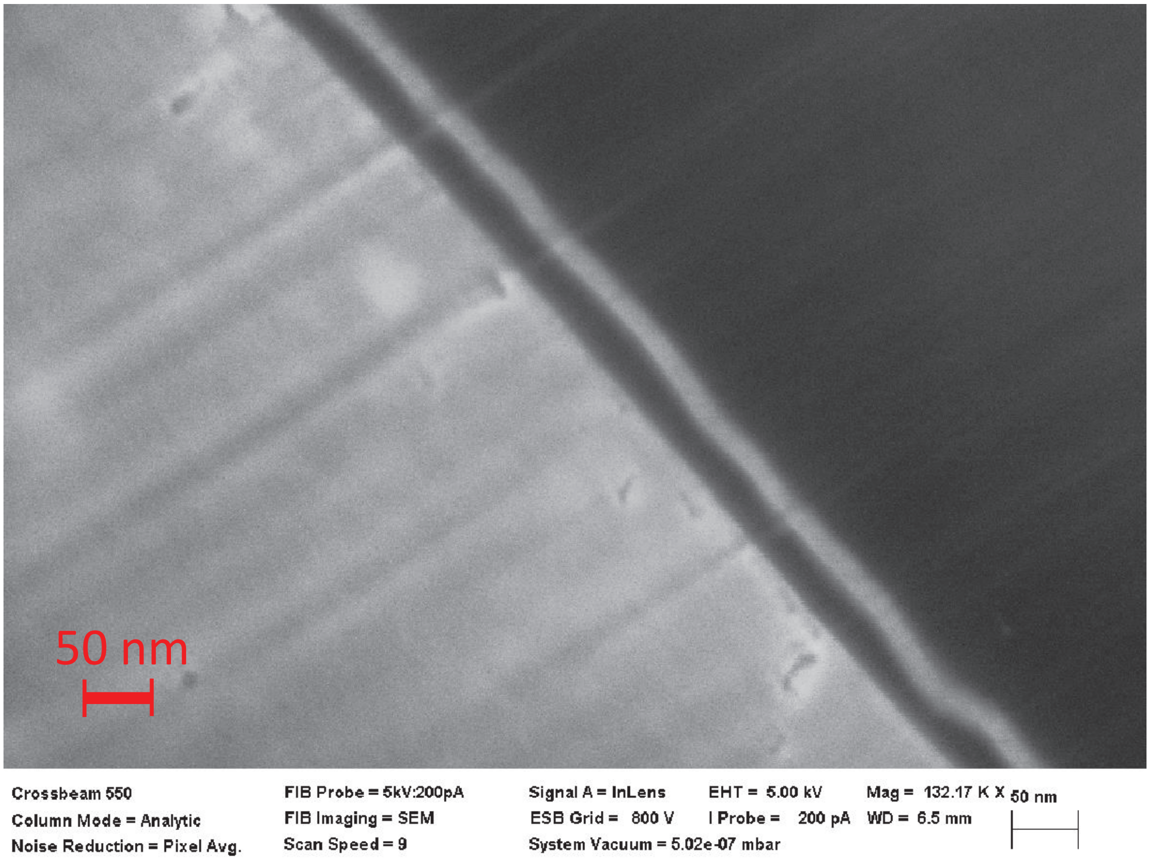

Figure 5.14: TEM shows intermediate layer between dielectric and electrode.

The TEM image clearly shows that another thin layer with a thickness of around 15 nm is visible in addition to the metallization. This additional layer could be caused by various processes within the metallization process. One possibility is that the film is chemically activated using oxygen plasma before the vapour deposition process. This can trigger the formation of an additional polar boundary layer in a similar way to food packaging applications [108]. Another possible explanation is that there has been a second vapour deposition process, for example by using an additional zinc layer. This is typically done to prevent corrosion effects on the metallization and also improves the adhesion between electrode and dielectric. The TEM image therefore allows some conclusions to be drawn about the modelling of the boundary layer. It is therefore very likely that the quasi-stationary part of the compensation voltage is caused by trapped charges in the boundary layer. This is shown in the close-up in Fig. 5.15.

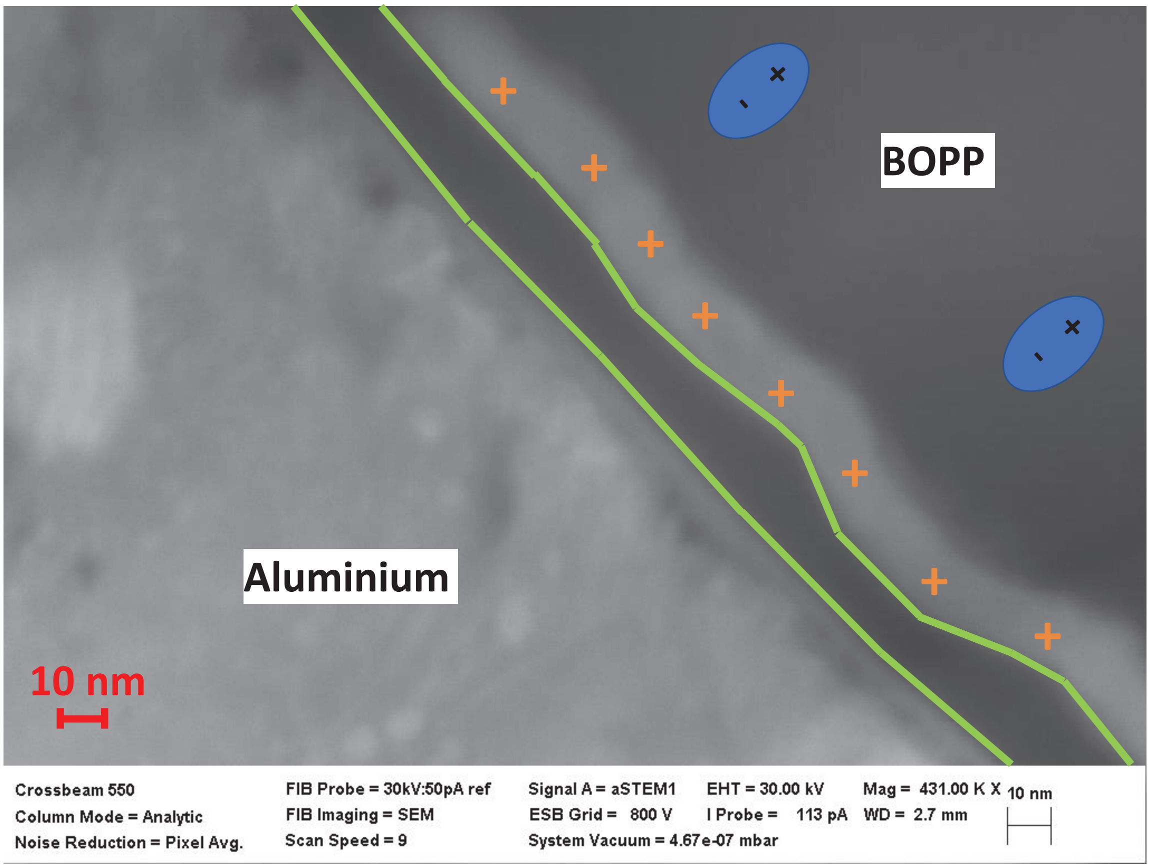

Figure 5.15: TEM shows intermediate layer between dielectric and electrode.

The compensation voltage of the examined bobbins has always been detected in the range of 35±4 V for the windings tested in their initial state (even after two years storage time). This could be explained by the thickness of the boundary layer, i.e. the 35 V may correspond approximately to the insulation capacity of 15 nm. It can therefore be assumed that a thicker additional boundary layer would also enable a higher quasi-stationary compensation voltage. This could probably be influenced by the intensity of plasma activation of the dielectric.

5.3.3 Film capacitor model including intermediate layer

The capacitor model considering the intermediate layer has been introduced in [11]. Here, the polar behaviour and the stable part of the compensation voltage are explained by the intermediate layer measured in the previous section. The model is sketched in Fig. 5.16.

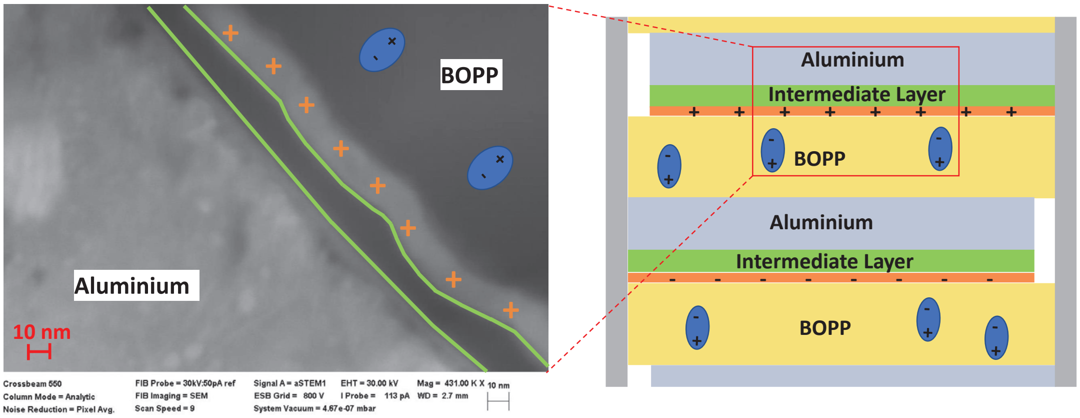

Figure 5.16: Film capacitor with intermediate layer introduced in [11].

This model explains the existence of the compensation voltage and its stable long-term value for capacitors based on BOPP. A high compensation voltage can be stored in the material, since so-called voids in BOPP act as charge traps. This voltage can be influenced externally by an applied voltage during the HV conditioning process introduced in section 5.2.1. In addition, the reduction of this voltage can be accelerated, for example by temperature cycles.

The charge traps can be reinforced, so foamed PP is used specifically in other applications. However, this alone does not explain why a quasi-stationary value is achieved or why the compensation voltage also relaxes "above 0 V" and therefore changes the polarity during the temperature discharge process presented in section 5.2.4. This behavior indicates that a preferred direction is present in the material and can be attributed to the boundary layer interface.

Essentially, in addition to the trap states, charges are also permanently separated from each other via the boundary layer. The insulating capacity of the boundary layer can be used as a stable limit. The relaxation of the trap states and that of the charges separated by the boundary layer are subject to different time constants.

5.4 Summary

In this section, the polarization effects in film capacitors based on a BOPP dielectric were studied in more detail. The measurement method used represents a new approach in which conclusions can be drawn about the polarization on the basis of the acoustic excitation. It was shown that the compensation voltage can be influenced by external voltage pulses. It is therefore possible to increase the compensation voltage of a film capacitor for electric vehicles to up to 210 V. Regarding the compensation voltage over time, high values are not stable over time. Measuring the course of the compensation voltage over one month, it became visible that it can consist of a transient and a steady state part. The transient component is subject to different depolarization mechanisms, which is why the time course of the compensation voltage must ideally be described with the aid of several exponential terms. The steady state component, on the other hand, was measured after more than two years of storage and can be compared with the long-term stability of electrets.

Thermally stimulated discharge at 90 °C and 120 °C of the capacitors was also regarded. However, the preferred direction of the compensation voltage originating from manufacturing can not be neutralized with thermal loads. Thus, after HV conditioning, it is even possible to reverse the polarity of the compensation voltage with the aid of a thermal load.

Furthermore, the structure of the dielectric was examined using a scanning electron microscope (SEM) as well as a transmission electron microscope (TEM). The corresponding measurement provided insights in the dielectric and an interface layer was found. This layer is relevant for the steady state part of the compensation voltage. The results provide a basis for the technical usability of the measured compensation voltage.

Chapter 6

Conclusion and outlook

In the last chapter, a conclusion is drawn to point out where the state of research has been further extended. For this purpose, the main results are summarized and interpreted. Furthermore, patents are listed that are related to this work. These represent a possible outlook and show for which areas of application the results obtained could be of significance. Finally, the research questions from section 2.6 are answered.

6.1 Major research findings

The main objective of the present work was to fully understand the acoustic excitations caused by DC-link capacitors within the power electronics of electric vehicles. To achieve this, a detailed excitation model was developed that considers the electromechanical couplings present within the dielectric material. Therefore, a sensor model from Thakur et al. [114, 115] was transferred to the specific properties of DC-link capacitors made of metallized BOPP films. In addition to the Coulomb forces, this model also takes into account the electrostriction, which is described by the electrostrictive parameters. This increases the deflection of the capacitors in the example of the analysed winding geometries by up to 47 percent, which could be validated by measurements based on low voltages [41].

By developing this comprehensive understanding of the acoustic excitations in DC-link capacitors, the present work also provides valuable insights for the design and optimization of power electronics in electric vehicles, where capacitor-induced noise can become a significant problem, especially when ripple voltages excite the DC-link capacitor at its resonance frequency. To ensure that film capacitors remain acoustically unobtrusive, it is crucial that the excitation frequency does not coincide with an electromechanical resonance. This can be achieved either by selecting a suitable PWM strategy, such as shifting the PWM frequency or randomizing it, or through geometric measures on the DC-link capacitor itself. Typically, more strongly pressed windings tend to have lower resonance frequencies, while rounder windings exhibit higher resonance frequencies. By tailoring the capacitor winding geometry, the resonance frequencies can be shifted away from the critical operating range, eliminating the risk of undesirable acoustic excitations.

For this reason, finite element models were applied to transfer the analytical excitation model based on a plate capacitor to the geometry of capacitor windings. Combining the electrostrictive excitation model with the FE approach, it is possible to predict the excitation amplitudes of the film capacitor windings, using the electrostrictive parameters of BOPP measured and reported in the literature [103]. The results thus obtained have already been published in Herrnberger et al. [41]. Two ways of transferring the excitation model to the FE environment are presented:

1. Application of orthotropic strains with temperature auxiliary loads.
2. Modelling the strain by selecting suitable pressure components.

It can be concluded that the model with pressure components represents an increased modelling effort due to a necessary calibration workflow. In return, it allows a more efficient calculation due to the application of modal superposition. This is particularly relevant for large composite models. Based on the presented winding geometries, the calculation time could thus be reduced to approx. ten percent of the original FE calculation time based on full matrices.

Measurements on the DC-link capacitor show that ripple voltages less than 1 V and DC voltages of up to 30 V are already sufficient to exceed the hearing threshold. As battery voltages of 400 V are typically used in real electric vehicles, sound power levels of up to 72.6 dB can be expected under worst-case conditions. This excitation is based on the fundamental oscillation, which has the main influence due to the dominant DC voltage in the application presented.

During the validation measurements, it was also established that the excitation of the capacitors in their initial state does not behave symmetrically with respect to the applied DC voltage. For this reason, the excitation model was extended to include a compensation voltage, which can occur in a stable and quasi-stationary manner, comparable to the polarization of an electret material. This effect had been documented as early as 1954 by Kuhl et al. [65] and is referred to as a compensative voltage. The principle of this compensative voltage was found to be applicable to film capacitors, indicating that these types of capacitors can exhibit electret-like properties that allow them to store polarization over extended periods of time.

Investigations of components with a two-year storage time have revealed that capacitor windings still exhibit a preferred directionality with respect to the application of an external DC voltage. This preferred polarization state of the windings can be influenced with the application of targeted high-voltage pulses, known as HV conditioning. The ability to actively manipulate this polarization state through the HV conditioning process indicates the potential for tailoring the acoustic response characteristics of the capacitor windings by controlling their internal polarization.

It can be concluded that the polarization is already given to the windings during the production process, especially during the end-of-line test, as voltages higher than the nominal voltage are applied at this step.

Since the compensation voltage affects the acoustic excitation of the windings, the polarization can be determined by varying the applied DC voltage. This is similar to the known capacitance-voltage characterisation in the field of electrostatic transducers. However, as the acoustic response of the capacitors is analysed in the measurement method presented, the approach represents a new measurement method that also applies aspects of pulsed electroacoustic analysis [7].

The acoustically characterized capacitor windings with a nominal voltage of 400 V already had a quasi-stationary compensation voltage of approx. 35±4 V, which represents a moderate prepolarization. For an optimized acoustic behaviour, the intrinsic polarization of the bobbin should therefore act against the field direction specified by the HV battery. The corresponding compensation voltage can be increased up to 210 V with a HV pulse near the breakdown voltage (typically around 1100 V at room temperature). However, this obtained compensation voltage is not stable as it decreases over time. After 27 days of further storage at room temperature, the compensation voltage had dropped from 210 V to 125 V. This decrease in the compensation voltage is similar to the behaviour of element membranes for microphones investigated by Gerlach et al. [29]. Analogous to the measurements presented there, exponential functions with several exponents are suitable for the mathematical description of the decay curve, which suggests the presence of various physical effects.

It was found that the compensation voltage can be divided into a transient and a quasi-stationary part. The transient part of the compensation voltage is most likely caused by a polarization of the cavities in the dielectric. These cavities are obtained due to the intense stretching process of the BOPP film, which causes cracks in the material. The quasi-stationary part of the compensation voltage can be attributed to the manufacturing processes of the metallization. This process is also often applied in the field of food packaging. The literatue indicates that the BOPP surface is activated prior to metallization, for example by plasma treatment. This leads to the presence of a boundary layer, which may also be present in the context of film capacitors [108–110].

In order to test this hypothesis, a capacitor winding was prepared and its cross-section consisting of a small number of metallized BOPP layers was analysed. This was initially attempted using a scanning electron microscope (SEM), but the resolution was not sufficient to detect a layer system. The boundary layer could only be detected using high-resolution transmission electron microscopy (TEM) and was found with a thickness of approx. 15 nm at a dielectric film thickness of 2.2 µm. This boundary layer is considered the primary contributor to the observed quasi-stationary compensation voltage in the observed capacitors.

If temperature loads are applied to polarized windings, the decay of the compensation voltage is accelerated. This was investigated with the aid of a simple experiment in which the windings were acoustically characterized before and after an oven treatment. It can be concluded that the maximum peak temperature in particular has an influence on the discharge, so that repeated temperature treatment results in only a minor drop in the compensation voltage. This matches with the fact, that a specific temperature is connected to a peak in the depolarization, similar to measurements of thermally stimulated discharge (TSD) [119, 120]. It should be mentioned that the discharge temperatures of 90 °C and 120 °C investigated in this work were not able to neutralise the initial preferred direction of the windings. For example, windings that were polarized shortly beforehand with a voltage pulse against their preferred direction were observed to change their polarity as a result of temperature loads. The observed behavior is most likely related to the detected boundary layer mentioned previously. This boundary layer represents deeper charge traps within the dielectric material, which are only likely to relax at higher temperatures. However, exposing the dielectric to temperatures higher than 120 °C would result in permanent damage, as the material would not be able to maintain the required dielectric strength under those conditions.

6.2 Outlook and possible technical usability of the research findings

In the course of this work, several patent applications have been developed and thus represent potential use cases for the new findings. The patent drafts are published, for detailed descriptions it can be referred to Refs. [8–10, 35–39, 43]. In the following, the patents will be summarized shortly to showcase potential applications in the field of film capacitors.

Since the compensation voltage affects the acoustics, it can also be used specifically to improve the electromechanical properties of capacitors. For this reason, a method of generating a pre-polarization in the capacitor is described. It must be ensured that the capacitor windings are installed "the right way round" in the capacitor in order to take advantage of the preferential direction created by the metallization. In this way, it is possible to reduce the acoustic excitation of the capacitor due to the pre-polarization [8, 38, 39].

As described in chapter 4, the electromechanical resonant frequencies of DC-link capacitors depend on both the winding geometry and the surrounding structure. As a result, copper busbars can provide local stiffening and increase the resonant frequency. This concept can be used to resonate several windings at different frequencies. This will reduce the maximum possible amplitude, especially with PWM control methods with variable carrier frequency and could be a potential solution for solving acoustic problems inside an automotive film capacitor [37].

Another possible application is based on the long-term stability of the compensation voltage. It is thus conceivable to use the electret properties of BOPP films as a data and information storage system. Initial experiments on this have already been carried out with the aid of an atomic force microscope, but were not investigated further within the scope of this work due to time constraints. For example, it is possible to impose a quasi-stationary electric field in a charge section by a voltage pulse and thus encode an information. The deformation of this charge carrier section is then dependent on the stored electrical field. As a next step, a deformation of this section can be measured, for example with the measuring tip of an atomic force microscope. Reference is made to the principle measurement carried out in the context of this work in the appendix in section A.5 [10].

Another approach to compensate the acoustic emissions of a capacitor element is the utilization of piezoelectric materials. One potential configuration involves integrating a thin piezoelectric layer underneath the capacitor or between the metallized layers. This piezoelectric layer would then also be subjected to the voltage fluctuations experienced by the capacitor, allowing it to generate a counteracting acoustic response. The piezoelectric layer must be designed in a way that it compensates for the expansion of the actual capacitor. This setup will admittedly be relatively complex, but could be a potential solution in very vibration-sensitive environments [36].

Since capacitors heat up during operation, a temperature effect was also found during measurements in the course of this work. This could be related to the fact that the damping of some materials changes significantly with temperature. This effect can be used in particular when the glass transition temperature T_g is reached. In this case, the damping of the material increases abruptly, reducing the resulting amplitude. One example is the use of polyamide as a dielectric, which has a glass transition temperature of approx. 55 °C. The invention can be used for capacitors with a constant operating temperature [9].

Another possible application is to measure the compensation voltage during production using the method described in this work. Typically, end-of-line tests already exist in the production of capacitor windings, so the extension of an acoustic measurement is not costly. Ultimately, it is possible to measure which polarization a defined voltage pulse causes in a capacitor winding. The polarizability can be used as a monitoring criterion to guarantee consistent film quality. In general, a higher polarizability is likely to be associated with a higher number of voids and inclusions within the dielectric [43].

Having shown in the course of this work that ripple currents excite the capacitor in the electric drive of a vehicle, this excitation can also be used in reverse as monitoring for these currents. This applies in particular to separately excited synchronous machines, where a current sensor has to be installed to measure the rotor current. However, if the semiconductor associated with the exciter has a different carrier frequency than the other semiconductors, the oscillation of the capacitor can be evaluated (e.g. with the aid of an acceleration sensor). This allows to draw conclusions on the rotor current, since it should be proportional to the capacitor excitation. This would make it possible to save an additional current sensor for the exciter path [35].

6.3 Extension of the state of research

In conclusion, the five research questions from section 2.6 of this work can be answered. Accordingly, the answers to these research questions represent five key findings that expand the state of research for the acoustic excitation of DC-link capacitors.

I) The presented sensor model has been successfully adapted and applied to film capacitors. It has been demonstrated that electrostriction is a relevant factor, and its consideration is essential for accurately predicting the excitation amplitude.

II) The model, which is valid on the basis of a plate capacitor, can be transferred to winding geometries with the aid of FE simulations. The geometry of the individual winding influences the location of the resonance and can thus also be used to shift resonances outside the critical frequency range.

III) For the acoustic spectral analysis of DC-link capacitors, the windings can be simulated using both a substitute temperature model and an equivalent pressure model. Both excitation models provide a good agreement, with MAC values exceeding 0.95. Furthermore, the pressure model can also be employed for modal superposition, enabling the simulation at the inverter level while maintaining manageable computational resources.

IV) The polarization effects influence the acoustic excitation of the BOPP film capacitors. These polarization effects can change over time and can be influenced by temperature loads.

V) After extended periods of operation, the capacitors exhibit persistent polarization, establishing parallels to the behavior of electret materials. This persistent polarization has been attributed to the presence of a boundary layer within the dielectric, which was detected through high-resolution transmission electron microscopy (TEM) analysis.

An additional extension is the measurement method for polarized windings. In this context, the acoustic characterization of the compensation voltage can be seen as a simpler version of a thermally stimulated discharge (TSD) measurement. By evaluating the acoustic excitation of the capacitor winding, it is possible to quantify the depolarization of the winding.

The connection between film capacitors and electret properties is also a new discovery. In conclusion, it can be said that a capacitor winding has similarities to an electret loudspeaker. The pre-polarization makes it possible to influence the acoustic excitation amplitude. Ideally, the stored polarization should be utilized to achieve a more quiet capacitor operation.

Appendix A

Appendix

A.1 Wedge vaporization of film capacitor windings

Many capacitor manufacturers adjust the metallization thickness to the required current carrying capacity. For example, more material is usually used in the Schoop layer area. This must be taken into account when producing TEM samples and an area of homogeneous metallization thickness should be selected.

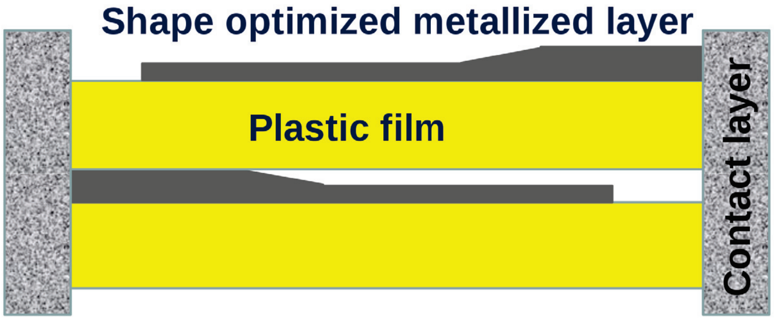

Figure A.1: To optimize the current carrying capacity, the metallization thickness can be varied via the socket height [14].

A.2 Modelling of the capacitor impedance for voltage calculation

To derive the voltage excitation at the DC-link, a simple model was created in LT-Spice. The assumption is made that the supply line only contributes inductance and the capacitor only capacitance to the system. Since the impedance curves from measurement and simulation agree well, this assumption can be considered valid.

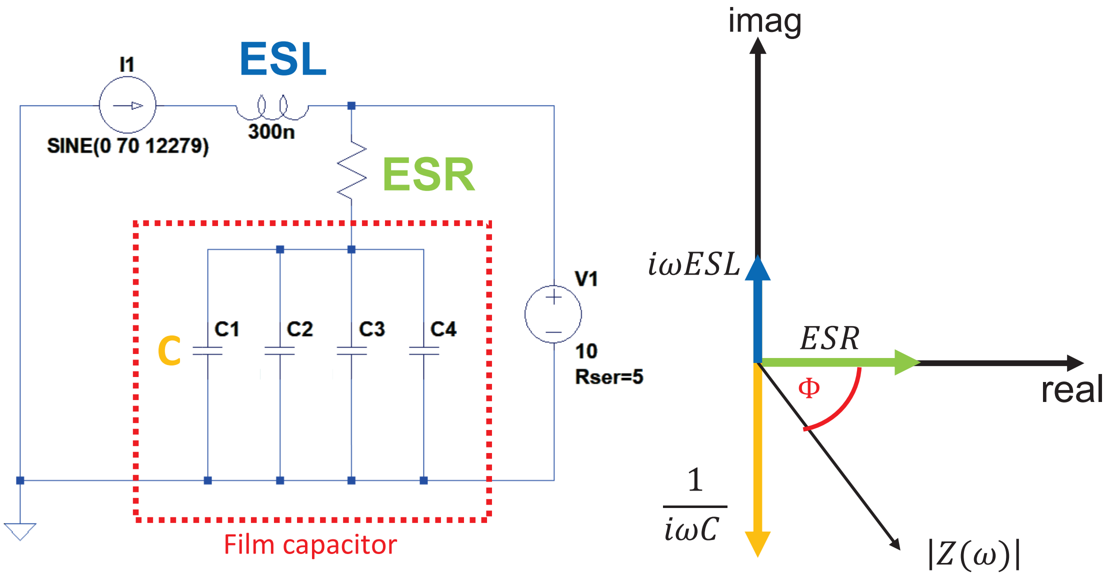

Figure A.2: Electrical model of the measurement setup (l) and space vector representation of the electrical impedance (r).

A.3 DMTA measurements of epoxy material

For the simulation of DC-link capacitors, the material parameters of the epoxy were determined by dynamic mechanical thermal analysis (DMTA) measurements. These measurements were provided by Moritz Hülsebrock in cooperation with the Technical University Darmstadt. No particular frequency dependence was found, which means that constant material parameters can be assumed. Thus, the simulation on capacitor assembly level is simplified by modal superposition.

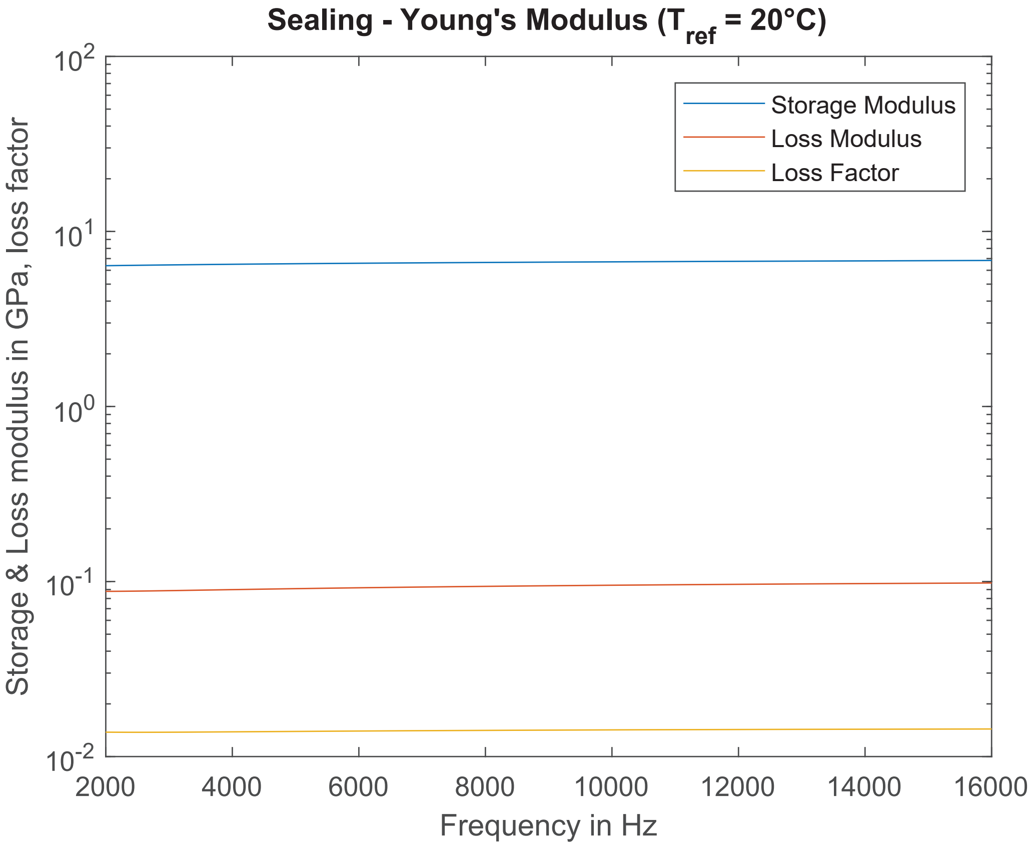

Figure A.3: DMTA measurement of epoxy resin.

A.4 Impedance curves

The impedance curves of the bobbins were measured after each test. No changes were detected. The changes in the acoustic excitation are therefore not due to damage to the bobbins.

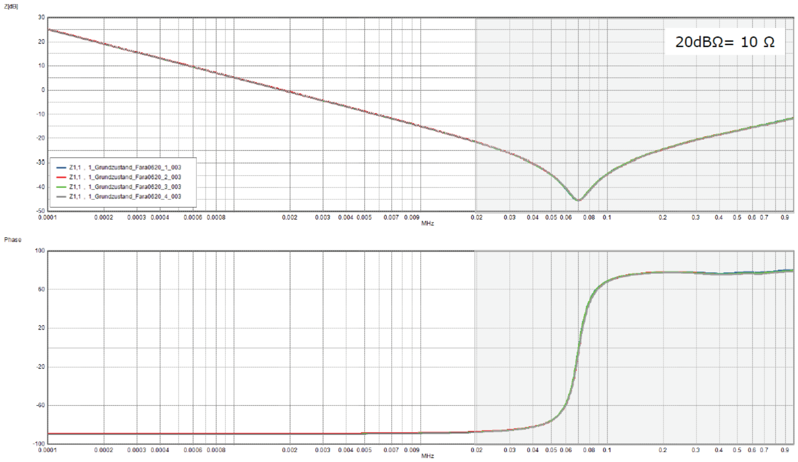

Figure A.4: Initial state of the capacitor windings.

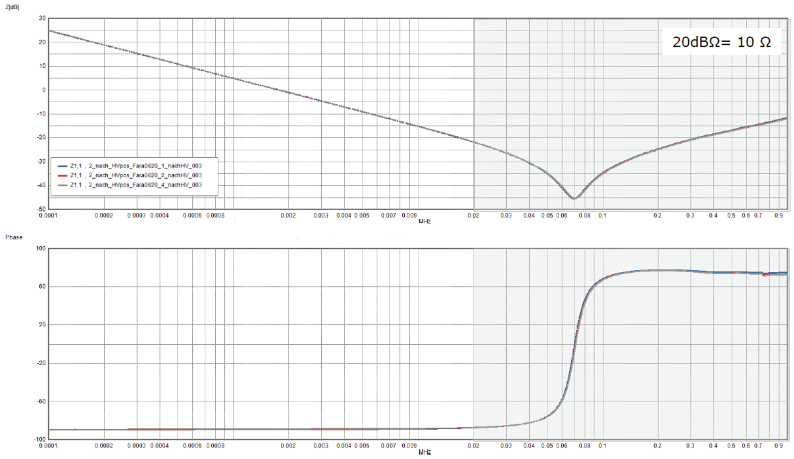

Figure A.5: Network analysis after positive voltage pulse test.

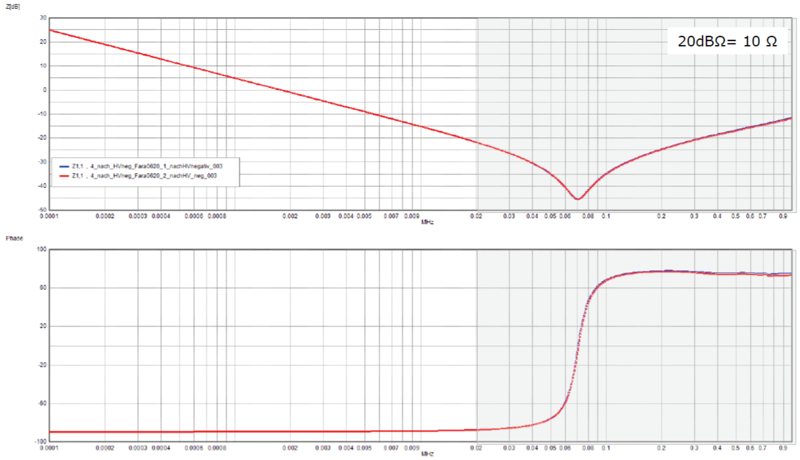

Figure A.6: Network analysis after negative voltage pulse test.

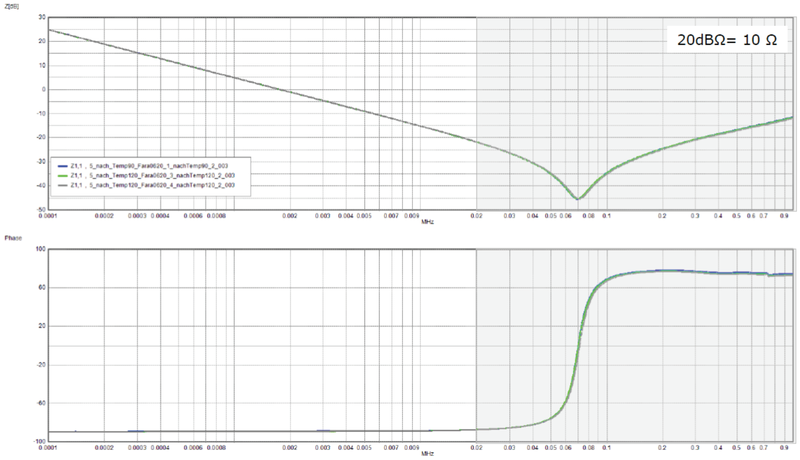

Figure A.7: Network analysis after temperature test at 120 °C.

A.5 Atomic force microscopy of capacitor bobbins under excitation

In this work, the deformation of a capacitor winding was measured using an atomic force microscope (AFM). Therefore, only the DC voltage is present, which leads to a stationary deformation as long as the voltage is applied. Since the surface of the winding already has a higher roughness than the expected deformation, a flat glass plate was glued on the bobbin for the measurement. The corresponding measurement setup is shown in Fig. A.8.

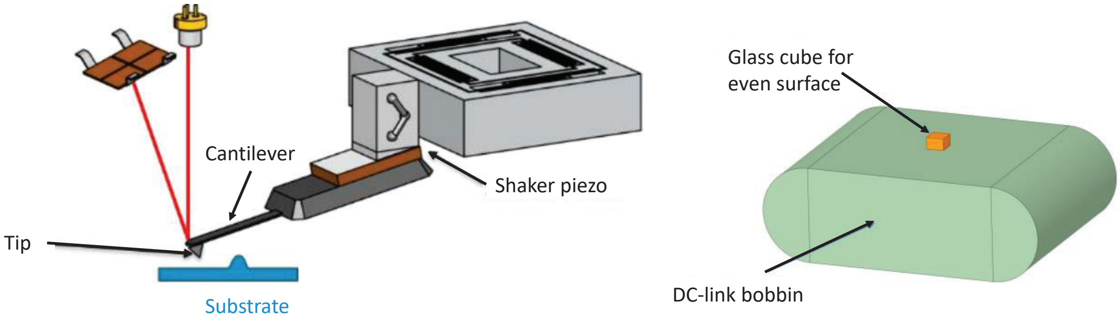

Figure A.8: Measurement setup of AFM (Nanosurf) [84].

The glass plate with a thickness of approx. 5 mm provides additional decoupling so that the influence of the capacitor on the cantilever is reduced. Nevertheless, this is only a principle experiment and no reliable quantitative statements are to be made. The course of the deflection at the AFM during charging and discharging of a capacitor is shown in Fig. A.9. The asymmetric deflection with a capacitor charge of + 10 V or - 10 V suggests the effect of the compensation voltage. In addition, the compensation voltage can be roughly estimated from the recorded measurement curve. For this purpose, the drift effects are estimated with a gusset adjustment. The following applies for the displacement of the bobbin δh:

$$\delta h \propto (U_{DC} + U_{komp})^2 \tag{A.1}$$

$$\frac{187nm}{65nm} = \frac{(U_{DC} + U_{komp})^2}{(U_{DC} - U_{komp})^2} \tag{A.2}$$

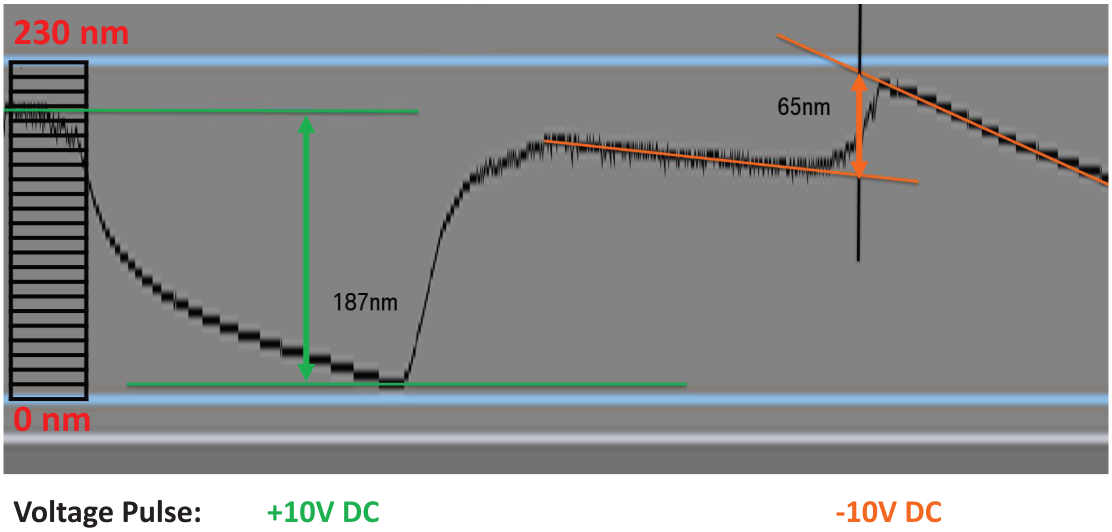

Figure A.9: Deformation analysis of AFM measurements during charging and discharging process of a DC-link bobbin with initial polarization.

This would result in a compensation voltage of 38.2 V, which is also in the range of the values determined with acoustic measurements. Thus, it would be possible to determine with the help of the evaluation of the amplitude whether there is a polarization stored in the material, which according to the published patent could represent the physical basis of a data memory [10].

Curriculum vitae

Maximilian Herrnberger *30.08.1992 in Munich

- 2015: Bachelor degree in engineering science at the Technical University Munich
- 2018: Master degree in automotive engineering with a focus on electric powertrains at the Technical University Munich.
- Master thesis in NVH related topic using transfer path analysis for a vehicle chassis
- 2018 - 2021: PhD- candidate at the BMW AG in cooperation with the Technical University Darmstadt.
- Since 2021: Mechanical engineer for DC-link capacitors at the BMW AG.
- Research interests: Power electronics, acoustics, film capacitors, numerical simulation, dielectric materials

Publication List

First Authorship

- Simulation Process for the Acoustical Excitation of DC-Link Film Capacitors in Highly Integrated Electrical Drivetrains. SAE International Journal of Advances and Current Practices in Mobility 3.2020-01-1500 (2020): 1030-1037. DOI: https://doi.org/10.4271/2020-01-1500 [41]
- Akustische Anregungsquellen in hochintegrierten Leistungselektroniken mobiler Antriebe. Daga 2019 [40]
- Transferpfadanalyse auf Basis der Vierpolmethode bei Mehrquellenanregung in der Fahrzeugakustik. Daga 2018 [42]
- Patents related to film capacitors [8–10, 35–39, 43]

Co-Authorship

- An electrostrictive model for polypropylene capacitors including intermediate layer polarization. IEEE Transactions on Dielectrics and Electrical Insulation 27.4 (2020): 1348-1353. DOI: 10.1109/TDEI.2020.008878 [11]
- Damage detection of joining technologies for printed controller boards in automobiles. EURODYN 2020. DOI: 10.47964/1120.9293.19578 [47]
- Stochastic identification of parametric reduced order models of printed circuit boards, ISMA 2020 [48]

Supervised student works

This is a chronological list of supervised students who have supported me with their theses:

- Jakob Bonart: Acoustic spectral analysis of inverter structures under consideration of multiphysical effects, Universität Augsburg, 2019.
- Patrick Eifert: Simulative design of vibro-acoustic decoupling for power electronics in highly integrated electric drives, RWTH Aachen, 2019.
- Thymothy Naacke: Untersuchung elektromechanischer Einflüsse von polaren Grenzschichten in Folienkondensatoren für die Leistungselektronik elektrischer Antriebe, Universität Augsburg, 2020.
- Felix Wolf: Acoustic spectral analysis of DC-link capacitors in the power electronics of electric drives, HS München, 2021.

Bibliography

[1] Adams, C. ; Schaal, C. ; Bös, J. ; Melz, T.: Numerical investigation of the sound power and of the structural intensity of a permanent magnet synchronous machine. In: *INTER-NOISE and NOISE-CON Congress and Conference Proceedings* Bd. 250 Institute of Noise Control Engineering, 2015, S. 3840–3851

[2] AKG Acoustics GmbH: *Datasheet; High-performance instrumental microphone.* `https://www.akg.com/on/demandware.static/-/Sites-masterCatalog_Harman/default/dw8e27e578/pdfs/AKG_P170_Cutsheet.pdf`. – Latest access on: 05.06.2024

[3] Albers, A. ; Fischer, J. ; Behrendt, M. ; Lieske, D.: Measurement and Interpretation of the Transfer Path of an Acoustic Phenomenon in the Drivetrain of an Electric Vehicle. In: *ATZ worldwide* 116 (2014), Nr. 3, S. 48–55

[4] Barshaw, E. J. ; White, J. ; Chait, M. J. ; Cornette, J. B. ; Bustamante, J. ; Folli, F. ; Biltchick, D. ; Borelli, G. ; Picci, G. ; Rabuffi, M.: High energy density (HED) biaxially-oriented poly-propylene (BOPP) capacitors for pulse power applications. In: *IEEE transactions on magnetics* 43 (2006), Nr. 1, S. 223–225

[5] Belko, V.O. ; Emelyanov, O.A.: Self-healing in segmented metallized film capacitors: Experimental and theoretical investigations for engineering design. In: *Journal of Applied Physics* 119 (2016), Nr. 2, S. 024509

[6] BMW Group: *BMW Gen5 Antriebstrang für BMW iX (11/2020)*, 2020. `https://www.press.bmwgroup.com/deutschland/photo/detail/P90407669/BMW-Gen5-Antriebstrang-fuer-BMW-iX-11-2020`. – Latest access on: 13.03.2023

[7] Bodega, R. ; Morshuis, P. H. F. ; Smit, J. J.: Space charge measurements on multi-dielectrics by means of the pulsed electroacoustic method. In: *IEEE transactions on dielectrics and electrical insulation* 13 (2006), Nr. 2, S. 272–281

[8] Bonart, J. ; Herrnberger, M.: *Verfahren zur vorgegebenen Polarisierung eines Kondensators sowie Kondensator mit vorgegebener isolierter Polarisierung.* Patent published on 07.01.2021. – DE102019118190A1

[9] Bonart, J. ; Herrnberger, M.: *Kondensatorsystem mit einem Dämpfungsmaterial mit vorgegebener Dämpfung und Verfahren zur Herstellung eines solchen Kondensatorsystems.* Patent published on 11.02.2021. – DE102019121530A1

[10] Bonart, J. ; Herrnberger, M.: *Informationsspeicher und Verfahren zum Programmieren und Auslesen von Informationen.* Patent published on 30.09.2021. – DE102020108366A1

[11] Bonart, J. ; Herrnberger, M. ; Hulsebrock, M. ; Lichtinger, R.: An electrostrictive model for polypropylene capacitors including intermediate layer polarization. In: *IEEE Transactions on Dielectrics and Electrical Insulation* 27 (2020), S. 1348–1353

[12] Bösing, M. ; Doncker, R. W.: Acoustic modeling of electrical drives: noise and vibration synthesis based on force response superposition / Lehrstuhl und Institut für Stromrichtertechnik und Elektrische Antriebe. 2014. – Forschungsbericht

[13] Both, E.: *Film capacitor manufactoring process.* `https://upload.wikimedia.org/wikipedia/commons/1/13/Film_cap-manufacturing.png`. Version: 2012. – Latest access on: 18.06.2023

[14] Both, E.: *Film capacitor wedge profile.* `https://upload.wikimedia.org/wikipedia/commons/thumb/7/7a/Shape_optimised_electrode.svg/1920px-Shape_optimised_electrode.svg.png`. Version: 2012. – Latest access on: 18.06.2023

[15] Böttcher, C. J. F. ; Belle, O. C. ; Bordewijk, P. ; Rip, A. ; Yue, D. D.: Theory of electric polarization. In: *Journal of The Electrochemical Society* 121 (1974), Nr. 6, S. 211Ca

[16] Bouayed, K. ; Mebarek, L. ; Lanfranchi, V. ; Chazot, J.-D. ; Marechal, R. ; Hamdi, M.-A.: Noise and vibration of a power transformer under an electrical excitation. In: *Applied Acoustics* 128 (2017), S. 64–70

[17] Brueckner Maschinenbau: *Simultaneous and Sequential BOPP UHB Films with improved Gas Barrier.* `https://www.brueckner-maschinenbau.com/downloaddata?id=djlWUERhK2Z0S1hQdElySUp4MFpRUT09`. – Latest access on: 05.07.2024

[18] Chen, G. ; Li, Y. ; Xiao, H. ; Zhu, X.: A micro-oscillation-driven energy harvester based on a flexible bipolar electret membrane with high output power. In: *Journal of Materials Chemistry A* 5 (2017), Nr. 8, S. 4150–4155

[19] Chen, G. ; Xu, Y ; Chen ; Xiao, H: A charging method for electrets based on interfacial polarization. In: *IEEE Transactions on Dielectrics and Electrical Insulation* 25 (2018), Nr. 3, S. 797–802

[20] Chen, X. ; Tseng, J.-K. ; Treufeld, I. ; Mackey, M. ; Schuele, D. E. ; Li, R. ; Fukuto, M. ; Baer, E. ; Zhu, L.: Enhanced dielectric properties due to space charge-induced interfacial polarization in multilayer polymer films. In: *Journal of Materials Chemistry C* 5 (2017), Nr. 39, S. 10417–10426

[21] Curie, J. ; Curie, P.: Développement par compression de l'électricité polaire dans les cristaux hémièdres à faces inclinées. In: *Bulletin de minéralogie* 3 (1880), Nr. 4, S. 90–93

[22] DeMeuse, M.T.: Academic investigations of biaxially stretched films. In: *Biaxial Stretching of Film*. Elsevier, 2011, S. 117–124

[23] Deutsche Gesellschaft für Akustik: *Akustische Wellen und Felder: DEGA-Empfehlung 101*. `https://www.dega-akustik.de/fileadmin/dega-akustik.de/publikationen/DEGA_Empfehlung_101.pdf`. Version: 2006. – Latest access on: 11.06.2023

[24] Dong, Q. ; Liu, X. ; Qi, H. ; Sun, C. ; Wang, Y.: Analysis and evaluation of electromagnetic vibration and noise in permanent magnet synchronous motor with rotor step skewing. In: *Science China Technological Sciences* 62 (2019), S. 839–848

[25] Dong, Q. ; Liu, Xi. ; Qi, H. ; Zhou, Y.: Vibro-acoustic prediction and evaluation of permanent magnet synchronous motors. In: *Proceedings of the Institution of Mechanical Engineers, Part D: Journal of Automobile Engineering* 234 (2020), Nr. 12, S. 2783–2793

[26] Drude, P. ; Nernst, W.: Über Elektrostriktion durch freie Ionen. In: *Zeitschrift für physikalische Chemie* 15 (1894), Nr. 1, S. 79–85

[27] Fothergill, J. C.: Electrical properties. In: *Dielectric polymer nanocomposites* (2010), S. 197–228

[28] Genuit, K.: Particular importance of psychoacoustics for sound design of quiet vehicles. In: *INTER-NOISE and NOISE-CON Congress and Conference Proceedings* Bd. 2011 Institute of Noise Control Engineering, 2011, S. 2908–2914

[29] Gerlach, A. ; Liebler, M. ; Sessler, G. M. ; Seggern, H. von ; Scheufele, B. ; Hirth, E.: Comparative analysis of isothermal decay of the surface potential of fluoroethylenepropylene electrets and of the sensitivity of electret microphones at elevated temperature. In: *AIP Advances* 10 (2020), Nr. 9, S. 095313

[30] Gieras, J. F.: *Permanent magnet motor technology: design and applications. 3rd edition.* CRC press, 2009

[31] Gnonhoue, O. G. ; Velazquez-Salazar, A. ; David, E. ; Preda, I.: Review of technologies and materials used in high-voltage film capacitors. In: *Polymers* 13 (2021), Nr. 5, S. 766

[32] Götz, K. ; Sunderer, G. ; Birzle-Harder, Deffner J. B. ; Berlin, B.: Attraktivität und Akzeptanz von Elektroautos. In: *Frankfurt am Main: ISOE-Institut für sozial-ökologische Forschung* (2011)

[33] Griffiths, D. J.: *Introduction to electrodynamics. 4th edition.* Cambridge University Press, 2021

[34] Harris, S. L.: Dynamic loads on the teeth of spur gears. In: *Proceedings of the Institution of Mechanical Engineers* 172 (1958), Nr. 1, S. 87–112

[35] Herrnberger, M.: *Verfahren zum Bestimmen zumindest eines einer elektrischen Maschine zugeführten Stroms mittels eines Rückkopplungssignals, Antriebssystem sowie Kraftfahrzeug.* Patent published on 01.12.2022. – DE102021113964A1

[36] Herrnberger, M. ; Bonart, J.: *Kondensatorsystem zur Kompensation vom mechanischen Störungen.* Patent published on 09.03.2020. – DE102019122756B3

[37] Herrnberger, M. ; Bonart, J. ; Ehrenreich, S. ; Hamerski, R.: *Kondensatorsystem mit vorgegeben steif gelagerten Kondensatoren und elektrische Schaltung mit einem Kondensatorsystem.* Patent published on 07.01.2021. – DE102019117784A1

[38] Herrnberger, M. ; Bonart, J. ; Hamerski, R. ; Ehrenreich, S. ; Haas Rugel, E.: *Verfahren zur Herstellung eines polarisierten Kondensators, polarisierter Kondensator und Verfahren zum Ermitteln einer Polarisierung eines Kondensators.* Patent published on 27.05.2021. – DE102019132143A1

[39] Herrnberger, M. ; Ehrenreich, S. ; Hamerski, R. ; M., Helferich ; Haas Rugel, E. ; Lichtinger, R. ; Bonart, J.: *Verfahren zur Herstellung eines polarisierten Kondensators und Verfahren zur Polarisierung eines Kondensators.* Patent published on 12.09.2021. – DE102020114682A1

[40] Herrnberger, M. ; Huelsebrock, M.: Akustische Anregungsquellen in hochintegrierten Leistungselektroniken mobiler Antriebe. In: *DAGA 2019: 45 Jahrestagung für Akustik*, 2019

[41] Herrnberger, M. ; Hülsebrock, M. ; Bonart, J. ; Lichtinger, R. ; Atzrodt, H. ; Pohn, J.: Simulation Process for the Acoustical Excitation of DC-Link Film Capacitors in Highly Integrated Electrical Drivetrains. In: *SAE International Journal of Advances and Current Practices in Mobility* 3 (2020), Nr. 2020-01-1500, S. 1030–1037

[42] Herrnberger, M. ; Moheit, L. ; Wagner, P. ; Lohmann, T.: Transferpfadanalyse auf Basis der Vierpolmethode bei Mehrquellenanregung in der Fahrzeugakustik. In: *Fortschritte der Akustik-DAGA 2018: 44. Jahrestagung für Akustik, 19. bis 22. März 2018 in München*, 2018

[43] Herrnberger, M. ; Naacke, T.: *Verfahren und Vorrichtung zur Analyse mechanischer Emissionen eines kapazitiven Bauteils*. Patent published on 28.07.2022. – DE102021101728A1

[44] Hill, R. M. ; Dissado, L. A.: Relaxation in elastic and viscoelastic materials. In: *Journal of Materials Science* 19 (1984), S. 1576–1595

[45] Hill, R. M. ; Dissado, L. A.: Debye and non-Debye relaxation. In: *J. Phys. C: Solid State Phy.* 18 (1985), S. 3829–3836

[46] Huang, G. ; Wei, H. ; Li, Z.: Noise Prediction for Power Capacitor Stacks Based on Whole-Condition Multiharmonic-Frequency Loaded Circuit Environment. In: *Ekoloji* 28 (2019), Nr. 107, S. 4803–4808

[47] Hülsebrock, M. ; Herrnberger, M. ; Atzrodt, H. ; Lichtinger, R.: Damage Detection of Joining Technologies for printed controller boards in automobiles. In: *EURODYN 2020, XI International Conference of Structural Dynamics, 2020.* ICMES, 2020

[48] Hülsebrock, M. ; Herrnberger, M. ; Atzrodt, H. ; Lichtinger, R.: Stochastic identification of parametric reduced order models of printed circuit boards. In: *ISMA* (2020)

[49] Hülsebrock, M.: *Methode zur parametrischen globalen Modellordnungsreduktion für eine effiziente Validierung dynamischer Systeme*, Technische Universität Darmstadt, PhD thesis, 2023. `http://tuprints.ulb.tu-darmstadt.de/22844`

[50] Ibrahim, I. ; Mohammadi, M.H. ; Ghorbanian, V. ; Lowther, D. A.: Effect of pulsewidth modulation on electromagnetic noise of interior permanent magnet synchronous motor drives. In: *IEEE Transactions on Magnetics* 55 (2019), Nr. 10, S. 1–5

[51] Ieda, M.: Electrical conduction and carrier traps in polymeric materials. In: *IEEE transactions on electrical insulation* (1984), Nr. 3, S. 162–178

[52] Imburgia, A. ; Miceli, R. ; Sanseverino, E. R. ; Romano, P. ; Viola, F.: Review of space charge measurement systems: Acoustic, thermal and optical methods. In: *IEEE Transactions on Dielectrics and Electrical Insulation* 23 (2016), Nr. 5, S. 3126–3142

[53] Jackson, J. D.: *Classical electrodynamics*. John Wiley & Sons, 2021

[54] Jadeja, R. ; Ved, A. D. ; Chauhan, S. K. ; Trivedi, T.: A random carrier frequency PWM technique with a narrowband for a grid-connected solar inverter. In: *Electrical Engineering* 102 (2020), Nr. 3, S. 1755–1767

[55] Jeschke, S. ; Loos, J. ; Kleinen, M.: Impact of highly efficient power electronics on the EMC in electric vehicles with autonomous driving functions. In: *AmE 2020-Automotive meets Electronics; 11th GMM-Symposium* VDE, 2020, S. 1–4

[56] Jonscher, A. K.: The universal dielectric response. In: *Nature* 267 (1977), S. 673–679

[57] Jonscher, A. K.: The universal dielectric response: Part I. In: *IEEE Electrical Insulation Magazine* 6 (1990), Nr. 2, S. 16–22

[58] Jonscher, A. K.: The universal dielectric response and its physical significance. In: *IEEE Transactions on Electrical Insulation* 27 (1992), Nr. 3, S. 407–423

[59] Jonscher, A. K.: Dielectric relaxation in solids. In: *J. Phys. D: Appl. Phys.* 32 (1999), S. 57–70

[60] Juraschek, S. ; Buchner, A. ; Schinnerl, B.: The electric powertrain technology of the BMW Group. In: *39th International Vienna Motor Symposium*, 2018

[61] Kahraman, A. ; Singh, R.: Non-linear dynamics of a spur gear pair. In: *Journal of sound and vibration* 142 (1990), Nr. 1, S. 49–75

[62] Kalapat, N. ; Amornsakchai, T.: Surface modification of biaxially oriented polypropylene (BOPP) film using acrylic acid-corona treatment: Part I. Properties and characterization of treated films. In: *Surface and Coatings Technology* 207 (2012), S. 594–601

[63] Kittel, C. ; McEuen, P.: *Introduction to solid state physics*. John Wiley & Sons, 2018

[64] Kloos, G.: On photoelasticity and the quadratic electrostrictive effect. In: *Journal of Physics D: Applied Physics* 30 (1997), Nr. 10, S. 1536

[65] Kuhl, W. ; Schodder, G.R. ; Schröder, F.-K.: Condenser transmitters and microphones with solid dielectric for airborne ultrasonics. In: *Acta Acustica united with Acustica* 4 (1954), Nr. 5, S. 519–532

[66] Körner, P. M. ; Stiegler, R. ; Meyer, J. ; Wohlfahrt, T. ; Waniek, C. ; Myrzik, J. M. A.: Acoustic noise of massmarket equipment caused by supraharmonics in the frequency range 2 to 20 kHz. In: *2018 18th International Conference on Harmonics and Quality of Power (ICHQP)*, 2018, S. 1–6

[67] Le Besnerais, J.: *Reduction of magnetic noise in PWM-supplied induction machines-low-noise design rules and multi-objective optimization*, Ecole Centrale de Lille, PhD thesis, 2008

[68] Le Besnerais, J.: Vibroacoustic analysis of radial and tangential air-gap magnetic forces in permanent magnet synchronous machines. In: *IEEE Transactions on Magnetics* 51 (2015), Nr. 6, S. 1–9

[69] Le Besnerais, J. ; Lanfranchi, V. ; Hecquet, M. ; Brochet, P.: Characterization and reduction of audible magnetic noise due to PWM supply in induction machines. In: *IEEE Transactions on Industrial Electronics* 57 (2009), Nr. 4, S. 1288–1295

[70] Lee, H. Y. ; Peng, Y. ; Shkel, Y. M.: Strain-dielectric response of dielectrics as foundation for electrostriction stresses. In: *Journal of Applied Physics* 98 (2005), Nr. 7

[71] Lee, H. Y. ; Shkel, Y. M.: The dielectrostriction effect for NDE of polymeric materials. In: *Smart Structures and Materials 2004: Sensors and Smart Structures Technologies for Civil, Mechanical, and Aerospace Systems* Bd. 5391 SPIE, 2004, S. 211–218

[72] Lennström, D. ; Nykänen, A.: Interior sound of today's electric cars: tonal content, levels and frequency distribution / SAE Technical Paper. 2015. – Forschungsbericht

[73] Lenz, T. ; Hummel, R. ; Katsouras, I. ; Groen, W. A. ; Nijemeisland, M. ; Ruemmler, R. ; Schäfer, M. K. ; De Leeuw, D. M.: Ferroelectricity and piezoelectricity in soft biological tissue: Porcine aortic walls revisited. In: *Applied Physics Letters* 111 (2017), Nr. 13

[74] Li, H. ; Chang, B. S. ; Kim, H. ; Xie, Z. ; Lainé, A. ; Ma, L. ; Xu, T. ; Yang, C. ; Kwon, J. ; Shelton, W. S ; and others: High-performing polysulfate dielectrics for electrostatic energy storage under harsh conditions. In: *Joule* 7 (2023), Nr. 1, S. 95–111

[75] Li, H. ; Li, Z. ; Xu, Z. ; Lin, F. ; Wang, B. ; Li, H. ; Zhang, Q. ; Wang, W. ; Huang, X.: Electric field and temperature dependence of electrical conductivity in biaxially oriented polypropylene films. In: *IEEE Transactions on Plasma Science* 42 (2014), Nr. 11, S. 3585–3591

[76] Li, J. ; Ji, S. ; Zhu, L. ; Wu, P. ; Cao, T.: Vibration characteristics of filter capacitors used in HVDC converter stations. In: *IEEE Transactions on Power Delivery* 31 (2015), Nr. 5, S. 2045–2053

[77] Liu, G. ; Hong, J. ; Parker, R. G.: Influence of simultaneous time-varying bearing and tooth mesh stiffness fluctuations on spur gear pair vibration. In: *Nonlinear Dynamics* 97 (2019), Nr. 2, S. 1403–1424

[78] Mandrioli, R. ; Viatkin, A. ; Hammami, M. ; Ricco, M. ; Grandi, G.: Variable switching frequency pwm for three-phase four-wire split-capacitor inverter performance enhancement. In: *IEEE Transactions on Power Electronics* 36 (2021), Nr. 12, S. 13674–13685

[79] Mason, A. ; Mukhopadhyay, S. C. ; Jayasundera, K. P.: *Sensing technology: Current status and future trends III*. Bd. 11. Springer, 2014

[80] Mills, E. J.: I. On electrostriction. In: *Proceedings of the Royal Society of London* 26 (1878), Nr. 179-184, S. 504–512

[81] Mitcheson, P. D. ; Sterken, T. ; He, C. ; Kiziroglou, M ; Yeatman, E.M. ; Puers, R.: Electrostatic microgenerators. In: *Measurement and Control* 41 (2008), Nr. 4, S. 114–119

[82] Montanari, D. ; Saarinen, K. ; Scagliarini, F. ; Zeidler, D. ; Niskala, M. ; Nender, C.: Film capacitors for automotive and industrial applications. In: *Proceedings of CARTS USA 2009* (2009)

[83] Nalwa, H. S.: *Ferroelectric polymers: chemistry: physics, and applications*. CRC Press, 1995

[84] Nanosurf: *How AFM works*. `https://www.nanosurf.com/en/support/afm-operating-principle`. – Latest access on: 15.07.2022

[85] Panasonic Cooperation: *Film Capacitors for automotive Applications*, 2023. `https://industrial.panasonic.com/ww/products-cap/film-capacitors/automotive-film-cap/`. – Latest access on: 22.05.2023

[86] Pastor, M. ; Binda, M. ; Harčarik, T.: Modal assurance criterion. In: *Procedia Engineering* 48 (2012), S. 543–548

[87] Poorfakhraei, A. ; Narimani, M. ; Emadi, A.: A review of multilevel inverter topologies in electric vehicles: Current status and future trends. In: *IEEE Open Journal of Power Electronics* 2 (2021), S. 155–170

[88] Prateek ; Thakur, V. K. ; Gupta, R. K.: Recent progress on ferroelectric polymer-based nanocomposites for high energy density capacitors: synthesis, dielectric properties, and future aspects. In: *Chemical reviews* 116 (2016), Nr. 7, S. 4260–4317

[89] Rao, H. ; Zhou, B. ; Zhang, F. ; Xu, Y. ; Hong, C. ; Yang, J.: A Summary of the Latest Research Progress of Pulse Electroacoustic Method. In: *2021 3rd Asia Energy and Electrical Engineering Symposium (AEEES)* IEEE, 2021, S. 979–983

[90] Ritamäki, M. ; Rytöluoto, I. ; Lahti, K.: DC Voltage Endurance of Capacitor BOPP Films at High Temperature. In: *2018 Ieee 2nd International Conference on Dielectrics (Icd)* IEEE, 2018, S. 1–4

[91] Ritamäki, M. ; Rytöluoto, I. ; Lahti, K.: Performance metrics for a modern BOPP capacitor film. In: *IEEE Transactions on Dielectrics and Electrical Insulation* 26 (2019), Nr. 4, S. 1229–1237

[92] Rogti, F. ; Ferhat, M.: Maxwell–Wagner polarization and interfacial charge at the multilayers of thermoplastic polymers. In: *Journal of Electrostatics* 72 (2014), Nr. 1, S. 91–97

[93] Rytöluoto, I. ; Gitsas, A. ; Pasanen, S. ; Lahti, K.: Effect of film structure and morphology on the dielectric breakdown characteristics of cast and biaxially oriented polypropylene films. In: *European Polymer Journal* 95 (2017), S. 606–624

[94] Rytöluoto, I. ; Ritamäki, M. ; Lahti, K.: Short-term dielectric performance assessment of BOPP capacitor films: A baseline study. In: *2018 12th International Conference on the Properties and Applications of Dielectric Materials (ICPADM)* IEEE, 2018, S. 289–292

[95] Sagadevan, S. ; Sundaram, A S.: A brief review of the relevant dielectric theories of solids. In: *Latin-American Journal of Physics Education* 8 (2014), Nr. 3

[96] Sathyan, S. ; Aydin, U. ; Belahcen, A.: Acoustic noise computation of electrical motors using the boundary element method. In: *Energies* 13 (2020), Nr. 1, S. 245

[97] Schweidler, E. R.: Studien über die Anomalien im Verhalten von Dielektrika. In: *Ann. Phys.* 329 (1907), S. 711–770

[98] Sessler, G. M. ; Turnhout, J. van ; Gross, B. ; Broadhurst, M. G. ; Davis, G. T. ; Mascarenhas, S. ; West, J. E. ; Gerhard-Multhaupt, R.: *Electrets*. Springer-Verlag Berlin Heidelberg GmbH, 1987

[99] Sessler, G. M. ; West, J.E.: Self-Biased Condenser Microphones with High Capacitance. In: *The Journal of the Acoustical Society of America* 34 (1962), Nr. 12, S. 1981–1982

[100] Sessler, G.M. ; West, J.E.: Electret transducers: a review. In: *The Journal of the Acoustical Society of America* 53 (1973), Nr. 6, S. 1589–1600

[101] Shchelko, N.S. ; Sokolova, I.M. ; Zakrzhevskiy, V.I.: CV-testing of electret transducers. In: *Proceedings of 8th International Symposium on Electrets (ISE 8)* IEEE, 1994, S. 1028–1033

[102] Shengchang, J. ; Peng, W. ; Qiaogen, Z. ; Yanming, L.: Study on the noise-level calculation method for capacitor stacks in HVDC converter station. In: *IEEE Transactions on Power Delivery* 25 (2010), Nr. 3, S. 1866–1873

[103] Shkel, Y. M. ; Klingenberg, D. J.: Electrostriction of polarizable materials: Comparison of models with experimental data. In: *Journal of Applied Physics* 83 (1998), Nr. 12, S. 7934–7843

[104] Siegmann, S. ; Abert, C.: 100 years of thermal spray: About the inventor Max Ulrich Schoop. In: *Surface and Coatings Technology* 220 (2013), S. 3–13

[105] Specovius, J.: *Grundkurs Leistungselektronik: Bauelemente, Schaltungen und Systeme*. Springer, 2008

[106] Spitzenberger und Spies: *Quadranten Spannungsverstärker Datenblatt LVA5000*, 2023. `https://www.spitzenberger.de/NEU--AC-DC-2--4--Quadranten-Verstaerker-LVA-dt-source.aspx`. – Latest access on: 22.05.2023

[107] Struller, C.: *Next generation vacuum deposited AlOx clear barrier coatings for flexible food packaging materials*, The Manchester Metropolitan University, PhD thesis, 2013

[108] Struller, C. ; Kelly, P. ; Copeland, N. J.: Aluminum oxide barrier coatings on polymer films for packaging applications. In: *Surface and Coatings Technology* 241 (2014), S. 130–137

[109] Struller, C. ; Kelly, P. ; Copeland, N. J. ; Tobin, V. ; Assender, H. ; Holliday, C. W. ; Read, S. J.: Aluminum oxide barrier films on polymeric web and their conversion for food packaging applications. In: *Thin solid films* 553 (2013), S. 153–156

[110] Struller, C. ; Kelly, P. J. ; Copeland, N. J. ; Liauw, C. M.: Aluminum oxide barrier layers on polymer web. In: *Web coating and Handling Conference 2012* 1 (2012), S. 661–683

[111] Struller, C. ; Kelly, P. J. ; Copeland, N. J. ; Liauw, C. M.: Characterization studies of aluminum ocide barrier coatings on polymeric substrates. In: *Journal of Vacuum Science and Technology A* 30 (2012), S. 041502–1 – 041502–8

[112] Suh, K.-S. ; Tanaka, J. ; Damon, D.: What is TSC? In: *IEEE Electrical Insulation Magazine* 8 (1992), Nr. 6, S. 13–20

[113] Suzuki, Y.: Recent progress in MEMS electret generator for energy harvesting. In: *IEEJ Transactions on Electrical and Electronic Engineering* 6 (2011), Nr. 2, S. 101–111

[114] Thakur, O. P. ; Singh, A.: Electrostriction and electromechanical coupling in elastic dielectrics at nanometric interfaces. In: *Material Science Poland* 27 (2009), Nr. 3, S. 839–850

[115] Thakur, O.P. ; Agrawal, N.: Modelling of sensing performance of electrostrictive capacitive sensors. Springer, 2015, S. 341–358

[116] Tian, F. ; Bu, W. ; Shi, L. ; Yang, C. ; Wang, Y. ; Lei, Q.: Theory of modified thermally stimulated current and direct determination of trap level distribution. In: *Journal of Electrostatics* 69 (2011), Nr. 1, S. 7–10

[117] UBA, Umweltbundesamt: *Position - Kurzfristig kaum Lärmminderung durch Elektroautos*. `https://www.umweltbundesamt.de/sites/default/files/medien/377/dokumente/position_kurzfristig_kaum_laermminderung_im_verkehr.pdf`. Version: 2013. – Latest access on: 04.07.2020

[118] Van der Giet, M.: *Analysis of electromagnetic acoustic noise excitations: A contribution to low-noise design and to the auralization of electrical machines*, PhD thesis, 2011

[119] Van Turnhout, J.: Thermally stimulated discharge of polymer electrets. In: *Polymer Journal* 2 (1971), Nr. 2, S. 173–191

[120] Van Turnhout, J.: *Thermally stimulated discharge of polymer electrets, a study on non-isothermal dielectric relaxation phenomena*, University of Technology Delft, PhD thesis, 1972

[121] Vu, T. T. N. ; Teyssedre, G. ; Le Roy, S. ; Laurent, C.: Maxwell–Wagner effect in multi-layered dielectrics: interfacial charge measurement and modelling. In: *Technologies* 5 (2017), Nr. 2, S. 27

[122] Wang, K. ; Lu, H. ; Li, X.: High-Frequency Modeling of the High-Voltage Electric Drive System for Conducted EMI Simulation in Electric Vehicles. In: *IEEE Transactions on Transportation Electrification* (2022)

[123] Weber, G.: Thermisch stimulierte Entladung als Methode zur Untersuchung der dynamischen Eigenschaften von Polymeren. In: *Progr. Colloid and Polymer Sci.* 66 (1979), S. 125–133

[124] Weber, G. ; Törmälä, P.: Untersuchungen zur Dipol- und Raumladungspolarisation in Polymethylmethacrylat mit Hilfe der thermisch stimulierten Entladung. In: *Colloid and Polymer Sci.* 256 (1978), S. 1137–1139

[125] Wei, S. ; Han, Q. K. ; Dong, X. J. ; Peng, Z. K. ; Chu, F. L.: Dynamic response of a single-mesh gear system with periodic mesh stiffness and backlash nonlinearity under uncertainty. In: *Nonlinear Dynamics* 89 (2017), Nr. 1, S. 49–60

[126] Xiao, M. ; Du, B. ; Xu, R. ; Ran, Z. ; Liu, H. ; Xing, J. ; Fan, K.: Improvement of Dielectric Properties of Polypropylene Film for HVDC Metallized Film Capacitors. In: *Polymer Insulation Applied for HVDC Transmission*. Springer, 2021, S. 627–651

[127] Xue, Y. ; Zhao, J. ; Zhang, X. ; Sessler, G. M. ; Kupnik, M.: Acoustic energy harvesting with irradiated cross-linked polypropylene piezoelectret films. In: *Physica Scripta* 94 (2019), Nr. 9, S. 095002

[128] Zeiss Deutschland: *FIB-SEM-Technologie*. `https://www.zeiss.de/mikroskopie/produkte/fib-sem-instruments/crossbeam/crossbeam-technology.html#FIB-SEM-Technologie`. Version: 2020. – Latest access on: 09.07.2020

[129] Zhang, X. ; Seggern, H. von ; Sessler, G. M. ; Kupnik, M.: Mechanical energy harvesting with ferroelectrets. In: *IEEE Electrical Insulation Magazine* 36 (2020), Nr. 6, S. 47–58

[130] Zhu, L. ; Ji, S. ; Shen, Q. ; Liu, Y. ; Li, J. ; Liu, H.: A noise prediction method based on electro- mechanical frequency response function for capacitors. In: *PLOS ONE* 8 (2013), Nr. 12, S. 1–9

[131] ZVEI: *Basic Qualification of DC-Link Capacitors for Automotive Use*. `file://europe.bmw.corp/winfs/EA-proj/Motor/ProAn_01_EAM/Modul_MR/GEN6/BE_GEN6_TEE/06_Produkt/90_ZKK/33_Test_und_Absicherung/ZVEI_Basic_Qualification_of_DC-Link_Capacitors_for_Automotive_Use_V2.pdf`. Version: March 2022. – Latest access on: 21.04.2024